



## TELESCOPES AND INSTRUMENTATION

## FEROS, the Fiber-fed Extended Range Optical Spectrograph for the ESO 1.52-m Telescope

A. KAUFER, B. WOLF; *Landessternwarte Heidelberg-Königstuhl, Germany*  
 J. ANDERSEN, *Astronomical Observatory Copenhagen, Denmark*  
 L. PASQUINI, *ESO*

### Overview

FEROS is a fiber-fed bench-mounted prism-crossdispersed echelle spectrograph for the ESO 1.52-m telescope at La Silla. It works in quasi Littrow mode and in white pupil configuration. For the object and the nearby sky, the complete optical spectrum from 370–860 nm is recorded in one exposure with a resolving power of  $R = 48,000$  by the use of a two-beam, two-slice image slicer.

A first concept of FEROS, which is supposed to replace ECHELEC at the 1.52-m telescope, was presented by Pasquini et al., 1992, "FEROS for the ESO 1.52-m Telescope", 32nd Scientific Technical Committee Meeting, Garching. Designed as a fiber-linked spectrograph connected to the permanently mounted Boller & Chivens spectrograph it has the advantage of being always available. The fibre entrance of FEROS is mounted on the slit unit of the Boller & Chivens spectrograph, and it will be possible to change from one spectrograph to the other by a simple translation of the slit unit. Because FEROS provides high-

dispersion spectroscopy with a wide, simultaneous wavelength coverage, this instrument mounted on an intermediate-size telescope fills a gap in the present and future ESO instrumentation park. It will allow to realise many important scientific programmes (a few of which are described below) of objects down to about 16th magnitude with high efficiency, little constraints on operations and will relieve the pressure on larger telescopes.

FEROS is built for ESO by a consortium of four astronomical institutes under the leadership of the Landessternwarte Heidelberg (LSW). The Principal Investigator (PI) of the FEROS project is Prof. Dr. Bernhard Wolf at the LSW. Further members of the consortium are the Astronomical Observatory Copenhagen (AOC), the Institut d'Astrophysique de Paris (IAP), and the Observatoire de Paris/Meudon (OPM). The contract between ESO and the FEROS Consortium was signed in September 1996. It is planned that the instrument will be available to the community in early 1999.

### Scientific Objectives

The need for instruments for high-resolution spectroscopy has increased considerably in the last years. With the advent of fiber-linked echelle spectrographs, the former domain of the largest telescopes became accessible for small- to medium-size telescopes with their advantage of higher availability for long-term programmes. Furthermore, the high long-term spectral stability of bench-mounted and fiber-fed spectrographs turns out to be crucial for high-precision spectroscopic work. Therefore, it is expected that FEROS will be an important work-horse instrument for the ESO community, e.g., for the search for extrasolar planets with high-precision radial-velocity measurements on long time bases, for investigations in the growing field of asteroseismology, and for spectroscopic investigations of time-dependent phenomena in stellar atmospheres and envelopes in general.

FEROS at the ESO 1.52-m telescope will meet the requirements posed by

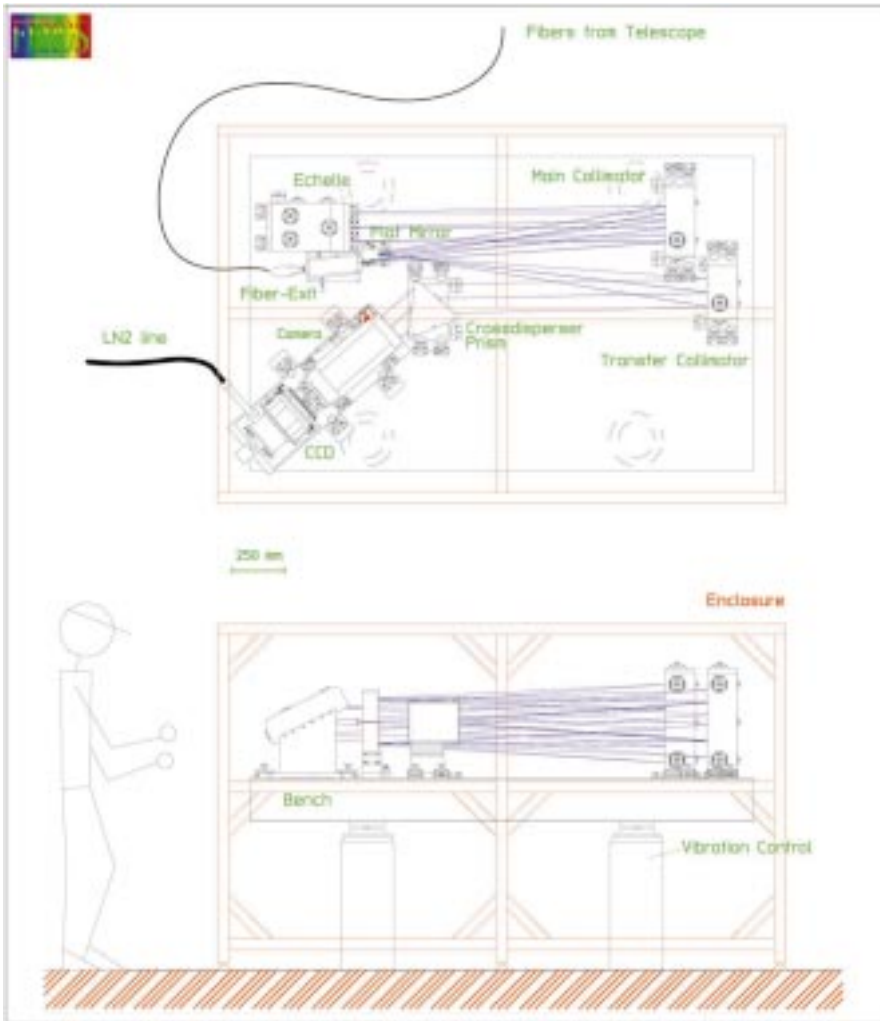


Figure 1: Top and side view of the opto-mechanical layout of FEROS.

these scientific objectives. Due to its high efficiency, many of the observing programmes which to date can only be conducted with CASPEC at the 3.6-m telescope or EMMI at the NTT are within reach of FEROS with a comparable spectral resolution and even superior spectral coverage. The same holds for the CES at the CAT if the highest-resolution mode is not imperative for an observing programme. It is worth to note that FEROS will not touch the domain of programmes which can only be carried out effectively with UVES at the VLT, i.e., low to medium  $S/N$  observations of the faintest objects and high  $S/N$  observations with resolutions of the order  $10^5$  of brighter objects [Dekker & D'Odorico, 1992, *The Messenger* 70].

## Instrument Description

### Opto-mechanical layout

The bench-mounted part of the opto-mechanical layout of FEROS is shown in Figure 1. The Boller & Chivens spectrograph in the Cassegrain focus of the ESO 1.52-m telescope will be modified to carry the additional fibre-entrance unit and the extended calibration unit for both spectrographs.

The light of the object and the nearby sky is coupled via micro-lenses into two 100  $\mu\text{m}$  fibres in the Cassegrain focus of the telescope. The micro-lenses convert the F/15 telescope beam into a F/4.6 beam which is optimal for the fibres. In the coudé room, where the bench-mounted spectrograph will be located in a temperature- and humidity-controlled

room, the fibre exit is converted to the F/11 focal ratio accepted by the spectrograph via a lens system. A two-beam, two-slice image slicer in the F/11 focal plane halves the width of the images of the two fibres in the direction of dispersion (cf. Fig. 3). The fibres are re-imaged on the R2 echelle grating through the main off-axis collimator. Then, the light goes back to the main collimator and is reflected by the flat folding mirror to the transfer off-axis collimator. The entrance surface of the large LF5 prism cross-disperser is located near the white pupil image and the light is finally imaged by the dioptric camera onto the detector. The detector foreseen is a monolithic thinned  $2048 \times 4096$   $15 \mu\text{m}$  pixel CCD.

The mechanical design of FEROS follows in many parts the design of the UVES instrument and consequently uses standard techniques for bench-mounted instrumentation. The echelle grating and the off-axis collimators are mounted in kinematic mounts; if feasible, standard industrial mechanical elements are used.

To ensure a maximum long-term stability of the spectrograph, *no* movable or remotely-controlled parts besides the CCD shutter are foreseen on the bench-mounted part of the instrument. Further, the CCD detector will be equipped with a continuous-flow cryostat supplied with liquid nitrogen from a nearby vessel with a capacity for about two weeks. The cooling by a continuous flow of liquid nitrogen is important to keep the weight of the CCD dewar constant over longer periods. The evaporation of the  $\text{LN}_2$  from a standard dewar during the night would cause considerable shifts of the spectrum in main dispersion direction on the detector. In addition, the spectrograph is built on a vibration-controlled optical bench and will be housed in a separate light-tight room, which is temperature and humidity controlled.

The main parameters and the ex-

Table 1: Main parameters of FEROS.

Wavelength range in one exposure (object+sky)	3700–8600 Å (40 orders, 2 fibres)
Resolving Power (with 2-slice image slicer)	$\lambda/\Delta\lambda = 48,000$
Entrance Aperture	2.7 arcsec
Fiber input/output Focal Ratio	F/4.6
Spectrograph Beam Size	136 mm diameter
Off-axis Collimators	F/11, cut from one parent paraboloid
Echelle	R2, 79 lines/mm, 154 mm by 306 mm
Crossdisperser Prism	LF5 glass, 55° apex angle
Dioptric Camera	
Wavelength Range	350–900 nm
Focal Length; F ratio	410 mm; F/3.0
Field Diameter	69 mm
Image quality ( $E_{80}$ )	< 25 $\mu\text{m}$
Efficiency	> 85%
CCD	2048 $\times$ 4096, 15 $\mu\text{m}$ , thinned
Expected Detection Efficiency (without telescope)	6% (3700 Å), 21% (5000 Å), 9% (9000 Å)
Expected Limiting Magnitudes at the ESO 1.52-m	16 mag in V (S/N = 10, 2 h) 12 mag in V (S/N = 100, 2 h)
Expected Radial-Velocity Accuracy	< 25 m/s, < 5 m/s with iodine cell (contract: < 50 m/s)

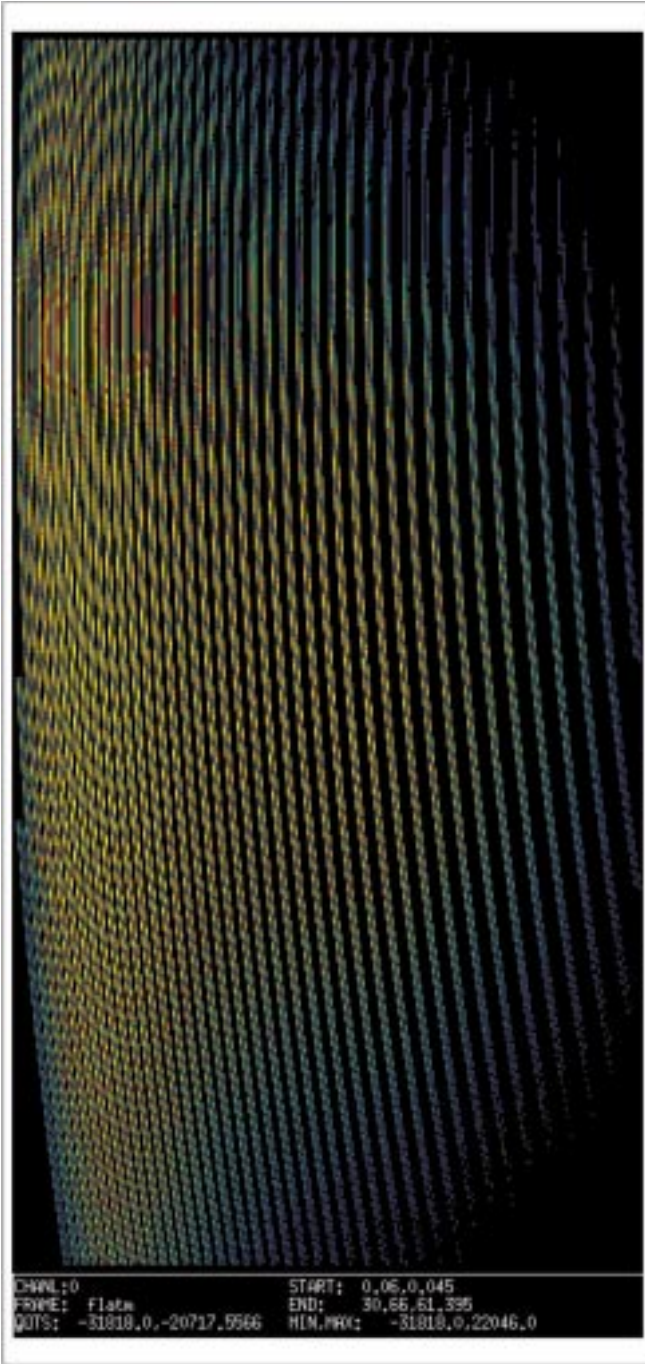


Figure 2: Spectral format of FEROS showing a simulated flatfield exposure. Red is to the left with the extreme order 32 with  $\lambda_c = 9850 \text{ \AA}$ ; blue is to the right with the extreme order 63 with  $\lambda_c = 3600 \text{ \AA}$ . Each spectral order is double due to the illuminated object and sky fibre. The whole echelle spectrum is rotated counter-clockwise by  $2.4^\circ$  to align the slit image with the CCD rows.

beam is evaluated at the moment [cf. Butler et al., 1996, *PASP* 108, 500].

For flatfield and wavelength calibrations, the B&C calibration unit will be equipped with a blue-enhanced flatfield source and a Thorium-Argon hollow-cathode lamp, respectively.

All observing modes will be supported by the DAISY instrument control software foreseen at the ESO 1.52-m telescope for the operation of the B&C and the FEROS instruments. This will allow a change between the two instruments within a few minutes – an interesting option for spectroscopic programmes which require a pre-examination of the targets with low resolution or spectrophotometric observing programmes.

Further, full on-line data reduction will be available at the telescope to enable the observer to fully exploit the capabilities of the instrument already during the observations.

### Spectral Format

A simulation of the two-dimensional echelle spectrum on the  $2k \times 4k$   $15 \mu\text{m}$  detector is shown in Figure 2. This simulation includes the wavelength-dependent intensity distribution of the blue-enhanced flatfield source, the wavelength dependent transmission of FEROS itself, the two-beam two-slice image slicer, models for the blaze function, for the straylight distribution, and for the photon and detector noise. This simulation runs in the MIDAS environment and is primarily used for the development of the on-line data-reduction and instrument-simulation software.

A special complication of the spectral format is introduced by the permanently mounted Bowen-Walraven image slicer which is needed to achieve the spectral resolution of  $R = 48,000$ . Figure 3 shows the output of a scaled prototype of this device built from Acrylic in the mechanical workshop at the LSW. The circular outputs of the two object and sky fibres (top) are simultaneously sliced into two 'half moons' (bottom) which effectively halves the equivalent slit width in the main dispersion direction. The equivalent slit height was chosen to be 4.5 times the slit width which leaves a quite small gap between the two half moons. The individual slit images will be sampled on 2 by 10 pixels on the CCD detector. Therefore, a double-peaked cross-dispersion slit profile has to be handled by the data-reduction software, which requires special care for the order definition and the optimum extraction.

pected performance for FEROS are summarised in Table 1.

### Observing Modes

For the observations with FEROS, only three observing modes will be provided:

1. Calibration (Flatfield and Thorium-Argon)
2. Object + Sky
3. Object + Calibration

For the latter mode, the spectrum of an adequately attenuated Thorium-Argon lamp will be recorded through the sky fiber during the object exposure. The Object + Calibration mode allows to record the residual motions of the spectrograph during the object exposure and to consid-

erably improve the radial-velocity accuracy. This technique in combination with software cross-correlation has successfully been used in the ELODIE instrument at the Observatoire de Haute-Provence and achieves a long-term accuracy of  $< 15 \text{ m/s}$  for a sharp-lined G dwarf [Baranne et al., 1996, *A&AS* 119, 373]. For even higher accuracy of the order of  $< 5 \text{ m/s}$ , the use of an iodine absorption cell placed in the telescope

Table 2: Time schedule for FEROS.

Contract Signature	September 1996
Final Design Review	June 1997
Preliminary Acceptance (@LSW, HD)	June 1998
Provisional Acceptance (@ESO, La Silla)	December 1998
Availability to the Community	early 1999

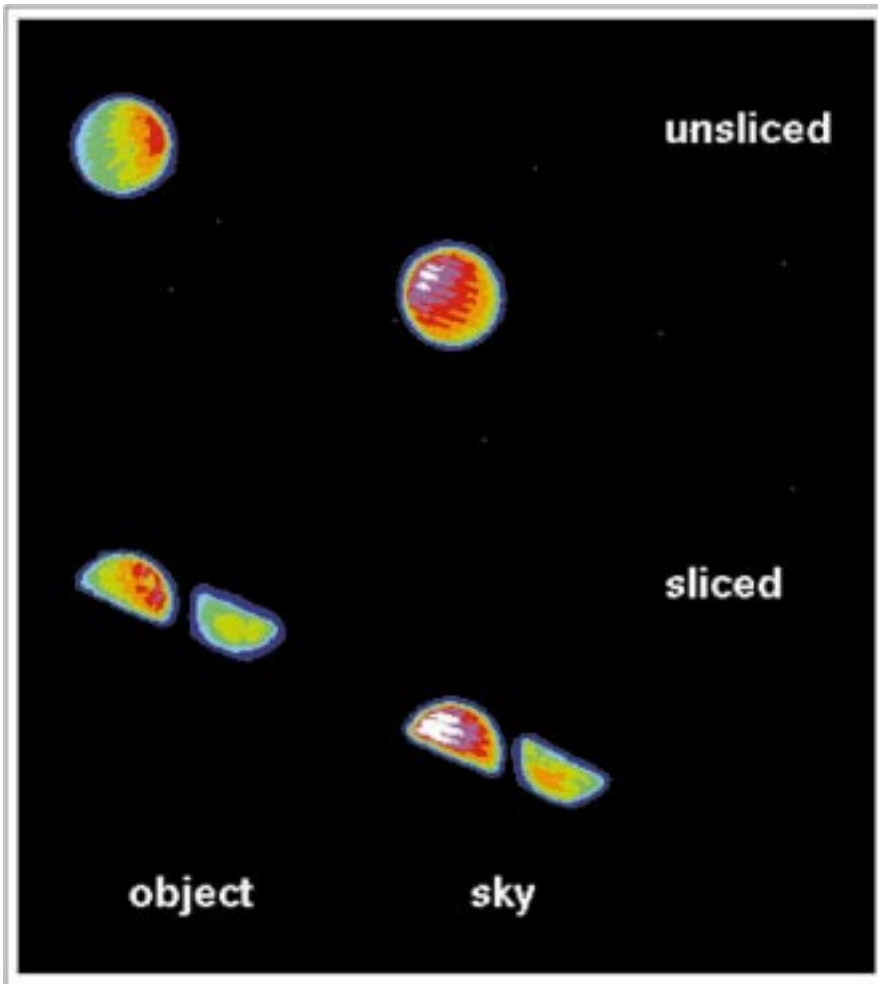


Figure 3: CCD images of the unsliced and sliced outputs of the scaled image-slicer prototype. The inhomogeneous intensity distributions within the images is due to the low polishing quality and inhomogeneity of the Acrylic's surfaces.

### CCD Detector

The thinned  $2k \times 4k$  CCD and the standard ESO-VLT continuous-flow cryostat will be provided by ESO (cf. Lizon, 1997, *The Messenger* 88, p. 6, Fig. 1).

The CCD controller electronics will be built by the AOC; also the integration and testing of the complete CCD system will be carried out at the AOC. For the beginning, an engineering grade  $13.5 \mu\text{m}$  EEV CCD was already delivered by ESO at the end of March 1997. The first devices of this type have been tested at the Royal Greenwich Observatory. They show a good performance with an on-chip noise of  $4 e^-$  rms and

a peak quantum efficiency of 85% at 550 nm and 27% (goal 50%) at 350 nm. The delivery of the science grade  $15 \mu\text{m}$  EEV CCD to the FEROS consortium is planned for November 1997.

### On-line Software

The FEROS data reduction software (DRS) is currently developed in the MIDAS environment at the LSW. The DRS will provide full on-line data reduction of the standard observing modes at the telescope workstation during the observation. In addition, the observer will be supported by a graphical user interface (GUI) for the on-line reduction and

an instrument simulation for the preparation of the observations.

A dedicated DRS is particularly suitable for the FEROS instrument because of its fixed configuration. But it is also crucial because of the complex spectral format on the CCD and the large size of the raw frames (16 Mb for a 16-bit ADC). As was seen in Figure 2, the DRS has to cope with the strong curvature of the orders, the doubling of the orders due to the object and sky/calibration fibres, and the double-peaked slit profile in cross-dispersion direction.

Basically, the DRS will follow the standard echelle reduction scheme with order definition, wavelength calibration, background subtraction, flatfield correction, optimal order extraction to optimise the S/N of the spectra, rebinning to constant wavelength steps in linear and logarithmic scale, and if required, order merging, correction for the instrument response function, and sky subtraction. It is worth to note that because of the very stable spectral format of the bench-mounted and fiber-fed spectrograph, the correction for the blaze function, that is needed to allow precise order merging, can be carried out with the internal flatfields alone. Further, cross-correlation facilities will be supplied for high-precision radial velocity work and time-series analysis facilities for variable-star research which probably will be the main fields of work for FEROS.

### Time Schedule

The time schedule for the FEROS project is given in Table 2. It is planned to make the instrument available to the community in early 1999. The present status of the project is that after the final optical design review was passed in October 1996, the procurement of the optical components was started immediately. The final mechanical design was completed in June 1997 and the manufacturing of the mechanical components started afterwards. The FEROS final design was presented at the design review at the end of June 1997 and was approved by ESO. Up-to-date information on the status of the project is available in the WWW on the FEROS homepage (URL <http://www.lsw.uni-heidelberg.de/~akaufer/Feros.html>).

### Project Teams

The project teams of the consortium and ESO consist of the people listed in Table 3. The project is further supported by the technical advice of G. Avila, B. Delabre, H. Dekker, W. Eckert, A. Gilliotte, J.-L. Lizon, and R. Olivares at ESO.

Table 3: FEROS project teams.

LSW	B. Wolf (PI), I. Appenzeller (Advisor) A. Kaufer (Instrument Responsible) W. Seifert (Optic Design), H. Mandel (Adjustment) O. Stahl, A. Malina (Data-Reduction Software) C. Hartlieb, L. Schäffner (Mechanics)
AOC IAP OPM	J. Andersen, P. Nørregaard, J. Klougart (CCD controller) M. Dennefeld R. Cayrel
ESO	L. Pasquini (Instrument Scientist)

A. Kaufer  
E-mail: [A.Kaufer@lsw.uni-heidelberg.de](mailto:A.Kaufer@lsw.uni-heidelberg.de)

# Predicting Observing Conditions at ESO Observatories – Reality and Perspectives\*

M. SARAZIN, ESO

## 1. Introduction

It is now understood that most future ground-based observatories will make use of flexible scheduling tools to select the observing mode best adapted to the observing conditions.

ESO has been conducting a wide survey of existing and potential forecasting techniques and, on the basis of a strategy described in Figure 1, several feasibility studies were initiated from 1992 onwards, both internally and externally. Most of them are completed or close to completion. It is thus time to prepare the specifications of the operational tools and services to be developed for the VLT.

For this purpose, a workshop on *Forecasting Astronomical Observing Conditions* took place on 29–30 May, 1997 at ESO Garching. A summary of the main results is presented in what follows, trying to establish the current state of the art applicable to Chilean observatories as a whole.

In his introductory talk, the ESO Director General stressed that ESO is aiming at the highest observing efficiency at the VLT to make possible the scientific discoveries the astronomical community legitimately expects from such a tool. The DG also indicated that the cost of a night of operation of the observatory ( $\approx 100,000$  DM) gives the scale for deciding the extent to which ESO should push research in modelling and prediction. He noted in particular that he would probably exclude launching a dedicated satellite (as proposed by one of the speakers) but that he would certainly support further measurement campaigns or local instrumentation development if deemed necessary.

In what follows, the meteorologists attempt to answer questions preoccupying most individuals involved in the planning of observatory operation. A common tool for all studies is the invaluable forecast service provided by ECMWF (European Centre for Medium-Range Weather Forecasts) or its US equivalent NCEP (National Centre for Environmental Prediction). We are grateful to ECMWF to

have accepted ESO's invitation to be represented at this workshop to introduce the participants to the complex world of forecasting.

## 2. Forecasting Cloudiness and Water Vapour

*Will next night be photometric? When to schedule infrared observing? How stable is the current situation?*

### 2.1 Meteorology and satellite images

The study of ECMWF forecast skill over ESO observatories ([CRS4 97]) has shown that the global forecasts of cloudiness and water vapour did not reach the type of accuracy needed for astronomy. A more successful method proposed by [Erasmus 97] combines synoptic scale circulation modelling with ECMWF standard forecasts and analyses (geopotential height, wind components, temperature and vertical velocity) as well as local surface relative humidity to extract from a  $6.7 \mu\text{m}$  satellite image, the pixels which will pass over the observatory during the period predicted, and the corresponding water vapour content. The large-scale circulation patterns affecting the Chilean coast are presented in Figure 2. The particular situation of the Atacama desert with respect to cloudiness and water vapour

is clearly illustrated. Here follows a summary of the presentation by A. Erasmus:

*In summer the pressure systems move southwards and the Subtropical high pressure (H) strengthens and expands its area of influence. Subsidence in the high creates a strong temperature inversion at about 1000 m above the surface which traps low-level stratocumulus clouds below it (notice the area of medium grey speckled cloud in and around the high). The subtropical high is a semi-permanent circulation feature that only experiences minor position changes as the high develops east or west of its mean position. The high produces clear dry conditions over northern Chile. Occasional incursions of moisture and cloud may occur over northern Chile from the north in summer if the high weakens and the anticyclonic flow over the Amazon basin intensifies.*

*In winter the pressure systems move northwards and the subtropics comes under the influence of migratory wave-like systems that propagate from west to east in the prevailing flow. The high pressure area of the wave (the ridge) is warm and dry while the low pressure area (the trough) is cool and moist. Middle and upper tropospheric clouds can typically be found along the leading edge of the ridge and trough in association with surface warm and cold fronts. Trough and ridge development, which is*

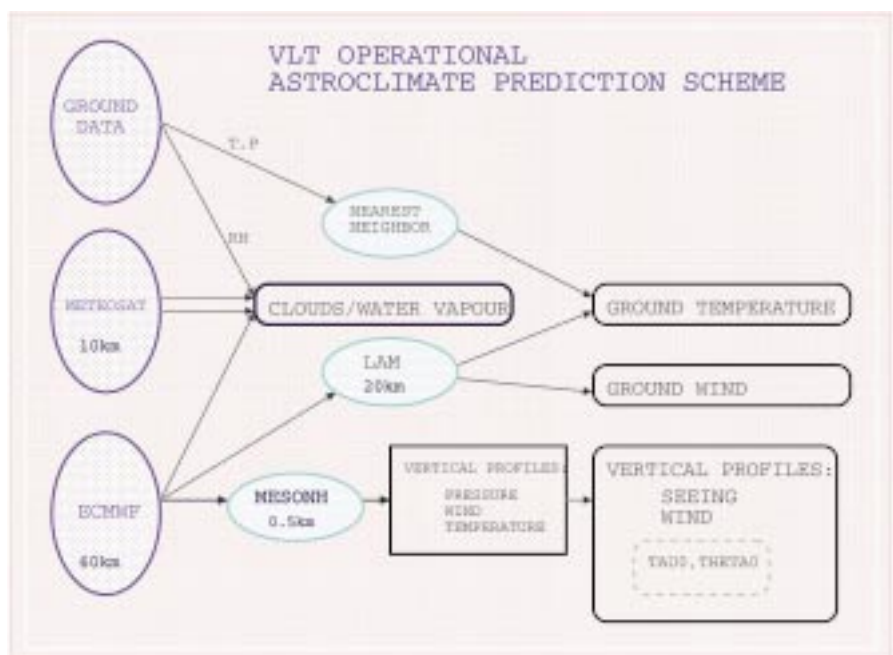


Figure 1: Initial organigram of the prediction strategy for the VLT Observatory.

\*This article summarises the talks and discussions during the meeting. Speakers were A. Erasmus (University of Northern Colorado), A. Speranza, R. Deidda and M. Maroccu (CRS4, Cagliari), J. Vernin and E. Masciadri (University of Nice), A. Lanzinger (ECMWF Reading) and the author of the present article. The agenda of the Workshop can be found in *The Messenger* No. 88, June 1997, p. 35.

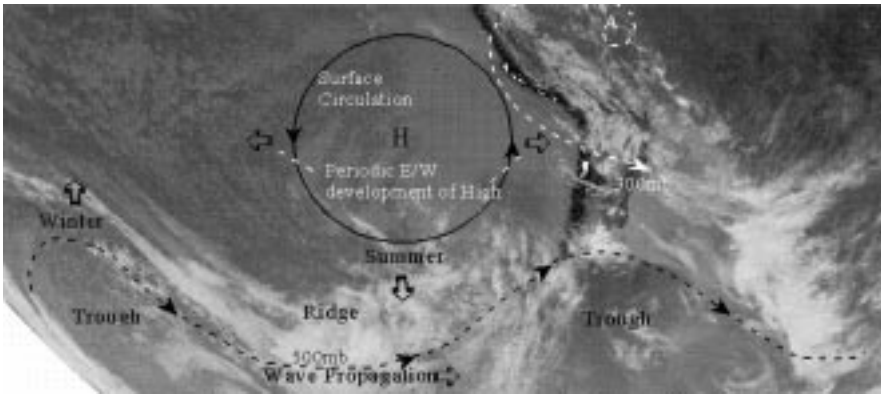


Figure 2: Schematic diagram showing the main synoptic scale circulation systems that control water vapour and cirrus cloud cover advection patterns over the South-eastern Pacific Ocean. The satellite image is taken at 11  $\mu\text{m}$  in the atmospheric IR window. Warmer surfaces appear dark and cold surfaces light. Clouds behave essentially as blackbodies at this wavelength, hence low clouds (being warmer) are medium grey and higher clouds (being cold) appear light grey or even white for the highest (about 15 km), coldest cirrus clouds.

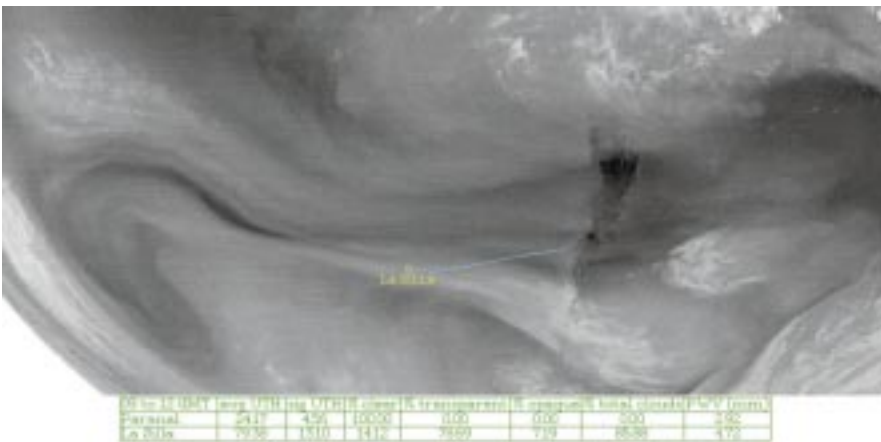


Figure 3: Sample 6.7  $\mu\text{m}$  Satellite Image and Output of Cloudiness and Water Vapour Forecast over La Silla Observatory: the model identifies at 15 h UT, on November 29, 1993, the image pixel which will most probably pass over the observatory 20 hours later.

usually slight over the south-eastern Pacific, may add a meridional component to the cloud cover and water vapour advection patterns.

## 2.2 Forecast skill

It was demonstrated that operational forecast of cloudiness and water vapour is feasible for observatories in Chile. The product illustrated in Figure 3 consists of a daily estimate of the percentage of the sky to be clear, covered with transparent cirrus, or by opaque clouds, and the total amount of precipitable water vapour, for the next 24 hours by periods of 3 hours. In addition, an up to 7-day daily outlook of status and tendency will be issued on qualitative grounds such as dry/moist and persisting/drying/moistening.

The image area trajectory is forecast with an rms error below 8% in image transparency units. The water vapour forecasts agree with infrared radiometric measurements taken from the ground at Paranal (NOAO Water Vapour Monitor) within an rms of 1.0 mm  $\text{H}_2\text{O}$  (comparable to the dispersion between the WVM ground measurements and the Antofagasta radiosonde). Cloudy sky is successfully forecast 95% of the time at

Paranal and 84% at La Silla, with respectively 2% and 7% false alarm rate.

## 3. Forecasting Temperature and Wind at Ground Level

### 3.1 24-hour ahead temperature forecasts

*At which temperature should the air conditioning of the enclosure be preset during the day so that the telescope and primary mirror are in thermal equilibrium with the outside air at the beginning of the next night?*

A chronologically first, non meteorological approach was to train some statistical engine on the large database

available for ESO sites. An internal study was conducted ([Aussem 94]) and led to the results presented in Table 1 where the nearest neighbour technique clearly outperforms the neural nets, in particular with regard to the fine tuning of the forecast (prediction error smaller than 0.5 Celsius in 62% of the cases). However, as could be expected, none of these techniques can catch weather trends leading to abrupt temperature shifts of 2 to 6 degrees in 24 hour, representing about 15% of the time at Paranal during the season studied (summer).

Could large  $\Delta T$  be better predicted using meteorological models? Obviously, a global model such as ECMWF has a mesh much too large (ca. 60 km) for the steep terrain surrounding astronomical sites. Such a model has to be complemented either by a statistical post-processing such as Kalman filtering, or by a local area model (LAM) implementation. The study of 4 sample years conducted by [CRS4 97] concluded that the poorness of local measurements over the Pacific was limiting the accuracy of ECMWF forecasts on the Chilean coast. A LAM initialised by erroneous forecasts without injection of additional observational data could obviously not improve the detection of unpredicted weather changes coming from outside its orographic limits.

Table 2 shows however that a simple Kalman postprocessing of ECMWF 24-hour forecasts successfully cancels the forecast systematic errors (the correlation coefficient of postprocessed forecasts is as good as for the analysis). As expected, postprocessing alone is not able to remove synoptic errors so that large differences between actual and forecasted temperatures still subsist. Table 3 summarises the forecast skill at 12 hour UT at Paranal as a function of 24-hour temperature changes, it shows that 55% – (159+158)/572 – versus 40% – (112+117)/572 – of the cases are brought inside the  $\pm 1$  C range, and that 84% versus 69% are smaller than  $\pm 2$  C. These performances are very similar to the results obtained with the statistical method of Table 1, however it is believed – but not proven – that the cases corrected by either methods have little in common, so that a mixture of both techniques (as proposed on Fig. 1) would consistently improve the forecast skill.

Prediction error (Celsius)	$\leq 2$	$\leq 1$	$\leq 0.5$
Best Nearest Neighbour	84%	73%	62%
Best Neural Network	71%	43%	22%
Carbon Copy $t_n = t_{n-1}$	63%	36%	19%

Table 1: 24-hour ahead statistical forecast of ground temperature at each hour of the day: hit rate of nearest neighbour and neural network methods over 18,000 observations corresponding to summer 1989/1990 at Paranal. Nearest neighbour predictions were carried out on a 5-tuple set of the type  $[t_{n-1}, t_{n-2}, t_{n-3}, p_{n-1}, p_{n-2}]$ .

Site	N	$ \epsilon^{Kal} $	$r^{Kal}$	$ \epsilon^{per} $	$r^{per}$	$r^{for}$	$r^{ana}$
La Silla	1114	1.6	0.86	2.1	0.77	0.82	0.86
Paranal	572	1.1	0.88	1.5	0.80	0.79	0.87

Table 2: Absolute mean errors ( $|\epsilon|$ ) and correlations ( $r$ ) between observed 2-metre temperatures ( $C$ ) and estimations by Kalman filter post-processing ( $^{Kal}$ ) compared to persistence ( $^{per}$ ), ECMWF 24-hour forecast ( $^{for}$ ), and ECMWF analysis ( $^{ana}$ ).  $N$  is number of data used for comparison during the period from 1989 to 1993.

Let us extract from Table 3 the forecast skill in the cases when the telescope temperature would be 2 C or more warmer than the outside air, a situation which is detrimental for observations at all wavelengths (local seeing greater than 1 arcsec in the visible). Such cases are down by a factor of 2 from 15%  $-(4+11+22+46)/572$  – to 7.5%  $-(2+3+12+33)/572$ . Converting the overall temperature unbalance of Table 3 into mirror seeing with a rate of 0.5 arcsec per positive degree and 0.1 arcsec per negative degree, we obtain a yearly average mirror seeing in the first hour of observation of 0.48 arcsec with persistence ( $T_n = T_{n-1}$ ) down to 0.35 arcsec when Kalman filtered ECMWF forecasts are used.

### 3.2 24-hour-ahead forecasts of wind 10 metres above ground

*Is there any chance that observations have to be stopped in the course of the night because the wind is reaching the maximum operating velocity (20 m/s)?*

This topic did not meet a satisfying answer until now. The results of Table 4 by [CRS4 97] show large errors and poor correlation of 10-metre wind forecasts and analyses with data measured at Paranal or La Silla.

As for 2-metre temperature, much of ECMWF forecast error is due to the lack of observational data in the Antofagasta area and could not be corrected by implementing a LAM (20 km mesh) without injection of new observational data. However, unlike 2-metre temperature, not only the forecasts but also the analyses are poorly correlated. Obviously, a global model such as ECMWF and even the LAM have a mesh much too large for the steep terrain surrounding astronomical sites. One has probably to go down to a mesoscale model such as the one described in Section 4.2 (ca. 500 m mesh). A sample output on Figure 4 shows that local overspeed and shears are then clearly visible. Other more straightforward methods such a modified mass-consistency models could be investigated to improve the case of 10-metre wind forecast.

## 4. Forecasting Seeing

### 4.1 Introduction

*Does it make sense to plan using adaptive optics in the next coming hours? What is the improvement in Strehl ratio to be expected?*

To answer this question, two parameters have to be known: the distribution of the turbulence along the path, and its rate of change. The strategy chosen to obtain such forecasts requires three steps:

- (1) Obtain a reliable forecast of the

vertical profile of the temperature of the atmosphere several tens of kilometres upwind (Section 4.3).

(2) Use this profile to initialise a mesoscale model capable to reflect the effect of the terrain on an unperturbed atmosphere, in particular the triggering of gravity waves or the increase of mixing due to orographic wind shear (Section 4.2).

(3) Combine the output of the mesoscale model (vertical profile of turbulence corresponding to the forecasted vertical profile of temperature) with a forecast of the vertical profile of the wind field above the observatory so as to compute the wavefront velocity (Section 4.4).

		Actual 24-hour change (K)													
		-6	-5	-4	-3	-2	-1	1	2	3	4	5	6		
KFPP Error (K)	-6	0	0	0	1	1	0	0	0	0	0	0	0	2	KFPP Scores
	-5	0	0	0	0	0	0	0	0	0	0	0	0	0	
	-4	0	1	1	4	2	1	0	0	0	0	0	1	10	
	-3	0	1	3	8	9	3	3	2	1	1	0	0	31	
	-2	1	2	11	14	17	22	9	3	0	0	0	0	79	
	-1	1	5	3	14	38	38	34	15	9	2	0	0	159	
	1	2	2	2	4	15	34	47	28	16	5	3	0	158	
2	0	0	2	1	5	9	21	15	18	5	5	2	83		
3	0	0	0	0	4	5	2	6	10	1	2	3	33		
4	0	0	0	0	0	0	1	3	4	2	1	1	12		
5	0	0	0	0	0	0	0	1	0	1	1	0	3		
6	0	0	0	0	0	0	0	0	1	0	0	1	2		
		4	11	22	46	91	112	117	73	59	17	12	8		

Global scores of persistence

Table 3: Contingency table between errors of Kalman Filtering Postprocessing Procedure (KFPP) and Air Temperature ( $T_{2m}$ ) daily variation at Paranal during the period 1989–1993 at 12GMT. Sum of the counts along rows (shown in the last column of the table) is the number of times  $T_{2m}$  has been forecasted within an error indicated in the first column of the table itself. Sum of the numbers along a column (shown in the last row), is the number of times  $T_{2m}$  has had a diurnal variation within the value shown in the first row. The generic count within a cell of the table gives number of times  $T_{2m}$  has been forecasted within an error indicated in the corresponding cell of the first columns when the daily variation of  $T_{2m}$  was that indicated in the corresponding cell of the last row.

Site	N	$ \epsilon^{Kal} $	$r^{Kal}$	$ \epsilon^{per} $	$r^{per}$	$r^{for}$	$r^{ana}$
La Silla	1242	2.5	0.64	2.9	0.59	0.57	0.43
Paranal	608	3.0	0.59	3.4	0.56	0.50	0.64

Table 4: Absolute mean errors ( $|\epsilon|$ ) and correlations ( $r$ ) between observed 10-metre wind speed (m/s) and estimations by Kalman Filtering Postprocessing Procedure or KFPP ( $^{Kal}$ ) compared to persistence ( $^{per}$ ), ECMWF 24-hour forecast ( $^{for}$ ), and ECMWF analysis ( $^{ana}$ ).  $N$  is number of data used for comparison during the period from 1989 to 1993.

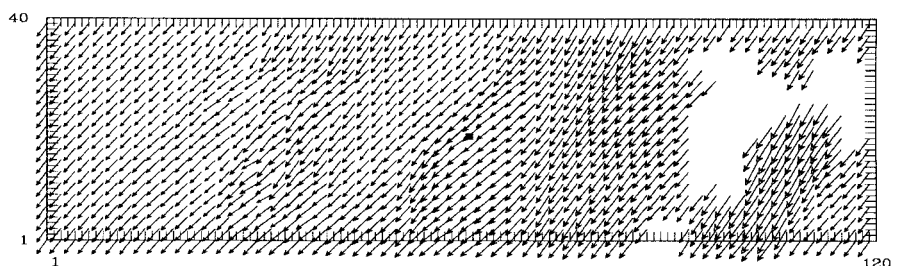


Figure 4: Sample Output of Surface Wind Mesoscale Modelling in the Paranal Area at 2600 m altitude on the terrain model of Figure 5 [Masciadri 97].

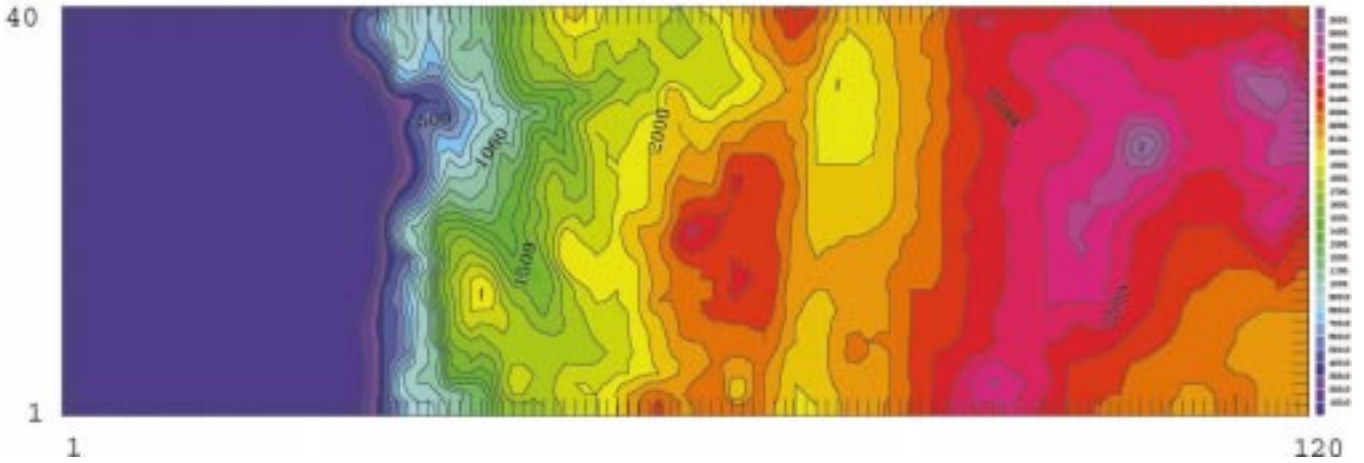


Figure 5: Input terrain model for Mesoscale Modelling in the Paranal Area with a 500 m horizontal resolution over an area of  $60 \times 20$  km centred on the site.

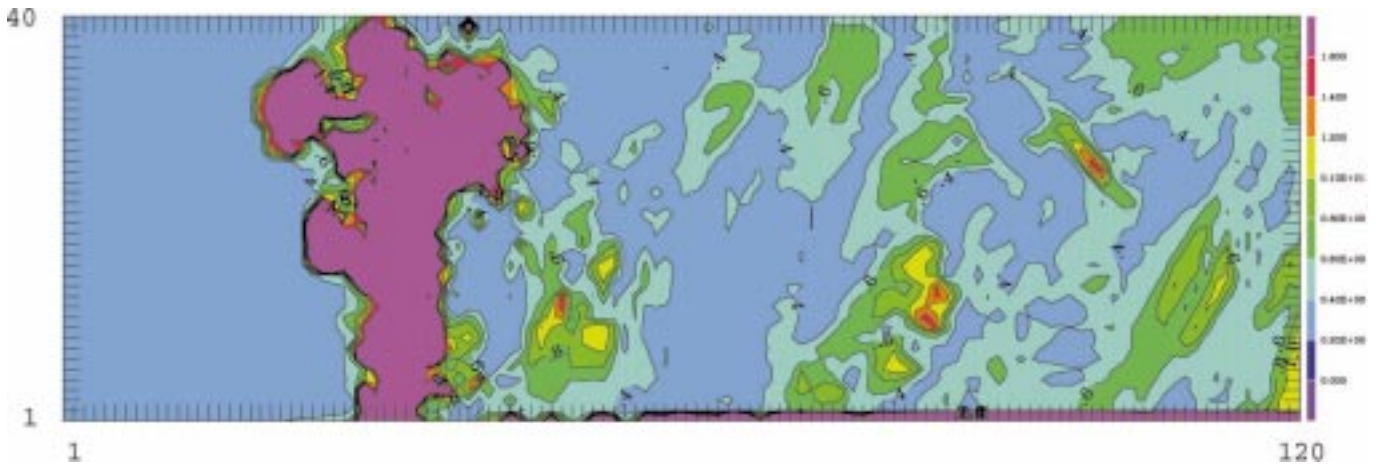


Figure 6: Sample Output of Seeing Mesoscale Modelling in the Paranal Area with the terrain model of Figure 5, colour scale is arbitrary, in units of FWHM (arcsec). The steep coastal slopes appear to strongly perturbate the optical steadyness of the airflow from the Pacific.

#### 4.2 Modelling seeing

Following earlier attempts by [Bougeault 95] of a mesoscale model applied on a mountainous continental site, a feasibility study has been started by [Masciadri 97] for the Paranal area using the recently developed non-hydrostatic model, meso-nh, including slight modifications appropriate to optical turbulence modelling. The model is non-hydrostatic, and as such allows the vertical development of orographic waves which are believed to be responsible of a large part of the night-time tropospheric seeing. Such waves indeed create areas with high kinetic energy (and thus well mixed air) at the boarder of which strong vertical gradients of the potential temperature constitute sheets of high optical turbulence.

One of the possible outputs of such a 3-D model shown in Figure 6, could obviously be useful during site surveys to exclude potentially unfavourable areas such as the immediate vicinity of the steep coastal slopes.

Tuning a model such as meso-nh is a complicated task because two parameters have to be minimised: the modelling error and the operational cost. Table

5 clearly illustrates the challenge. The cheapest configuration would allow several runs per night to be performed in an operational manner, while the two highest costs would simply forbid any operational use. Initial results of the study by [Masciadri 97] show that a simulated time of 30 minutes is often not sufficient to fully resolve terrain-atmosphere interaction, it is thus reasonable to assume that the cost of a simulation will be of the order of a few hundred DM.

#### 4.3 Forecasting wavefront isoplanaticity

*Assuming the decision is made to use adaptive optics, how far away from the*

*line of sight can a natural guide star be chosen? In case no convenient natural guide star is available for a given scientific object, will the cone effect be small enough to allow laser-guide-star operation?*

The answers depend on the relative vertical distribution of the turbulence expected above the observatory, expressed as an isoplanatic angle  $\theta_0$ :

$$\theta_0 = \left[ \int C_n^2(h) h^{5/3} dh \right]^{-3/5} \quad (1)$$

Let us assume that it is possible to model the vertical distribution of the index of refraction structure coefficient ( $C_n^2$ ) with an input vertical profile of tem-

Area (km)	Vert. Res. (m)	Horiz. Res. (m)	Simulated Time (sec)	Time Step (sec)	CPU Time (sec)	Price (DM)
60 × 20	300	500 × 500	1800	2.5	4629	1388
60 × 20	600	500 × 500	1800	2.5	1945	583
60 × 20	300	1000 × 1000	1800	5	719	215
60 × 20	600	1000 × 1000	1800	5	296	88
60 × 60	300	500 × 500	1800	2.5	13219	3965
120 × 120	600	2000 × 2000	1800	10	400	120

Table 5: According to the configuration chosen, the cost of a prediction (based on 1997 CRAY90 CPU charges) can vary by a factor of 50.

		1993			1989–1993
Site & hour	ECMWF	corr	err	err	err
Antofagasta 12GMT	Analysis	0.986	1.39	2.54	2.50
	24h For.	0.985	1.41	3.00	2.91
	48h For.	0.984	1.32	3.24	3.11
Quintero 12GMT	Analysis	0.991	1.15	2.48	2.52
	24h For.	0.989	1.35	3.39	3.25
	48h For.	0.988	1.37	3.96	3.71

Table 6: Averages of daily correlations, mean errors, and mean absolute errors of radio sounding temperatures against ECMWF analysis and 24/48-hour forecast during 1993 period and during the 1989–1993 period.

		m/s		
Site & hour	ECMWF	corr	err	err
Antofagasta 12GMT	Analysis	0.918	−0.36	2.11
	24h For.	0.813	−3.36	4.31
	48h For.	0.781	−0.24	5.09
Quintero 12GMT	Analysis	0.854	1.04	4.26
	24h For.	0.785	0.95	6.13
	48h For.	0.748	1.05	7.24

Table 7: Averages of daily correlations, mean errors, and mean absolute errors of radio sounding wind velocity against ECMWF analysis and 24/48-hour forecast during the 1993 period. The larger error at Quintero in 1993 is due to the blacklisting of this station from the ECMWF data assimilation scheme.

	Antofagasta		Quintero	
	1993	1989–1993	1993	1989–1993
Analysis	20%	21%	52%	31%
24h For.	48%	46%	98%	62%
48h For.	63%	58%	118%	80%

Table 8: Averages of daily relative unsigned errors of radio sounding wind velocity against ECMWF analysis and 24/48-hour forecast during 1993 period and during the 1989–1993 period. The larger error at Quintero in 1993 is due to the blacklisting of this station from the ECMWF data assimilation scheme.

perature measured locally by a radiosonde as described in Section 4.2. Could the radiosonde measurement be replaced by a forecasted temperature profile to obtain from meso-nh a forecast of the vertical profile  $C_n^2(h)$  above Paranal?

According to the conclusion of the evaluation of ECMWF forecast skill by [CRS4 97], summarised in Table 6, the temperature profile is accurately represented and correctly forecast at the two Chilean radiosonde launching sites. The question was raised if a profile obtained under the hydrostatic assumption could be used to initialise a non-hydrostatic model such as meso-nh. It was answered that although this would normally not be possible, the particular case of the Chilean coast was allowing this approximation: the general motion being eastwards, air masses are reaching the coast undisturbed by orography. The verification of this assumption is the object of the next phase of the study

by [Masciadri 97], comparing model results to actual  $C_n^2$  profiles measured from Paranal with balloon borne microthermal probes and by the SCIDAR technique.

#### 4.4 Forecasting Wavefront Temporal Characteristics

*Will the adaptive optics system be fast enough to follow the wavefront temporal evolution?*

The atmospheric seeing, expressed as the Full Width at Half Maximum (FWHM) of a long-exposure image at an aberration-free telescope (FWHM  $\approx \lambda / r_0$ ) is the cumulative effect of numerous sheets of refractive index perturbations all the way from about 20 km altitude down to the telescope enclosure (dome, mirror and instrument seeing are excluded from this section). Each turbulence sheet at altitude  $h$  has its own  $r_0(h)$  and moves with the wind at a velocity  $v(h)$  in the direction  $\theta(h)$ . If each sheet bears a fraction  $\alpha(h)$  of the total turbulence (as  $r_0$  varies as the  $-3/5$  power of the turbulence, we have  $\alpha(h) = [\frac{r_0}{r_0(h)}]^{\frac{5}{3}}$ ), the resultant wavefront corrugations horizontal velocity at ground level is

$$V_0 = \left[ \sum \alpha(h) v(h)^{\frac{5}{3}} \right]^{\frac{3}{5}} \quad (2)$$

and the coherence time will be proportional to the time needed for the wavefront to move by one coherence cell:

$$\tau_0 \approx 0.3 \frac{r_0}{V_0} \quad (3)$$

It is thus clear from Figure 7 that for a given seeing vertical distribution  $V_0$  will be much larger – and  $\tau_0$  much smaller – during austral winter. Moreover, 24-hour ECMWF predictions of wind velocity

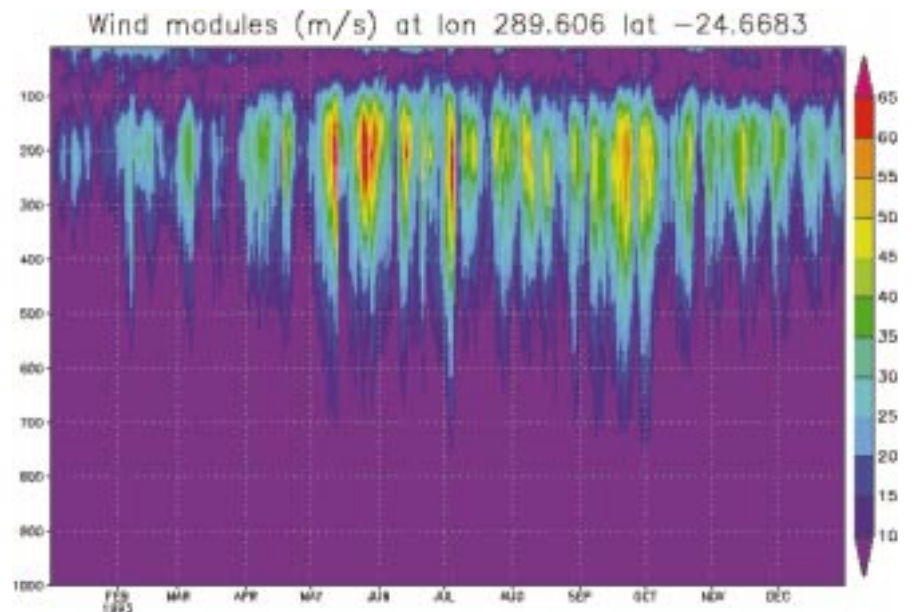


Figure 7: ECMWF wind velocity vertical profiles above Paranal: the period May to October is characteristic of potential jet stream development at 200 mB. The effect of high altitude wind is also noticeable down to the level of the VLT site (740 mB).

would as such, even with the 46% error displayed in Table 8, allow to classify the next night as potentially slow or rapid. Finally, considering the rather high correlation coefficients given in Table 7, it is believed that a statistical post-processing of the same type as described in Section 3.1 could also recover part of the systematic forecast errors.

### References

[Aussem 94] A. Aussem, F. Murtagh, M. Sarazin; Dynamical Recurrent Neural Net-

works and Pattern Recognition Methods for Time Series Prediction: Application to Seeing and Temperature Forecasting in the Content of ESO's VLT Astronomical Weather Station; *Vistas in Astronomy*, **38**, 357–374, 1994.

[Bougeault 95] P. Bougeault, Chen De Hui, B. Fleury, J. Laurent, Investigation of seeing by means of an atmospheric mesoscale numerical simulation, *Appl. Opt.*, **34**, 3481–3488, 1995.

[Erasmus 97] A. Erasmus, R. Peterson; The Feasibility of Forecasting Cirrus Cloud Cover and Water Vapour above Telescope Sites in Northern Chile; *PASP* **109**: 208–214, February 1997.

[CRS4 97] R. Deidda, M. Marrocu, A. Speranza; Feasibility Study of a Meteorological Prediction Model for ESO Observatories In Chile; *VLT Technical Report CRS-17443-0002*, Apr. 1997.

[Masciadri 97] E. Masciadri, J. Vernin, P. Bougeault; Feasibility Study of Seeing Prediction using the MESO-NH meteorological model: a progress report; *VLT Technical Report UNI-17400-0003*; March 1997.

---

Marc Sarazin  
msarazin@eso.org



**SUNSET ON PARANAL.** This photograph, recently taken on Paranal, shows that the VLT is taking shape.



## NEWS FROM THE NTT

G. MATHYS, ESO

At the time of this writing, the big-bang phase of the NTT upgrade project has just been completed, and the project is entering its third and final phase. Namely, operations have been resumed, according to a new model, pre-figuring the VLT operational model, and accordingly providing a test of the latter.

### The End of the Big Bang

The NTT page that appeared in the previous issue of *The Messenger* was written almost five months before the completion of the NTT big bang. Although all the fundamental components of the new control software had been implemented, a lot of debugging, fine-tuning, and testing remained to be carried out for many of them.

Both at the telescope and at the instrument level, and at the interface between them, the solution of quite a number of weaknesses or problems that we had had to carry along for a fairly extended period of time required the installation at the NTT of a new release of the VLT common software. This installation was performed in the second half of May. The outcome was a very significant improvement of the overall robustness and reliability of the system, as well as of the smoothness of its operation. It should also be stressed that, since the part of the software that is affected by these modifications is strictly common to the NTT and the VLT, the changes made in the new release in view of meeting the NTT needs also avoid future problems at the VLT. This illustrates the importance of the role of the NTT as a testbench for the VLT control system: many problems have already been detected and fixed prior to the installation of the system on UT1.

Other than that, most efforts on the telescope front have been directed towards the improvement of the image analysis and autoguiding software. Both are now much more robust and easier to use than a few months ago. Operation of the image analysis has evolved into a routine. For the user, this should translate primarily into the achievement of more predictable and stable image quality. In addition, through logging of the results of regularly performed image analysis, a better understanding of the optical behaviour of the NTT is building up, which in the long term should allow overall performance to be enhanced. For instance, it has already been dem-

onstrated (not surprisingly) that the autoguiding performs much better when the image quality has been optimised through proper use of the active optics. This illustrates the importance of the latter even within the framework of observing programmes such as point-source spectroscopy, where users in the past often tended to regard the execution of image analysis as useless or even wasteful (in terms of observing time).

The functionality of the autoguiding has been expanded. The autoguiding can now automatically select and acquire a guide star when the telescope is slewed to a new field. This process includes a check that the guide probe is not vignetting the field of view of the instrument CCD. Guide-star acquisition occurs at the position in the field viewed by the image analysis camera: accordingly, it can be used to run the image analysis in parallel with observation. As before the big bang, fully automatic combined offset is possible: when the telescope is offset by some amount, the opposite offset is applied to the guide probe, so as to recover the same guide star in the same location on the autoguiding camera. A new feature is that, if the motion required from the guide probe is to bring it outside its physical or vignetting position limits, the autoguiding switches to a new guide star, which it selects and acquires automatically.

On the optical side, in May, a new approach to mirror maintenance has been experimented with at the NTT, when the primary mirror was taken off the telescope and washed in its cell. This intervention, which was executed 38 weeks after the last aluminisation, restored the mirror reflectivity to its value of 18 weeks after aluminisation, and the micro-roughness of the coating to the value of 9 weeks after aluminisation. Contrary to aluminisation, washing does not require to take the mirror out of its cell and it can be done at the NTT (while for aluminisation, the mirror must be transported to the 3.6-m building). Therefore, it is both less delicate and less time-consuming: the whole operation, including rebuilding the pointing models once the mirror has been reinstalled on the telescope, can be completed in two days and two nights. Given the excellent results achieved in this first attempt, regular mirror washing seems to be a viable alternative allowing one to increase the spacing of mirror aluminisations while preserving the efficiency: accordingly, it is contemplated to repeat this operation at the NTT in the future. I take this opportunity to thank our colleagues of the La Silla Support Teams (in particular, Optics and Mechanics) who have assisted the NTT Team in this intervention.

At the time when the last issue of *The Messenger* was being prepared, the



Figure 1. View of the NTT control room during the first observing run after the big bang. From left to right are Visiting Astronomer Francesco Ferraro, Support Astronomer Chris Lidman, Instrument Operator Norma Hurtado, and Telescope Operator Hernán Nuñez.

EMMI control software was just undergoing first tests. This software, given the very complex nature of the instrument that it drives, is quite intricate, and its verification and debugging proved extremely demanding. As much time was required for the latter, some functionality was only added at a fairly late stage: dichroic mode for medium-dispersion (grating) spectroscopy, driving the punch tool for multi-object spectroscopy, and control of the calibration lamp. But the most troublesome part of the new EMMI control software proved to be the control panel, an extremely sophisticated graphical user interface. At the time of this writing, while all the functions of EMMI can now be regarded as controlled in a quite satisfactory manner, the control panel still shows on occasion some apparently erratic behaviour. This is regarded as a minor drawback, since this panel is mostly used for engineering purposes, and not generally to drive the instrument in normal operating conditions: indeed, scientific observations are primarily carried out through the high-level operating software, via templates (of which more below).

On the other hand, recurrent problems have been met throughout the EMMI commissioning with the CAMAC motor controllers. Only those of our readers with the deepest knowledge of the NTT upgrade project will remember that, early on, it had been decided that while the electronic controllers of all other NTT subsystems would be replaced by VLT standard modules, the CAMAC controllers of EMMI would be kept and they would be interfaced to the rest of the system through a layer of software making them look like VLT standard. Financial and manpower constraints fully justified that decision, which unfortunately now appears as a major source of trouble. The problem could not be tackled during the big bang due to lack of time, and it is being investigated at this very moment. The current approach consists in studying operational workarounds that will limit or cancel the impact of the problem on scientific observations, since a solution at a more fundamental level cannot be envisaged in the short term.

By contrast with EMMI, SUSI had already long ago reached a fairly stable state (thanks, of course, to its much greater simplicity). Work done on the SUSI control software over the last months has been mostly cosmetic, with in particular the implementation of a new control panel which looks much more similar than the previous one to the control panel of EMMI.

The bad news for SUSI come from the CCD, the newly installed Tektronix #42, whose charge transfer efficiency drops, causing image smearing, above levels of 60,000 e<sup>-</sup> for slow readout, and of 110,000 e<sup>-</sup> for normal and fast readout (with the settings currently offered to us-

ers). This problem appears to affect all the CCDs of that type, but the level at which it starts is lower for #42 than for other similar chips on La Silla. There is no easy solution apart from the replacement of the CCD. No adequate spare being available for the time being, CCD #42 will be left on SUSI until the instrument is decommissioned to be replaced by SUSI-2 at the end of 1997. Users will accordingly be warned against observation at too high levels.

The end of the big bang has suffered not only from the technical difficulties reported above, but even more of the unusual extended period of very bad weather on La Silla in May and June. During the latter, it was not only impossible to do any observation at all for about one month, but in addition, on several instances, it proved impossible to move the building closed because of the extreme strong wind, or even to drive the telescope or the instrument inside the building as water leaks forced us to keep them parked, covered with plastic protections. These circumstances have, of course, severely hampered our attempts to complete the verification and commissioning of the control system. They have had an even worse impact on the development of operational tools and procedures.

Operations of the NTT are intended to be fully embedded in an end-to-end data flow model. At the front end of the data flow, the user whose programme has been approved by the OPC, goes through a Phase 2 Proposal Preparation (P2PP) process, during which with the help of a sophisticated software tool (also called P2PP) he defines Observation Blocks (OBs). An OB can be seen as the smallest complete description of an observation. OBs are stored in a database, from which they are passed to the high-level operating software (aka Bob, Broker of Observation Blocks) by the Observing Tool (OT). Bob uses the information contained in the OB to trigger the execution of a series of templates, or sequencer scripts. The latter are essentially sequences of commands that are passed to the telescope, instrument, and detector control systems. While P2PP and OT have been developed by the Data Management Division (DMD), and Bob is part of the VLT common software, the specific templates for EMMI and SUSI were to a large extent created by the NTT Team. From the description above, it must be clear that proper certification of the templates requires that the underlying control system is operational: given the delays that have affected the latter, it can be understood that templates could not be as fully tested and debugged as one might have hoped. Consequently, the first post-big-bang NTT users have faced and still should expect to face on occasion some difficulties in the use of the templates. (I would like to apologise here for the in-

convenience). The latter should be kept to a minimum thanks to the fact that the know-how about the templates is fairly widespread among the members of the NTT Team supporting daily operations.

At the back end of the data flow, the original design was to have a copy of the CCD frames, after readout and storage in the instrument workstation, forwarded directly to an archive machine, and from there to a pipeline workstation and a user workstation. The former is to be used for on-line standard (pipeline) processing of the data, while the latter is at the disposal of the astronomer for analysis of his observations using some standard image processing software (for the time being, IRAF and MIDAS are available). The whole transfer chain, as well as most of the pipeline and associated quality control products, are being developed by the DMD. For very much the same reasons already mentioned, however, the transfer chain could not be brought into a stable operational state yet, so that its implementation had to be postponed. Instead, as a provisional workaround, a simpler tool, offering less functionality, has been installed by the NTT Team to transfer data from the instrument workstation to the astronomer and pipeline workstations. The pipeline processes, which appeared to be working reliably (although still fairly rudimentary algorithms were used for data processing), are being modified to allow them to ingest input from the simplified transfer chain. Once this is successfully completed, the change should be mostly transparent to the user. But there will be no on-line connection to the archive: accordingly archiving of the data is, for the time being, based on tape copies sent by courier service from Chile to Germany.

The execution in service mode of some shared-risk observations with SUSI which had started in February, continued through March and April. Distribution of the corresponding data is currently in progress. Regrettably, the already described delays due to technical and meteorological factors have later on prevented the NTT Team from executing many of the service observing programmes that had been approved by the OPC for the first half of Period 60 (in particular with EMMI). Even though there was no definite commitment to deliver data during that period, we would have strongly wished to obtain at least some observations then, to acknowledge the confidence placed in us by the applicants and the efforts made by them for programme preparation, as well as to gain practice in operations. I can only reiterate here the apologies that the affected investigators have already received through personal letters.

## Back to Operations

On June 27, as had long been foreseen, the NTT went back into normal

operations. The first few observing runs had been scheduled for classical observing. The first Visiting Astronomer to come back to the NTT after the big bang was Dr. Francesco Ferraro. Figure 1 shows a view of the renovated control room during this first run.

It is too early to draw conclusions from the first observing runs at the NTT after its reopening: this will be left for a next issue of *The Messenger*. It may be sufficient here to mention that if these runs were affected by some minor hiccups, as could be expected after such a long suspension of operations and given the difficulties encountered in the last phase of the big bang, the general behaviour of the system revealed no major flaw. The users so far have generally expressed an overall satisfaction, assorted with a number of constructive suggestions. The latter are extremely valuable to us, especially since the current NTT prefigures the VLT. Thus we are urging our users to tell us what they like and dislike in the current NTT, so as to enable us to shape the VLT more to their taste.

## Personnel Movements

The transition of the NTT from a stage of technical development work to regular operations has been accompanied by a change of leadership. Jason Spyromilio, who had been NTT Project Scientist since September 1995, has left the NTT team and his function has been taken over by the author of these lines. The key role played by Jason in the successful completion of the NTT big bang cannot be overstated. His dedication to the project, his indefatigable activity towards its achievement, and his extreme competence have been examples and catalysts for the work of all team members. Jason is now headed towards the VLT, where he is to lead the commissioning team. On behalf of the NTT Team, I wish him the best of success in this new challenge.

At the same time, Anders Wallander has left the NTT Team too. One of the members of the team since its creation in 1993, Anders, as chief engineer of the upgrade project, has been instru-

mental in its technical achievements. He now is back in the VLT software group, where the experience that he has accumulated through his work for the NTT will without doubt prove extremely valuable.

Finally, I am taking this opportunity to welcome Chris Lidman in the NTT Team, where he is taking the position of staff astronomer left vacant by the departure of Roland Gredel to the team in charge of the 3.6-m telescope and of the CAT at the beginning of the NTT big bang. Chris, who was until then a postdoc in the La Silla medium-sized telescope team (aka 2.2 team) where he was in charge of the IRAC instruments, will in the NTT Team assume the responsibility of SOFI instrument scientist. Until the latter comes on line, Chris is sharing the load of astronomical support of EMMI and SUSI with the other astronomers of the team.

---

Gautier Mathys  
gmathys@eso.org

## ESO at the Leipzig Fair

Thanks to the hospitality of the German Federal Ministry of Education and Research, ESO was able to entertain a 60 square metre information stand at the "Forschungsforum '97", held in connection with the INNOVATION Fair at Leipzig's impressive, new Fair grounds from September 16–20.

The stand itself had a circular layout with a diameter of 8.2 metres and featured a model of the VLT, ESO videos, Internet connection and colour panels with text and graphics. An 8-metre panorama photo of the Milky Way formed the background and provided an ample setting for the display.

The first day was dedicated to the youth, and about 5,000 young people passed the counters, eager to learn about the latest results and ideas in the numerous areas of fundamental and applied research that came together at the Research Forum.

Three ESO staff members were busy during the day answering questions from the



many visitors. It was evident that many of the young people were informed about the VLT project and did not want to miss the opportunity to ask very specific questions to the ESO staff present.

Later in the day, the extensive programme of public lectures included talks by ESO astronomers focusing on VLT science and the issue of Astronomy and the Youth.

Also during the following days, the ESO stand was well visited. Among the many visitors were the Mayor of Leipzig, high-ranking officials from the German Federal Ministry of Education and Research and representatives from industry. Physics teachers spent substantial time on the stand, browsing through the ESO Web pages about the VLT as well as Astronomy On-line.

C. MADSEN

# Tidal Dwarf Galaxies

P.-A. DUC, ESO

I.F. MIRABEL, SAp, Centre d'Études de Saclay, CEA, France

## 1. Introduction

The birth and evolution of galaxies are dramatically affected by environmental effects. Interactions with the intergalactic medium and collisions with companions cause major perturbations in the morphology and content of galaxies. As a result, late-type spirals may evolve into early-type spirals or even ellipticals. In “bottom-top” models, larger structures form from the agglomeration of smaller entities, and small galaxies would be swallowed by giant galaxies.

A more exotic – and somehow reversed – way of forming galaxies was

put forward by Schweizer (1978) and more recently by Mirabel et al. (1992), who found evidence for the genesis of a dwarf galaxy out of material removed from the interacting system NGC 4038/39. The idea that parent galaxies could give birth to dwarf galaxies goes back to the sixties, when the first photographic catalogues of extragalactic “perturbed” objects were published (Vorontsov-Velyaminov, 1959; Arp, 1966). These systems show numerous luminous clumps, attached to giant galaxies by jet-like thin filaments. At that time, some authors (Ambartsumian, 1961; Arp, 1972), invoking nuclear processes simi-

lar to those responsible for radio jets, claimed that giant galaxies could “eject” in the intergalactic medium a substantial part of their stellar mass. The crucial role of interactions and gravity was better understood when numerical simulations (e.g. Toomre & Toomre, 1972) demonstrated how tidal forces shape the stellar structures of interacting systems, creating tails, bridges and shells. Recent studies, based on optical and HI observations, have shown that debris of collisions actually form a class of “recycled” or “second-generation” galaxies that has several properties in common with classical dwarf galaxies: blue compact (BCDGs) or irregulars (dlrrs). Because they are mostly found in tidal tails, they are now commonly referred as “tidal dwarf galaxies” (hereafter TDGs).

We report here the results of a multi-wavelength campaign on tidal dwarfs carried out at La Silla, with several telescopes and instruments. Our aim was to identify and characterise objects of tidal origin in the environment of nearby interacting systems.

## 2. Observations

The optical observations were carried out using EFOSC1 on the 3.6-m and EMMI on the NTT, during several runs between 1992 and 1995. Deep large-field BVR images were first taken. We identified in tidal features associated with colliding galaxies blue condensations, and obtained spectra of each of them using multi-object spectroscopy techniques. For each field, one mask containing 20–30 slits had been punched. We used the low-resolution grism #3 in the RILD mode of EMMI. Despite several false alarms – background galaxies with discrepant redshifts – we found in almost all systems between one and ten tidal dwarfs, exhibiting recent star formation revealed by the presence of ionised gas. In order to study the stellar populations of tidal dwarfs, and their star-formation history, we started in February 1996 a near-infrared imaging programme. JHK' images were taken with IRAC2B on the ESO/MPI 2.2-m. Because of the relatively small field of view offered by this camera (2' with the lens LC), compared to the typical size of our objects (10'), we had to mosaic the field and therefore could map only few systems. In that respect, much observing time will be gained using SOFI, the next-generation



Figure 1: A tidal dwarf in the prototype interacting system NGC 4038/39 (The Antennae): This classic system is composed of two overlapping, distorted, late-type spiral disks. The two nuclei seen in the near-infrared  $K'$  image (inset) are separated by 15 kpc. More than 60% of the HI (green contours) is distributed along the tails. The object at the tip of the southern antenna shows a chain of HII regions, embedded in a low-surface brightness envelope (Mirabel et al., 1992). Optical image from the Digital Sky Survey; infrared image taken with IRAC2; HI contours from Hibbard et al. (1997). The field of view is  $17.7' \times 19.5'$ .

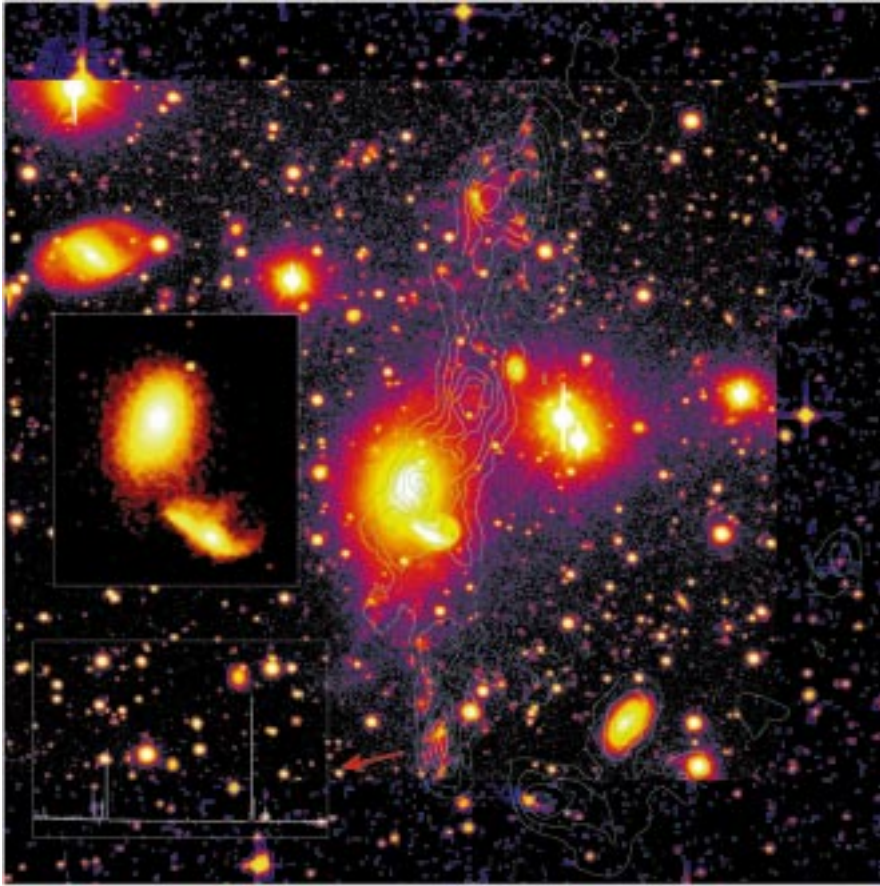


Figure 2: Very young tidal dwarfs in NGC 5291, an S0 with a huge HI ring: This lenticular galaxy is associated with a massive HI ring (green contours), perhaps formed after a high-speed collision with the disturbed object near the S0 (The “Seashell”). The inset shows a near-infrared K’ image of the colliding galaxies. Associated to the HI clumps in the ring are found very blue ( $B-V < 0.3$ ) optical counterparts. Multi-object spectroscopy reveals that they host active star-forming regions (see HII-like spectrum at the bottom-left). Optical R image and spectrum obtained with EMMI, K’ image with IRAC2; HI from Malphrus et al. (1995). The field of view is  $9.2' \times 8.7'$ .

ESO infrared camera, to be installed next year on the NTT. In one of its modes, SOFI will offer a  $5'$  field. Our IRAC2 observations have already shown that low-surface brightness tidal tails can be detected up to  $2.2 \mu\text{m}$  even on a 2.2-m telescope.

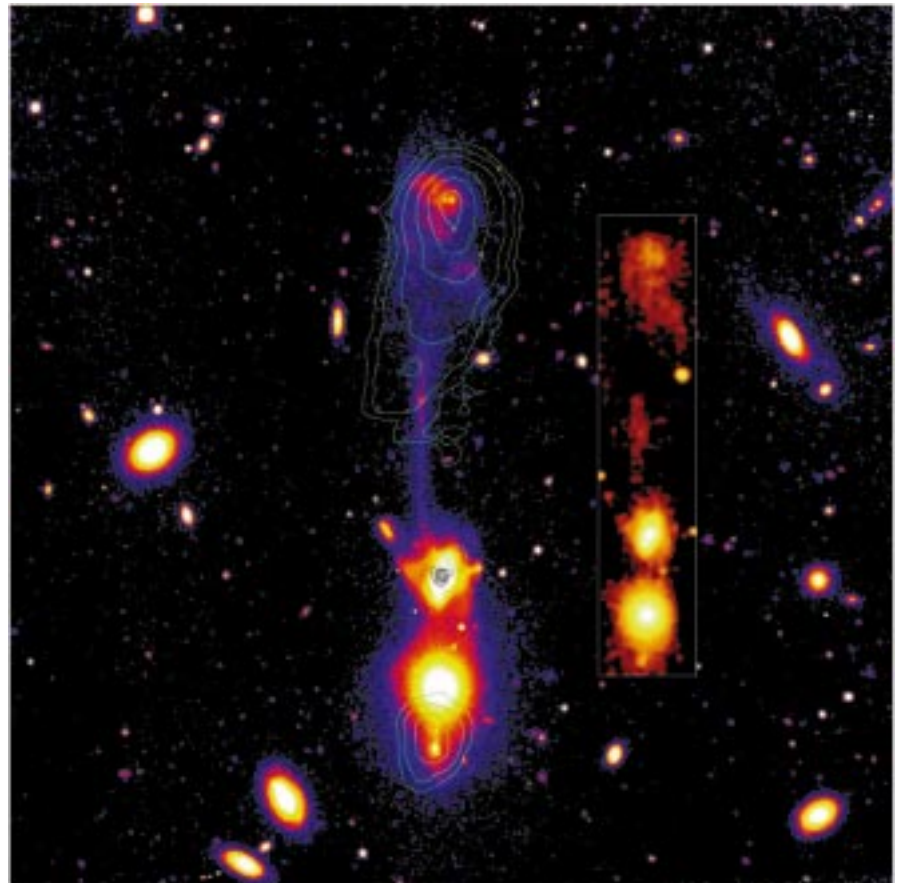
This optical and infrared work was complemented by radio observations of the atomic hydrogen, carried out with the Very Large Array interferometer, either by our group or other researchers, who kindly provided us with the data-cubes.

As test cases, we present in Figures 1–4 different examples of interactions: spiral-spiral collisions (NGC 4038/39 or “The Antennae”, Fig. 1; NGC 2992/3, Fig. 4) and spiral-elliptical encounters (NGC 5291, Fig. 2; Arp 105, “The guitar galaxy”, Fig. 3). On the optical NTT im-

ages, long tidal tails are clearly seen emanating from the parent galaxies. At their tip, at a distance of 50–100 kpc

from the nuclei, we found small irregular objects. Their absolute magnitude is in the range of dwarf galaxies. They host blue compact clumps that we identified with star-forming regions. Their spectra show emission lines, typical of HII regions, ionised by massive OB stars younger than 10 Myrs. Given the time scale for the formation of clumps in tidal tails – typically 1 Gyr (Barnes & Hernquist, 1992) – the young stars at the end of the antennae must have been born *in situ*. In Figures 1–3, the contours of the HI column density are superimposed in green on the CCD images. It is striking on these images that the central regions of the parent galaxies contain little atomic gas, whereas the optical tails, and especially the tidal dwarfs, are associated with HI clouds as massive as  $5 \times 10^9 M_{\odot}$ . Such a gas distribution in interacting

Figure 3: A gravitationally bound tidal dwarf in the spiral-elliptical colliding system Arp 105: The diffuse object at the end of the 70-kpc long tidal tail escaping from the spiral is as luminous as the LMC/SMC. The  $6 \times 10^9 M_{\odot}$  HI cloud associated with the tidal galaxy shows evidence of rotation. Another tidal dwarf is seen south of the elliptical. Note in that system the extreme spatial segregation between the atomic (green contours) and molecular gas (black contours). V band image obtained with EMMI, near-infrared J-band image (inset) with IRAC2; HI and CO from Duc et al. (1997). The field of view is  $7.5' \times 7.5'$ .



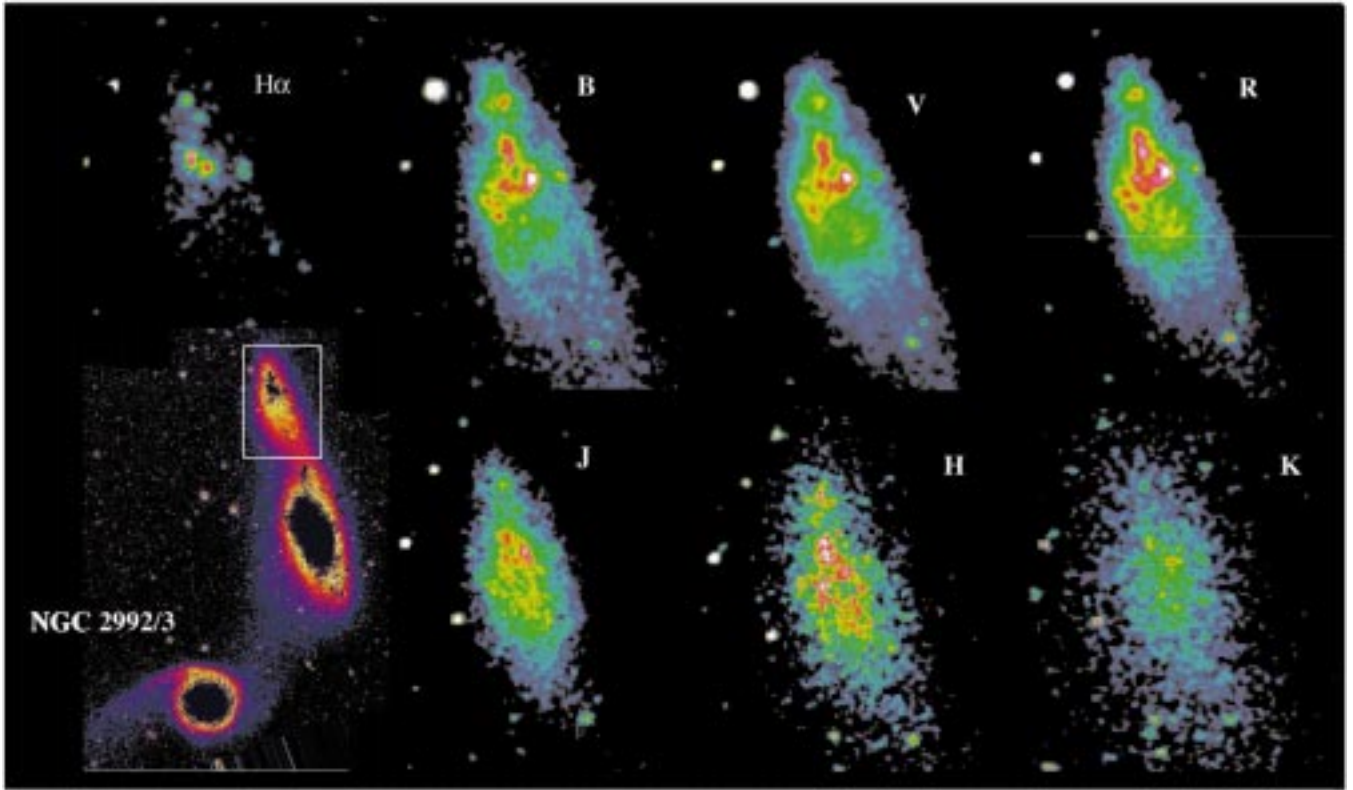


Figure 4: A tidal dwarf in the tail of the spiral-spiral colliding system NGC 2992/3. This figure displays multi-band images of the northern tail of NGC 2992. The spectral energy distribution of the tidal dwarf is dominated by old stars, formed in the disk of the parent galaxy. Optical images obtained with EMMI, near-infrared images with IRAC2.

systems seems to be quite general (Hibbard & van Gorkom, 1996). Above a critical HI column density between  $5 \times 10^{20} \text{ cm}^{-2}$  and  $10^{21} \text{ cm}^{-2}$ , we detect emission lines from gas ionised by massive stars.

### 3. Properties of Tidal Dwarf Galaxies

#### 3.1 Stellar populations

Tidal dwarf galaxies are made of two main stellar components: young stars recently formed by collapse of expelled HI clouds, and an older stellar population, at least 1 Gyr old, which was pulled out from the disk of the parent galaxies. Aperture photometry measurements, coupled with evolutionary synthesis models, allowed us to derive the proportion and age of both populations. Figure 5 displays on a V-K vs B-V diagram the near-infrared and optical colours of TDGs and for comparisons photometric measurements for the outer regions of their parent galaxies. Although our data-base is still limited, this figure shows that there may be a diversity of tidal dwarfs. On one hand, we find TDGs dominated by old stars with integrated colours comparable to those of the outer disk of their parent galaxies (e.g. NGC 2992, Fig. 4). In this type of objects, the recent star-formation episodes did not affect much the overall stellar population, and the K-band flux traces red giants. On the other hand, we find TDGs

having extremely blue colours ( $B-V < 0.3$ ;  $V-K \sim 2$ ) (e.g., NGC 5291, Fig. 2), with no compelling evidence for the presence of an underlying old stellar population. In this case, the K light comes mainly from red supergiants younger than 20 Myrs.

Therefore, some tidal dwarf galaxies in the nearby Universe are instances of genuine young galaxies that are forming their first generation of stars. This class of objects are usually sought in the early distant Universe, where detailed studies are difficult. It has been debated whether

another class of galaxies, the blue compact dwarf galaxies (BCDGs), are also of recent origin. A sample of them has been added in Figure 5. Although the B-V colour of BCDGs and TDGs are similar, their V-K index seems to differ quite significantly. This could be explained by a metallicity effect. The V-K colour of a starburst depends strongly on the metallicity during the first 20 Myrs (Cerviño & Mas-Hesse, 1994). Classical BCDGs born in primordial HI clouds are metal deficient objects (commonly  $Z < Z_{\odot}/10$ ), whereas TDGs are formed from

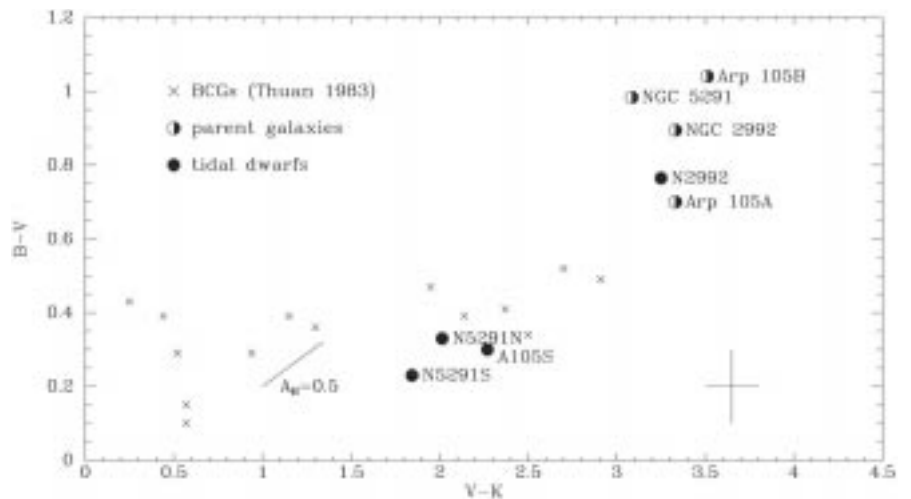


Figure 5: Colour-colour diagram of tidal dwarfs. For reference, the colours of the outer regions of the parent galaxies are also indicated. A sample of blue compact dwarfs has been added.

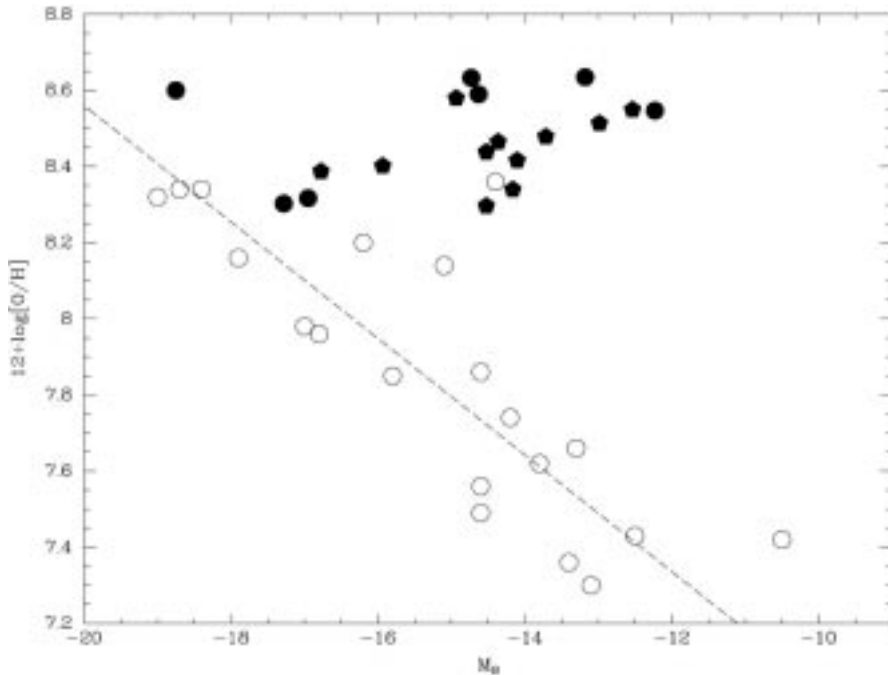


Figure 6: Oxygen abundance vs absolute blue magnitude for our sample of tidal dwarfs (black points) and a sample of isolated dwarf irregular galaxies (open points; from Skillman et al., 1989).

recycled material – material which has been pre-enriched in the disk of their parent galaxies – and therefore should be more metal-rich. This is consistent with the relatively high oxygen abundances we estimated in the HII regions of TDGs:  $Z_{\odot}/3$  on average, a value typical of the outer regions of spirals. A clear result from our spectral analysis is that tidal dwarf galaxies do not follow the classical correlation found for field dwarf and giant galaxies between luminosity (hence mass) and metallicity, as shown in Figure 6.

### 3.2 Dynamics

Radio observations of the 21-cm HI line can be used to derive the dynamics of the gas. Unfortunately, most tidal dwarfs found so far have small angular sizes compared to the radio synthesised beams of the interferometers and the detailed study of the line profiles is difficult. However, there is a tidal dwarf where has been found evidence for rotation (Duc et al., 1997a) suggesting some sort of dynamical independence. Because of the low surface brightness of TDGs, the knowledge of the stellar dynamics derived from absorption lines is still beyond the scope of the current instrumentation. However, we expect that an IR spectrometer like ISAAC, to be installed on the first unit of the ESO VLT, will achieve the required sensitivity. An obvious by-product of these kinematical studies will be the determination of the TDG dark-matter content, which is expected to be low in the numerical simulations by Barnes & Hernquist (1992).

## 4. Formation of Tidal Dwarf Galaxies

It is known that interactions trigger star formation (e.g. Kennicutt et al., 1987). However, until the discovery of the tidal dwarf galaxies, this phenomenon had been observed mostly in the central regions of merging galaxies. For instance, almost all ultraluminous infrared galaxies, which host violent nuclear starbursts, are close interacting galaxies (see review by Sanders & Mirabel, 1996 and Duc et al., 1997b).

How can collisions induce star-forming episodes at distances as high as 100 kpc from the galactic nuclei? The related mechanism involves mass transfers mostly driven by gravitational forces. Following the interaction, a fraction of the atomic hydrogen loses its angular momentum, sinks into the central regions where it may be transformed into molecular gas, fuelling a nuclear starburst or an AGN. Another part of the HI, initially situated in the outer regions of the disk and therefore less gravitationally bound to the galaxy, is stretched and tidally pulled out into the intergalactic medium, supplying the material that leads to the formation of tidal dwarf galaxies.

The relative proportions of old and young stars that we derive from our observations are an important constraint for the models of TDG formation. Models based on numerical simulations of colliding systems favour two mechanisms: a local dynamical instability in the old stellar populations of tidal tails, followed by accretion of gas (Barnes & Hernquist, 1992) or collapse of a supermassive cloud triggering precipitous star-forma-

tion activity (Elmegreen et al., 1993). The two scenarios predict a different fraction of old to new stars.

## 5. The Fate of Tidal Dwarf Galaxies

Do tidal dwarf galaxies contribute significantly to the overall population of dwarf galaxies? The answer to this fundamental question relies, from a theoretical point of view, on the knowledge of two critical parameters: (1) the frequency of galactic interactions, believed to be increased with redshift; (2) the survival time of tidal dwarfs. The latter is limited by the hostile environment of TDGs, in the vicinity of giant parent galaxies. They may fall back on their progenitors, as pointed out by Hibbard & Mihos (1995), or be tidally disrupted. In this respect, the indication that some TDGs are gravitationally bound (Duc et al., 1997a; Hibbard et al., 1997) suggests the possibility of a longer life expectancy.

From an observational point of view, the census of TDGs is not an easy task. TDGs should obviously be searched in the environment of interacting galaxies. Optical images taken recently with SUSI during the Big-Bang period of the NTT disclose tens of new tidal dwarf candidates around several colliding galaxies. Hunsberger et al. (1996) claim from the analysis of photometric data that half of the dwarf galaxies in an Hickson compact group could be of tidal origin. However, one should note that once the stellar/gaseous bridge between the parent and child galaxies has dissipated, it is difficult to re-establish a link between the two. Our study has shown that a good genetic fingerprint of TDGs is their high metallicity. In this respect, several studies have put forward trends for dwarf galaxies in groups or clusters to be more metallic than field dwarfs (Bothun et al., 1985; Vilchez, 1995). Since the collision rate is enhanced in denser environments, it is tempting to argue that a significant fraction of dwarfs in clusters could be recycled objects. We are currently carrying out at La Silla an imaging and spectroscopy survey to quantify this effect in the Hydra cluster. A bimodal star-formation history is also a strong signature for tidal dwarfs. Evolutionary Synthesis Models simulating a burst of star formation on top of the underlying component of old galaxies reproduce well the TDG star-formation history and will give constraints for their future evolution.

**Acknowledgements.** We are grateful to all students, fellows and staff people at La Silla for their invaluable help during the introductions. Special thanks to Chris Lidman for providing helpful tips for the acquisition and reduction of infrared images.

## References

- Ambartsumian, V.A.: 1961, *AJ* **66**, 536.  
 Arp, H.: 1966, *Atlas of Peculiar Galaxies*, California Institute of Technology, Pasadena.  
 Arp, H. C.: 1972, in D.S. Evans (ed.), *External Galaxies and Quasi Stellar Objects*, Vol. **44**, p. 380, IAU symposium.  
 Barnes, J.E. & Hernquist, L.: 1992, *Nature* **360**, 715.  
 Bothun, G.D., Mould, J.R., Wirth, A., & Caldwell, N.: 1985, *AJ* **90**, 697.  
 Cerviño, M. & Mas-Hesse, J.M.: 1994, *A&A* **284**, 749.  
 Duc, P.-A., Brinks, E., Wink, J.E., & Mirabel, I.F.: 1997a, *A&A*, **326**, 537.  
 Duc, P.-A., Mirabel, I.F., & Maza, J.: 1997b, *A&A Sup* **124**, 533.  
 Elmegreen, B.G., Kaufman, M., & Thomasson, M.: 1993, *ApJ* **412**, 90.  
 Hibbard, J., van der Hulst, J., & Barnes, J.: 1997, in preparation.  
 Hibbard, J.E. & Mihos, J.C.: 1995, *AJ* **110**, 140.  
 Hibbard, J.E. & van Gorkom, J.H.: 1996, *AJ* **111**, 655.  
 Hunsberger, S.D., Charlton, J.C., & Zaritsky, D.: 1996, *ApJ* **462**, 50.  
 Kennicutt, Robert C.J., Roettiger, K.A., Keel, W.C., Van der Hulst, J.M., & Hummel, E.: 1987, *AJ* **93**, 1011.  
 Malphrus, B.K., Simpson, C.E., Gottesman, S.T., & Hawarden, T.G.: 1995, *BAAS* **187**, 5102.  
 Mirabel, I.F., Dottori, H., & Lutz, D.: 1992, *A&A* **256**, L19.  
 Sanders, D.B. & Mirabel, I.F.: 1996, *ARA&A* **34**, 749.  
 Schweizer, F.: 1978, in E. Berkhuysen & R. Wielebinski (eds.), *Structure and Properties of Nearby Galaxies*, p. 279, Dordrecht, D. Reidel Publishing Co.  
 Skillman, E.D., Kennicutt, R.C., & Hodge, P.W.: 1989, *ApJ* **347**, 875.  
 Thuan, T.X.: 1983, *ApJ* **268**, 667.  
 Toomre, A. & Toomre, J.: 1972, *ApJ* **178**, 623.  
 Vilchez, J.M.: 1995, *AJ* **110**, 1090.  
 Vorontsov-Velyaminov, B.: 1959, *Atlas and Catalogue of Interacting Galaxies*, Sternberg Institute, Moscow State University, Moscow.

P.-A. Duc  
 pduc@eso.org

# The Activity of Comet 29P/Schwassmann-Wachmann 1 Monitored Through the CO J(2–1) Emission Line at 230 GHz

M.C. FESTOU<sup>1</sup>, M. GUNNARSSON<sup>2</sup>, A. WINNBERG<sup>3</sup>, H. RICKMAN<sup>2</sup>, G. TANCREDI<sup>4</sup>

<sup>1</sup>Observatoire Midi-Pyrénées, Toulouse, France; <sup>2</sup>Astronomiska Observatoriet, Uppsala, Sweden; <sup>3</sup>Onsala Rymdobservatorium, Sweden; <sup>4</sup>Universidad de Montevideo, Uruguay

*CO J(2–1) emission from comet 29P/Schwassmann-Wachmann 1 at 230 GHz was observed on 16 occasions with the 15-m SEST antenna from 4 December 1996 until 2 January 1997. A clear signal was detected in all daily averaged spectra, and day-to-day nuclear output variations by a factor  $\sim 2$  were observed. Whatever the position of the telescope main beam in the coma, the line position and shape showed remarkably stable characteristics, which justified to combine the spectra to produce line profiles with S/N greatly enhanced over previous observations of the same kind. While most of the outgassing occurs from the sunlit side of the nucleus, night-side emission is also present. The shape of the lines near zero velocities in offset spectra cannot yet be uniquely interpreted. Whatever the ultimate model proposed to explain these observations, important implications for our understanding of how CO molecules are stored in the nucleus and later released into the coma may be derived from this data set.*

Comet 29P/Schwassmann-Wachmann 1 (hereafter designated as SW1) was long the only object of proven cometary nature found to orbit the Sun entirely outside the orbit of Jupiter, at an average distance of  $\sim 6$  AU. Rickman speculated in 1985 that Chiron, an object of apparently cometary nature and giant size, only physically observable with large-size telescopes, could be one of the largest members of an unseen population of comets orbiting the Sun between the orbits of Jupiter and Neptune<sup>1</sup>. In recent years, an ever-growing number of solar-system objects have been discovered that are also constantly situated far from the Sun. They form the now called Centaur and Kuiper Belt (KB) families, two groups of bodies that circulate between the orbits of Jupiter and Neptune and on average beyond that of Neptune, respectively. From a dynamical point of view, the Centaurs may be escapees from the Kuiper Belt. While the true nature of these newly discovered objects still remains to be unveiled, the current thinking is that they are the largest members of a vast reservoir of potential comets proposed by Fernan-

dez<sup>2</sup> in 1980 to provide an important additional source of short-period comets beside the Oort cloud. The Centaur and KB populations should contain numerous small comets that are not observable with today's instruments. It is currently impossible to state whether SW1 was captured from the Oort cloud or the KB. In the light of all these new developments on the origin and evolution of orbits of comets, SW1 undoubtedly is a unique object that deserves attention besides the interest it has always aroused for its peculiar brightness behaviour.

SW1 is known since its discovery

in 1927 for its numerous and unpredictable bursts of activity, some of which bring its magnitude down to 10–11 from a state of much lower brightness long

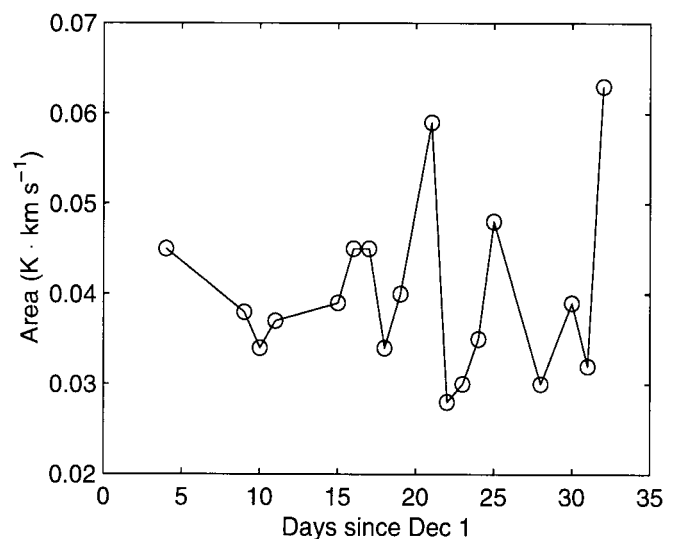


Figure 1: CO production in comet SW1 measured during the month of December 1996. The comet was observed during a period we can qualify, based on the comet total magnitude, as of "low" or "minimal" activity, the so-called "quiescent state".

thought as being a “dormant state”. The comet would be inactive most of the time and would become suddenly, say every two months or so, much brighter, the indisputable proof that its nucleus is active. A dust coma would then form, driven by an unseen gas. Spectroscopic observations of comets indicate that water is the most abundant volatile species in their nuclei, and laboratory data further indicate that water should not sublimate at distances from the Sun larger than 4–5 AU. However, it is not uncommon for comets observed at distances from the Sun larger than this limit, both on the incoming and outgoing branches of their orbits, to display a well-developed dust coma. C/Hale-Bopp (1995 O1) is the most recent example – and how famous! – of an object moving towards the Sun from remote neighbourhoods, that has consequently not been heated since long, and that displays activity when water cannot escape its nucleus<sup>3,4</sup>. A

question of paramount importance is thus “what is the nature of the outgassing agent that controls the activity of distant comets and how can this gas leave the nucleus?”. One would normally expect a dust mantle and/or water ices to block the way towards the surface. One can see now the key role played by comet SW1, possibly a pristine and relatively unevolved object. Like all objects never coming closer to the Sun than  $\sim 5$  AU, its nucleus is subject to only mild heating, and its surface temperature never goes beyond that of the water sublimation threshold.

In 1987–88, a large set of CCD images of comet SW1 was obtained by Jewitt<sup>5</sup>, which showed that the comet was permanently active and always surrounded by a dust coma, even when its magnitude was near a maximum value of  $R \sim 16.5$  (maximum magnitudes previously derived from photographic plates<sup>5</sup> – nearly equivalent to B magnitudes – are of order 18–19 and underestimate the true comet brightness by  $\sim$  one unit<sup>6</sup>). The nature of the outgassing agent in SW1 is known since 1994, when CO was detected for the first time

by Senay and Jewitt<sup>7</sup> from the JCMT by its emission at 230 GHz, based on a prediction made by Crovisier a year earlier<sup>8</sup>. The Meudon cometary team confirmed this important observation a little later<sup>9</sup>. These two data sets reveal that the CO line is very narrow and blue-shifted by  $\sim 0.4$  km s<sup>-1</sup>. An isotropically emissive coma would produce a line centred on

15-m diameter antenna, was designed to extend the previous observations over a significantly longer period of time and to determine what the normal “gaseous” state of activity of the comet was. Our main objectives were to measure the CO production on a daily basis for about 30 days, fully define the CO line parameters (width and line position), establish the reality of a night-side outgassing and, if possible, observe an outburst in progress.

Monitoring of the CO J(2-1) line began on 4 December 1996 and ended on 2 January 1997 and data were collected on 16 different days. The average time spent with the source in the telescope beam was of the order of 90 minutes per day. The comet was detected in all daily averaged spectra at a level of 0.04–0.08 K km s<sup>-1</sup> with a S/N intermediate between that obtained with the JCM and IRAM antennae. It was found that the day-to-day variability of its CO production rate

was about 2 (Figure 1 shows the production curve derived from our daily averaged “ON” spectra, assuming a nuclear source of CO, details on the model we used are given below). CCD images taken with the 1-m telescope of the DENIS project at the end of December 1996 on 3 consecutive nights showed a changing coma whose V magnitude was  $\geq 16$ . The line, as found in previous observations, was composed of a narrow and strong peak of FWHM  $\sim 0.1$  km s<sup>-1</sup> blue-shifted by  $\sim 0.45$  km s<sup>-1</sup>. On closer inspection, it appeared that the line profile extended towards negative radial velocities (the “skirt”). This is well seen in the average “ON” spectrum shown in Figure 2. There was no indication, within our noise level, that the line position changed with either time or activity. The CO velocity did not vary despite a nuclear activity level that was observed to change from one day to the next by a factor  $\sim 2$ . We also note that past observations of comet SW1 did not reveal any changes in the velocity of the dust (always found to be  $\sim 150$  m s<sup>-1</sup>), even when the nuclear activity level changed by a large factor. More recently, distant

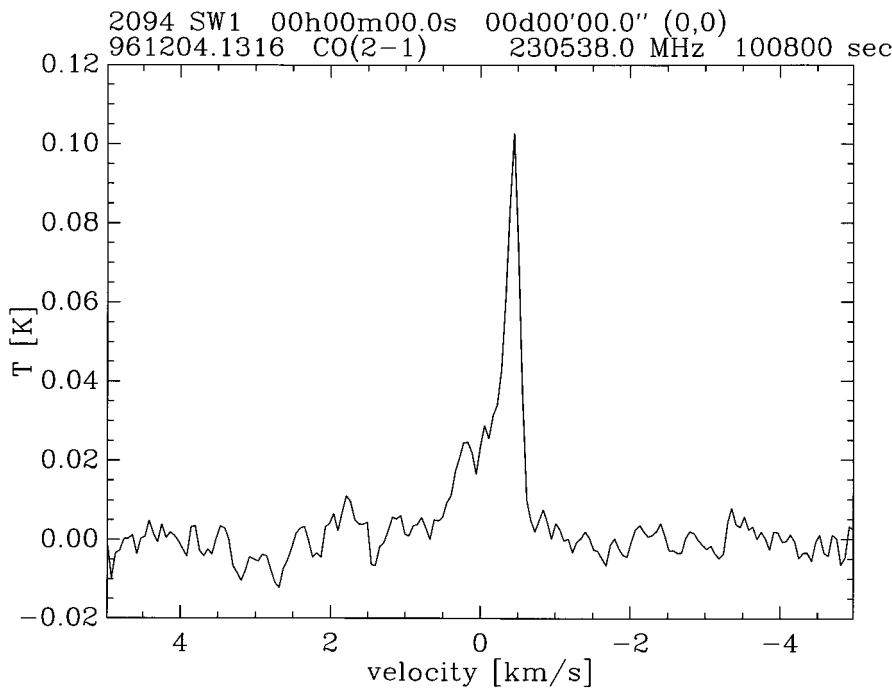


Figure 2: Average ON spectrum in December 1996. The time spent with the source in the aperture is 50,400 sec. The line peak position indicates a sunward ejection of matter at a velocity of order 500 m s<sup>-1</sup>. The width of the peak is a measure of the kinetic temperature of the gas,  $\sim 12$  K.

the zero velocity, and the observed line displacement indicates an ejection of matter on the sunward side of the nucleus. The sharpness of the main peak of the line is the result of both an under-sampling of the coma by the telescope main beam and a low kinetic temperature. The gas flows from the nucleus at a fairly high nearly monokinetic velocity, 300–500 m/s from the early measurements, and molecular collisions taking place near the nucleus do not widen the peak thus formed. Due to the long lifetime of the first CO rotational levels ( $\sim 10^6$  s) and the slow rate of pumping in the IR vibrational 1–0 lines, the rotational temperature acquired in the inner coma is conserved through most of the coma. These phenomena have typical scale lengths of the order of, or larger than,  $10^5$  km and we evaluate the effect of IR pumping to be 10% or less over the entire SEST antenna telescope main beam. The higher resolution IRAM data further showed the existence of a “skirt” extending to red-shifted velocities, a feature that was readily interpreted as proof of night-side outgassing. The present programme, conducted with the SEST

radio observations of C/Hale-Bopp, an indisputably very active comet, never revealed the presence of high gas velocities, despite the extremely large CO production measured in that comet. All this leads to the idea that the line displacement and width take values directly related to the process whereby the gases leave the nucleus but not so much to the amount of material thus produced. (Of course, near the sun, photolytic heating is a source of energy that may efficiently increase the velocity of coma species).

A study of the spatial distribution of CO molecules around the nucleus of the comet is in progress. The main spectral features, namely the peak position and width, are explained if outgassing occurs mainly on the sun-side and if its local rate is proportional to the square of the insolation and if the outflow velocity is proportional to that insolation. Since the outflow velocity is expected to vary as the surface temperature, this indicates that conduction must play a major role in controlling the surface temperature. The narrowness of the main peak is due to the low kinetic temperature of the gas. The presence of CO molecules with near-zero and negative velocities requires introducing some night-side outgassing. The assumption of LTE for the excitation holds because the rotational relaxation time constant and IR pumping rates are rather large, of the order of a few  $10^5$  sec and a few  $10^{-6}$  sec. respectively. If the telescope main beam were larger, the line shape would be quite different (the theoretical line profile for an isotropic outflow from a point source observed through a telescope main beam of large size compared to that of the coma is a rectangle of full width twice the outflow velocity), and more molecules would be observed with zero projected velocities. In our modelling, we adjust the night-side velocity to match the data and we derive that the CO flux on the night-side is  $\sim 15\%$  of that at the sub-solar point.

Complementary integrations were made at three offset positions inside the coma, at 11 arcsec anti-sunward, 11 and 22 arcsec sunward, respectively. Our ON and 22 arcsec sunward spectra are shown in Figures 2 and 3, respectively. It readily appears that the peak seen in the ON integration is also present in the offset integration, at the same velocity of

what *ad hoc* at the present time and additional observations are required to confirm or reject it. Another possible explanation is to suppose that some CO radicals are produced from grains that move very slowly on the sunward side. We are currently investigating this hypothesis, although there are difficulties associated with it too. One expects the gas to be able to entrain fairly large grains, and either those grains would evaporate rapidly to allow for the molecules to be excited in the collisional part of the coma or we have underestimated the role of the extended source of CO and that of the associated IR excitation mechanism.

The mean gaseous output of the comet is  $\sim 1$  ton per second, i.e. similar to the dust production rate derived from optical images by Fulle<sup>12</sup>. At that rate, comet SW1 can be continuously active for  $10^4$  revolutions, or a time much larger than its dynamical lifetime.

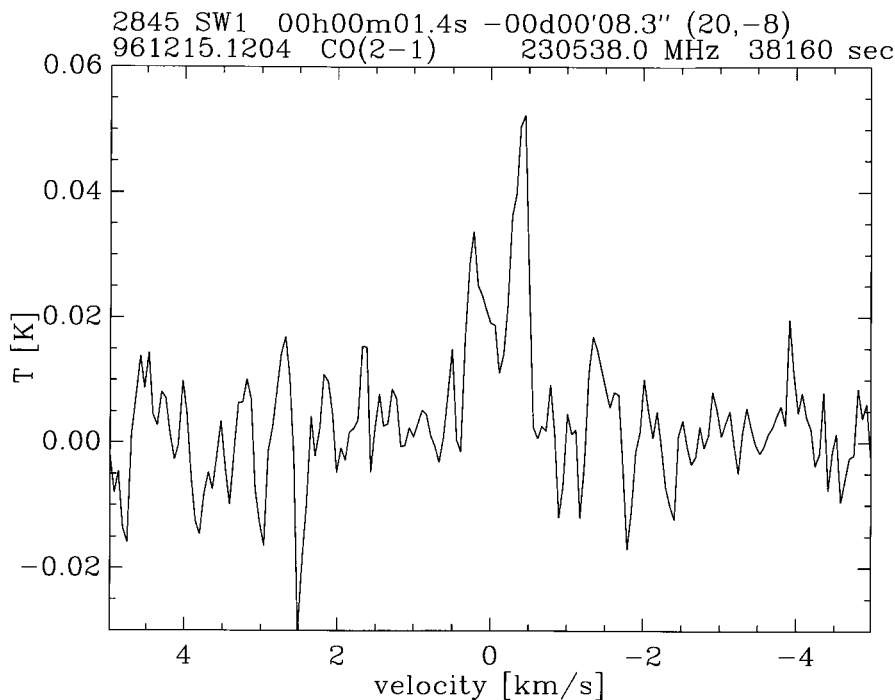


Figure 3: Mean line shape recorded in December 1996 when the telescope main beam was put 22 arcseconds away from the nucleus, sunward. The decrease in line area, within the pointing uncertainties, is barely compatible with a source of CO at the nucleus and this could be the indication of the presence of a second component produced in an extended region.

$\sim 400$  m  $s^{-1}$ . This was to be expected given the observing geometry: both the Sun and the Earth are on the same side of the nucleus and the Sun-comet-Earth angle is only 9 degrees. More surprising is the structure seen near zero velocity values. Since the telescope main beam is undersampling the CO cloud, the magnitude of this structure implies a large population of CO molecules with small radial velocities. Its presence either implies a massive injection of CO molecules in a very specific direction, near the Sun-Earth-comet plane and away from the Earth (i.e. near the terminator) or the existence of CO molecules on the sunward side that barely move. Time resolved observations of the activity of comets (e.g. comet Levy, Feldman et al.<sup>10</sup> or comet Hale-Bopp, Bockelée-Morvan et al.<sup>11</sup>) have shown that the nucleus responds rapidly to any change in the insolation pattern of the nucleus and the presence of a second component at a fixed velocity during all our observations could mean that the rotation axis of SW1 was not too far from the sunward direction. This hypothesis seems some-

## References and Notes

1. Rickman H., in *Dynamics of Comets: Their Origin and Evolution*, Carusi A. and Valsecchi G.B. Eds, Reidel, 129, 1985.
2. Fernandez J.A., *MNRAS*, **182**, 481-491, 1980.
3. Weaver H.A. et al., *Science*, **275**, 1900-1904, 1997.
4. Womack M. et al., *AJ*, in press, 1997.
5. Jewitt D., *ApJ*, **351**, 277-286, 1990.
6. Note that an  $m = 16$  object having reflecting properties similar to those of P/Halley and situated at 4 and 5 AU from the Earth and the Sun, respectively, would have a diameter of the order of  $10^2$  km.
7. Senay M.C. and Jewitt D., *Nature*, **371**, 229-231, 1994.
8. Crovisier J., Lenggries workshop on the activity of distant comets, Huebner et al. Eds., SWRI, San Antonio, TX, 1992.
9. Crovisier J. et al., *Icarus*, **115**, 213-216, 1995.
10. Feldman P. et al., *Icarus*, **95**, 65-72, 1992.
11. Bockelée-Morvan et al., *B.A.A.S.*, **29**, 3, paper 37.03, 1047, 1997.
12. Fulle M., *Nature*, **359**, 42-44, 1992.

M. Festou  
festou@astro.obs-mip.fr

# The ESO-Sculptor Faint Galaxy Survey: Large-Scale Structure and Galaxy Populations at $0.1 \lesssim z \lesssim 0.5^*$

V. DE LAPPARENT, G. GALAZ, S. ARNOUITS, CNRS, Institut d'Astrophysique de Paris  
S. BARDELLI, M. RAMELLA, Osservatorio Astronomico di Trieste

## 1. Introduction

We describe the current status of the ESO-Sculptor Survey. The observational goal has been to produce a new multi-colour photometric catalogue of galaxies in a region located near the southern galactic pole, complemented by a spectroscopic survey. The primary scientific objectives are (1) to map the spatial distribution of galaxies at  $z \approx 0.1$ – $0.5$  and (2) to provide a database for studying the variations in the spectro-photometric properties of distant galaxies as a function of redshift and local environment. The first clues towards the understanding of the matter distribution in the Universe have been obtained by mapping the distribution of its major light-emitting components, the galaxies. One of the main properties of the galaxy distribution is the presence of structures at nearly the largest scales examined (of the order of  $100 h^{-1}$  Mpc with a Hubble constant of  $H_0 = 100 h \text{ km s}^{-1}$ ) Mpc. The 3-dimensional maps provided by redshift surveys of various regions of the sky have clearly demonstrated the inhomogeneity of the galaxy distribution and have emphasised the need for systematic redshift surveys over large volumes of the universe.

The nearby galaxy distribution suggests a remarkable structure in which galaxies cluster along sharp walls which delineate vast regions with diameters between 10 and  $50 h^{-1}$  Mpc devoid of bright galaxies, in a cell-like pattern [2]. Gigantic structures such as the “Great Wall” have been detected and pose the problem of the largest scale for the inhomogeneities [3]. The general distribution has the topological properties of a “sponge”, which naturally arises from gaussian initial perturbations collapsing under gravity. The nearby redshift maps [2] have generated a renewed interest in mapping the large-scale structure of the Universe in the early 1990's. Several ambitious programmes were then initiated and provide new maps which probe the distribution out to distances of  $\sim 500 h^{-1}$  Mpc. These maps contain many sheets and voids, and confirm the sponge-like topology [4, 5], with no evidence of voids larger than  $\sim 100 h^{-1}$  Mpc [6]. It seems that these surveys have reached the scale where the galaxy distribution becomes homogene-

ous, but this requires further quantitative studies.

The maps of the galaxy distribution raise several fundamental questions of observational cosmology. Among them is the problem of the missing mass detected in increasing amounts at larger and larger scales [7]. If the limits of the nucleosynthesis predictions are to be met [8], the required dark matter for explaining the formation of large-scale structure must be for the most part non-baryonic [9]. In this picture, the galaxy formation must be biased towards the densest peaks of the matter distribution [10]. Therefore, the voids of the galaxy distribution could be filled with dark – and partly non-baryonic – matter. So far, all observational searches for baryonic matter within these voids in the form of galactic-size systems have led to only rare detections (see [11, 12] and references therein), largely insufficient for explaining a significant fraction of the missing mass. The detection of the dark matter is therefore a crucial requirement for validating the current scenario for large-scale-structure formation (the gravitational collapse of primordial fluctuations). Another challenge is to reconcile the size and amplitude of the inhomogeneities in the galaxy distribution with the high degree of isotropy of the microwave background radiation [13] (this also requires large amounts of dark matter).

Mapping the inhomogeneities in the galaxy distribution allows to obtain clues on the nature of the primordial fluctuations in the matter density field, and therefore to better understand the prevailing mechanisms in shaping the early universe. At large scales, constraints on the spectrum of primordial fluctuations can be derived directly from the maps of the 3-dimensional galaxy distribution. On smaller scales ( $\sim 1 h^{-1}$  Mpc), the non-linear effects of gravitation compli-

cate the derivation of such constraints. A study of the different galaxy populations and their environment becomes necessary for a better insight into the formation of structure on galactic size up to several  $h^{-1}$  Mpc. Constraints on the initial perturbations which led to the formation of structures on these scales may be obtained if one can eventually make the link between the mass function of the collapsing matter, the star formation history of the galaxies, and the influence of their environment. The mass function is predicted by the theoretical models and is partly constrained by the galaxy luminosity function [14]. The star formation history is tightly constrained by the observations (spectral energy distribution and magnitude number counts) [15]. One difficulty is to decouple the influence of the local environment, to which galaxies are intimately related via tidal interactions and mergers, from the large-scale segregation effects resulting from the initial conditions [16].

Detailed knowledge of both the large-scale clustering and the galaxy populations in a 3-dimensional galaxy map therefore provides invaluable information for studying the formation and evolution of structure in the universe. With the goal to address these issues, the ESO-Sculptor survey of faint galaxies (ESS, hereafter) was initiated in 1989. The programme was granted the key-programme status by ESO, which provided the unique opportunity for obtaining a new complete galaxy sample to both substantial depth and area on the sky. A large amount of observing nights on the 3.6-m and NTT was attributed and allowed to complete the observations in the fall of 1995. We describe the characteristics of the photometric and spectroscopic ESS samples in § 2 and 3 respectively, and we report the major results already obtained in § 4. In § 5 we

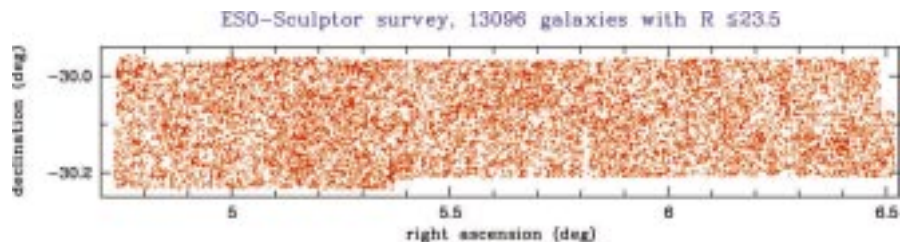


Figure 1: Distribution on the sky of the 13,096 galaxies in the ESO-Sculptor Survey (ESS) to its completeness limit of  $R = 23.5$  (in J2000 equatorial co-ordinates). The r.m.s. magnitude uncertainties are 0.04 mag, and the r.m.s. astrometric uncertainties are  $\sim 0.2$  arcsec. Even at this large depth, the galaxy distribution shows large-scale inhomogeneities which are measured by the angular 2-point correlation function [19].

\*The ESO-Sculptor Faint Galaxy Survey is one of the ESO Key Programmes. All the data have now been collected.

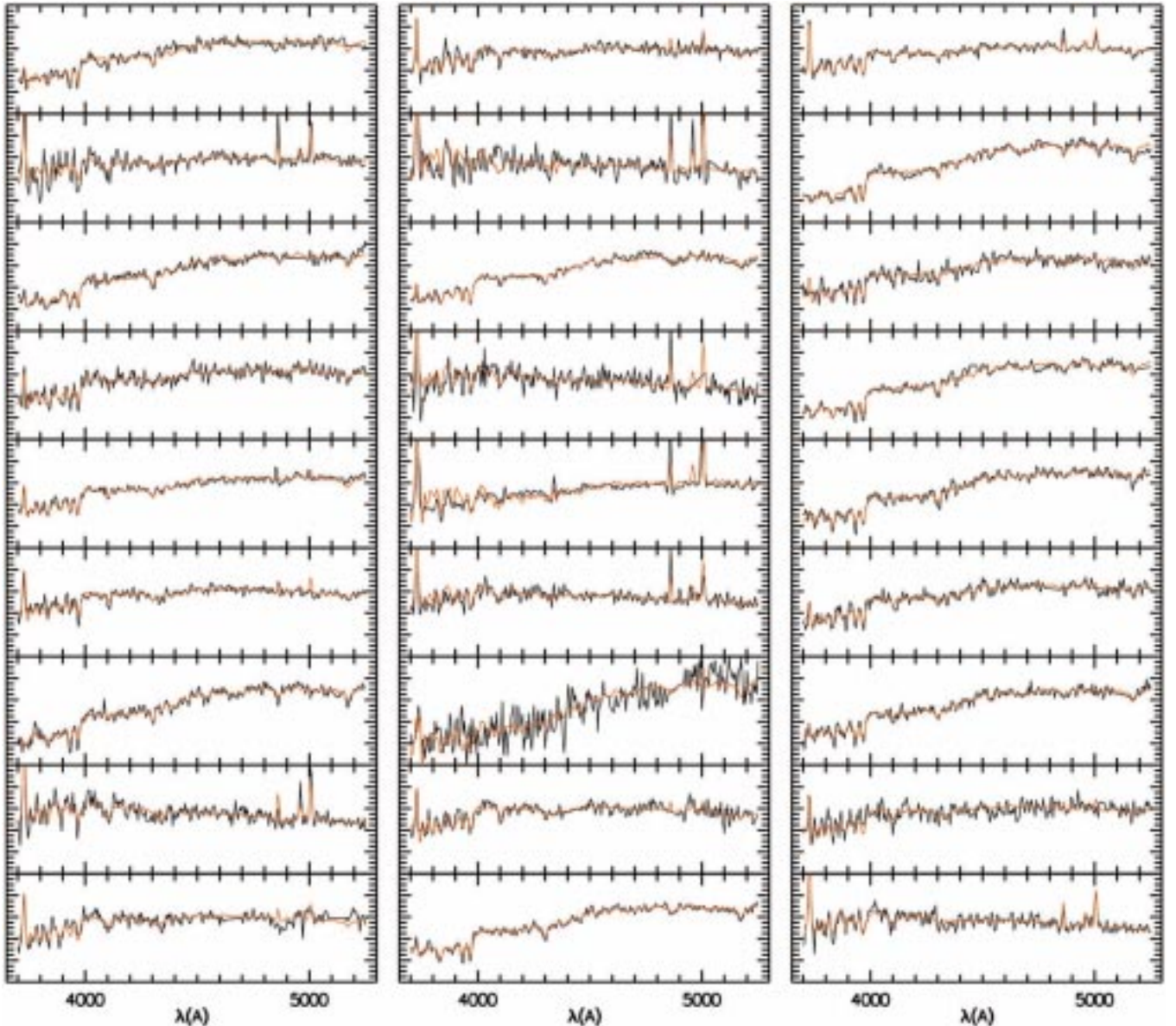


Figure 2: 27 spectra from the ESS (black curves) and their reconstructions using 3 principal components (red curves; see text for details). Note the filtering effect on the spectra with low signal-to-noise ratio, and the variable accuracy in the reconstruction of spectral lines.

comment on the results and examine the prospects for the ESS in the coming years.

## 2. The ESS Photometric Sample

The photometric data for the ESS [17] was obtained from CCD imaging of a continuous strip of  $1.53^\circ$  (R.A.)  $\times$   $0.24^\circ$  (DEC.)  $\approx 0.37$  deg<sup>2</sup> in the Sculptor constellation ( $\sim 0^h 21^m$ ,  $\sim -30^\circ$  in J2000 coordinates),  $17^\circ$  away from the Southern Galactic Pole. The typical exposure times at the NTT in the  $B$ ,  $V$ ,  $R$  filters were 25 min, 20 min, and 15 min, respectively. Whereas the  $R$  and  $V$  images have comparable depths, the  $B$  images are shallower because of the lower quantum efficiency at short wavelengths of the CCDs used. The photometry for the survey is obtained by a mosaic of  $\sim 50$  CCD frames in each filter overlapping on the edges. The galaxy catalogues are complete to  $B = 24.5$ ,  $V = 24$  and  $R =$

23.5. All objects are detected in the 3 bands up to  $R \sim 21.5$ . In the range  $22 < R < 23.5$ , the colour completeness drops to 65%. Figure 1 shows the projected distribution on the sky for the  $R$  photometric sample.

The data were reduced within MIDAS on SUN and IBM workstations. The major steps in the data reduction were: bias subtraction, flat-fielding using a “super-flat” obtained from median-filtering of the target exposures themselves, co-addition of multiple exposures, removal of cosmic events. Because the photometric data were obtained during 10 different observing runs with changing telescopes, instruments, filters and detectors, the calibration of the data required a thorough work of measurement of colour coefficients and magnitude zero-points. These were determined simultaneously with an iterative method. Listed in Table 1 are the mean zero-points and the colour coefficients for the

various instrumental set-ups used at the 3.6-m (EFOSC1) in 1989–1990, and at the NTT (EMMI) from 1990 to 1995 (see [17] for further details). These allow to convert the observed CCD magnitudes into the standard Johnson-Cousins  $BVR$  system.

To obtain a homogeneous photometry, an algorithm for comparing and adjusting the measured magnitudes in the overlaps of neighbouring CCD frames was used [17]. This technique reduces by a factor of 3 the systematic deviations in zero-point between individual CCD frames. The resulting r.m.s. internal uncertainties in our photometry are 0.04 mag in the 3 filters. The galaxy catalogue was obtained by analysing the full CCD data with SExtractor [18]. Note that the ESO-Sculptor data played a major role in testing and improving the performances of the SExtractor package for faint galaxy photometry. Because of its excellent performances, this software is

now widely used by the astronomical community. The final ESS photometric catalogue was produced after identification of the multiple detections of the same objects from different images, and determination of the adopted object parameters. This catalogue provides aperture magnitudes in the standard  $B$  (Johnson),  $V$  (Johnson) and  $R$  (Cousins) filters, astrometric positions to 0.2 arcsec, and morphological parameters for  $\sim 9500$ ,  $\sim 12,150$ , and  $\sim 13,000$  galaxies, respectively [17, 19]. As a by-product, the ESS also provides the 3-colour photometry of 2143 stars to  $B = 24.5$ . These are useful for constraining the models of galactic structure.

The ESO-Sculptor galaxy number-counts in the 3 bands, and the colour distributions are in good agreement with the results for other existing samples [17]. The faint number counts show the well-known excess over no-evolution models, in all 3 bands [20]. The faintest galaxies also exhibit a colour evolution, characterised by a blueing trend at  $R > 22$  in the  $B - V$  colour. These effects are often interpreted as an increase in the star-formation rate with look-back time [20]. The angular 2-point correlation function also shows evidence for significant evolution at  $R \approx 23$  which could be related in origin to the excess of faint galaxies in the blue number-counts [19]. Whereas the change in amplitude at fainter magnitudes was already detected in several other samples, a change in the slope is also detected thanks to the increased survey area compared to the previous studies [19]. This analysis of the angular 2-point correlation function might provide new clues on the nature and evolution of galaxies at faint magnitudes. Adjustment of the number-counts, colour distributions, and variations in the slope and amplitude of the two-point correlation function for the ESS provide useful constraints for the models of galaxy evolution, and might allow to discriminate among the different scenarios (pure luminosity evolution,

dwarf galaxy component, etc.) [20].

### 3. The ESS Spectroscopic Sample

The spectroscopic catalogue provides the flux-calibrated spectra of the complete subsample of  $\sim 700$  galaxies with  $R_c \leq 20.5$  using multi-slit spectroscopy. At this depth, there are 1.3 galaxy per sq. arcmin in the survey, and the typical multi-slit masks at the NTT contain  $\sim 30$  slits. The spectra are reduced using semi-automatic MIDAS procedures which were specifically designed for these data and which guarantee a homogeneous and systematic treatment of the numerous CCD exposures and extracted spectra. The major steps in the spectroscopic reduction are: 2-D correction for vignetting of field; cosmic events removal by comparison of multiple exposures; flat-fielding to correct for pixel-to-pixel variations, for variations in the slits transmission, and for fringes; long-slit wavelength calibration using the context LONG of MIDAS; sky subtraction with a wavelength-dependent fit of the sky flux along the slit and by interpolation at the position of the object; optimal extraction of objects by profile weighting; flux calibration using

ESO-Sculptor survey, 430 galaxies with  $R \leq 20.5$

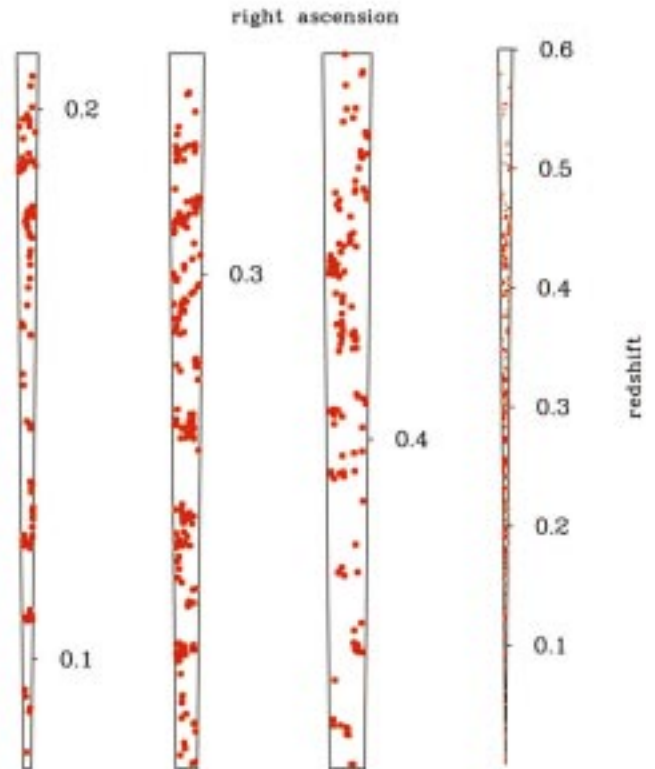


Figure 3: Distribution in R.A. versus redshift for 402 galaxies in the ESS in 3 contiguous redshift ranges (0.08–0.21, 0.21–0.34, 0.34–0.47). These maps show that the alternation of voids and walls persist at large distances, with a typical scale of  $20\text{--}60 h^{-1} \text{Mpc}$  [25]. The right-most cone shows the geometry of the full volume of the ESS (430 galaxies). In all 4 cones, the right ascension range is  $4.72\text{--}5.9^\circ$  (see Figure 1).

spectrophotometric standards; cross-correlation of the resulting spectra with galaxy templates for redshift measurement and error estimation.

The delicate extraction of spectra of extended objects with an integrated luminosity which represents only a fraction of the night sky, as it is the case for the ESS, requires optimised techniques. As a result, several of the high-level commands have been re-written within

Table 1: CCD photometric characteristics for EFOSC1 (3.6-m) and EMMI (NTT)

Instrument CCD/Period	Average zero-points			Colour coefficients <sup>(a)</sup>			
	B	V	R	$k_B[B-V]$	$k_V[B-V]$	$k_V[V-R]$	$k_R[V-R]$
EFOSC1 RCA#8/43-44 RCA#8/45-46	$23.70 \pm 0.03$ $23.41 \pm 0.01$	$24.24 \pm 0.04$ $24.06 \pm 0.03$	$24.21 \pm 0.02$ $24.03 \pm 0.02$	$0.16 \pm 0.03$ $0.16 \pm 0.03$	$0.04 \pm 0.02$ $0.04 \pm 0.00$	$0.10 \pm 0.02$ $0.10 \pm 0.02$	$0.00 \pm 0.02$ $0.00 \pm 0.02$
EMMI-R THX#18/49-50 LOR#34/52 TEK#36/54	$24.69 \pm 0.02$	$24.30 \pm 0.02$ $25.40 \pm 0.02$	$24.65 \pm 0.03$ $25.14 \pm 0.02$		$0.05 \pm 0.01$ $0.03 \pm 0.02$	$0.10 \pm 0.02$ $0.05 \pm 0.02$	$-0.10 \pm 0.01$ $-0.03 \pm 0.01$
EMMI-B TEK#31/52 TEK#31/54	$24.69 \pm 0.02$ $24.26 \pm 0.01$			$-0.21 \pm 0.02$ $-0.21 \pm 0.02$			

(a) Indicated in brackets are the colour terms by which must be multiplied the listed coefficients  $k_M$  in order to convert the observed CCD magnitudes  $M_{obs}$  into the standard Johnson-Cousins magnitudes  $M_{std}$  ( $M_{std} = M_{obs} + k_M \text{colour}$ ).

MIDAS, and allow better control of the reduction. In particular, the cross-correlation programme was specifically written for and tested on the ESS data. The essential steps are the continuum subtraction, the filtering of the spectra, and the matching of the rest-wavelength intervals of the observed spectrum and template. This matching is performed by first estimating the object redshift based on the cross-correlation with 6 templates representing the different galaxy spectral types (E, S0, Sa, Sb, Sc, Irr) and obtained by averaging several spectra from Kennicutt's sample [21]. The spectra are then cross-correlated within their common rest-wavelength intervals with a template of the bulge of M31 which provides a reliable zero-point of the redshift scale [22]. We emphasise that we do *not* use the comparison of the cross-correlation with the different galaxy types for determination of the spectral types of the ESS galaxies: this technique is subject to large errors because it is very sensitive to the noise and spurious features in the spectra. Our spectral classification method is described in § 4.2 below.

The full MIDAS routine guarantees a well-controlled and user-friendly reduction of the numerous images containing simultaneous spectra of 10 (with EFOSC1) to 30 (with EMMI) galaxies. The average slit lengths vary between  $\sim 10$  and  $\sim 30$  arcsec and the slit width is in the range 1.3–1.8 arcsec. The dispersion is 230 Å/mm. The resolution of the resulting spectra varies from 20 Å (EFOSC1) to 10 Å (EMMI) ( $\sim 110$  spectra were obtained with EFOSC1 at the 3.6-m, the rest with EMMI at the NTT). The resulting wavelength coverage is 4300–7000 Å with EFOSC1 and 3500–9000 Å with EMMI. The signal-to-noise ratio of the spectra varies in the range 4–40, with 75% in the spectra in the range 10–30. The resulting r.m.s. uncertainty errors in the redshifts are in the range 0.0002 to 0.0005 (i.e.  $\sim 60$  to 150 km s $^{-1}$ ; this corresponds to a spatial scale of 1  $h^{-1}$  Mpc, which is small compared to the size of the large-scale structures). For each galaxy, the rest-wavelength interval results from the combination of the grism dispersion, the position of the object within the multi-aperture mask, and the object redshift. The majority of the EFOSC1 spectra have rest-wavelength intervals in the range 3300–4700 Å, and the EMMI spectra in the range 3300–5700 Å. Therefore, only few emission-line galaxies have H $\alpha$  within the observed wavelength range.

Typical spectra of the ESS in the interval 3700–5350 Å are shown in Figure 2 (black lines). The prominent H (3968.5 Å) and K (3933.7 Å) lines of Ca II and the G molecular band of CH (4304.4 Å) are detected in most spectra with no emission lines. A large part of the contribution to the cross-correlation peak originates from these lines. A large fraction (48%)

of the galaxies in the sample have emission lines [23]. These are essentially [OII] 3727 Å, H $\beta$  4851 Å and [OIII] 4958.9 Å and 5006 Å. For objects with emission lines, the final redshift is obtained by the weighted mean of the cross-correlation redshift with the emission redshift derived by gaussian fits to the emission lines. Among the 277 galaxies for which the spectral classification has already been performed (see § 4.2), 4 are most likely HII galaxies (based on diagnostic diagrams using line ratios), and only one galaxy is a Seyfert 2 [23]. This is in marked disagreement with the significantly larger fraction of active galaxies found in the Canada-France Redshift Survey at  $z \leq 0.3$  [24].

A large fraction of the ESS spectra ( $\sim 3/4$ ) were observed in spectro-photometric weather conditions. Note that optimisation of the multi-slit spectroscopic observations does not allow to minimise the flux losses by adjusting the slit width and slit orientation (to correct for atmospheric refraction): the slit width is fixed and varies from 1.3 to 1.8 arcsec for the survey, and the slit/mask orientation is chosen as to globally maximise the spacings between the objects perpendicular to the dispersion direction. However, at the redshift of the ESS galaxies ( $z > 0.1$ ), the slits used contain  $> 95\%$  of the disk and bulge emission of a typical face-on spiral galaxy ( $\sim 20$  kpc in diameter). Therefore, the aperture and orien-

tation bias which affect the nearby redshift surveys as well as the intermediate distance multi-fiber surveys, are small for the ESS. Comparison of multiple spectroscopic observations for a subsample of 40 spectra shows that for those taken in spectro-photometric conditions, the total external error is of the order of 7% pixel-to-pixel. Because the only existing flux-calibrated samples of galaxies are nearby samples of several tens of spectra [21], the ESS spectra provide a unique database of galaxy spectra representative of the galaxy populations in a significant spatial volume. These spectra will be useful for constraining at low redshift the models of spectrophotometric evolution of galaxies, which is an essential step for making reliable predictions of galaxy evolution at high redshift.

## 4. Current Results

### 4.1 Large-scale structure

The ESS allows for the first time to map in detail the large-scale clustering at  $z \leq 0.5$  (nearly 10 times deeper than the nearby maps of the galaxy distribution [2]). Figure 3 shows the spatial distribution for  $\sim 400$  galaxies of the ESS in 3 portions because of the long line-of-sight (the right cone shows the full redshift range for the ESS). These maps reveal a highly structured distribution which closely resembles that seen in the

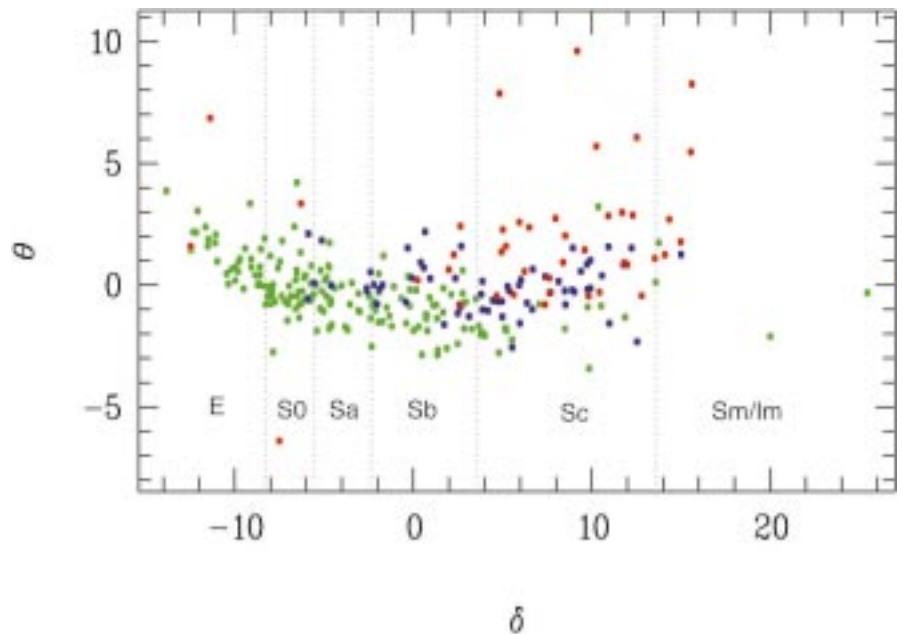


Figure 4: PCA spectral sequence for 277 ESS galaxies. The parameter  $\delta$  measures the relative contribution of the red and blue stellar components in the galaxy (PC1 et PC2 in Figure 5), and  $\theta$  measures the contribution of the emission lines (as shown in PC3 in Figure 5). Green points indicate galaxies with  $W[\text{OII}] \leq 15$  Å, blue points are galaxies with  $15 \text{ Å} \leq W[\text{OII}] \leq 30$  Å, and red points are galaxies with  $W[\text{OII}] \geq 30$  Å. The different discrete classes obtained by comparison with the Kennicutt spectra [21] are indicated by vertical dotted lines. Note the non-uniform sampling of the various types, with late-type galaxies spanning a larger range in  $\delta$ , in good agreement with the larger variations in morphological properties among the spiral galaxies. As expected, late spectral types tend to have more frequent and stronger emission lines.  $\theta$  is a good indicator of emission-line strength for late-type galaxies when used in conjunction with  $\delta$ . Some of the early-type objects also have emission lines [23].

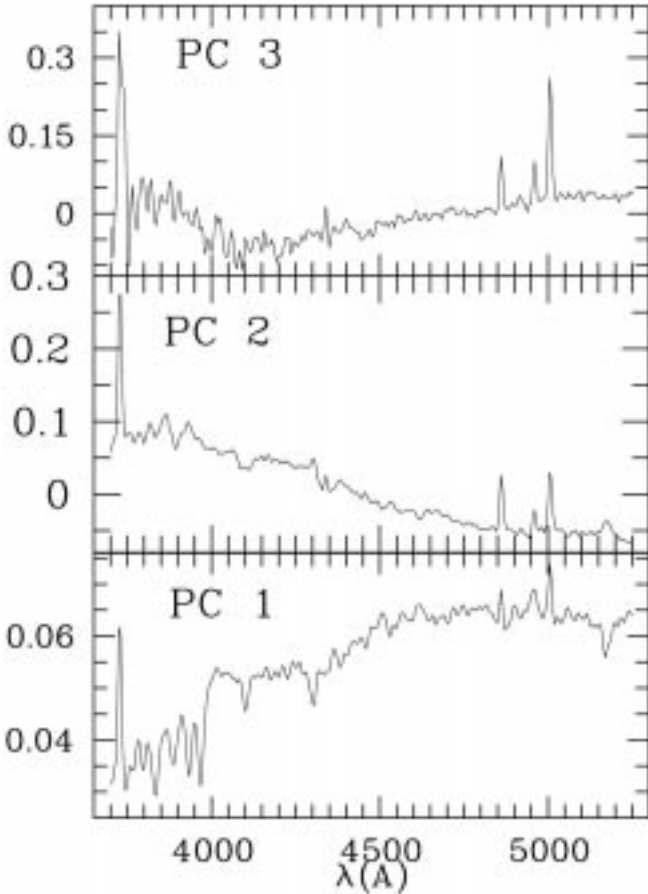


Figure 5: The first 3 principal components obtained for the ESS sample. The 1st PC is the average spectrum and resembles an Sb spectrum. The 2nd PC allows to quantify the relative contribution of the young stellar population, and the 3rd PC measures the contribution from the emission lines. 98% of the flux of the ESS spectra can be reconstructed by linear combination of these 3 PCs [23].

nearby surveys: the distribution is characterised by an alternation of sharp walls which are spatially extended across the sky, with voids with typical diameters of  $20\text{--}60 h^{-1}$  Mpc [25]. The ESS maps suggest that the cell-like galaxy clustering seen in the shallower redshift surveys extends to  $z \approx 0.5$ . Several statistical analyses of the data are in preparation (two-point correlation function, power-spectrum, genus, etc. . .) and will provide a characterisation of the large-scale clustering in the ESS for comparison with the nearby galaxy distribution. The long line-of-sight sampled by the ESS might also provide new constraints on the galaxy clustering on scales of  $\geq 100 h^{-1}$  Mpc, which are poorly sampled by the shallower surveys.

We emphasise that the large-scale structure pattern detected in the ESS is nowhere as regular as in the redshift survey of Koo et al. [26], which suggests a periodic distribution of dense structures with a separation of  $128 h^{-1}$  Mpc. This scale is well above the typical size of the voids in both the shallower surveys [2, 4, 5] and the ESS. This disagreement can be partly explained by the narrow beam size of the Koo et al. probes ( $\sim 5 h^{-1}$  Mpc at  $z \sim 0.4$ ) which makes them sensitive to small-scale clustering and might cause an overestimation of both the density contrast of the walls and the size of the voids. Moreover, the sparse distribution of the narrow probes of Koo et al. over the sky

(only a few per cent of the galaxies in the survey region have a measured redshift) makes it difficult to establish a relationship between the detected peaks and the network of sheets and voids. In contrast, the ESS was designed to sample efficiently structures similar to those found in the nearby surveys: at the median redshift of 0.3, the redshift survey probes an area of  $4 \times 15 h^{-1}$  Mpc<sup>2</sup>, sufficient for detecting most sheets with a

surface density comparable to that for the “Great Wall” [3]. Note that the ESS lies  $7^\circ$  away from the Koo et al. survey on the sky. At  $z \approx 0.3$  this corresponds to  $90 h^{-1}$  Mpc (with  $q_0 = 0.5$ ). Comparison of the 2 surveys shows no obvious correlation in the occurrence of the overdense structures along the line-of-sight, which might be difficult to reconcile with a typical clustering scale of  $128 h^{-1}$  Mpc. Further investigations along this line using simulated distributions are in progress.

#### 4.2 Spectral classification

In the ESS, galaxies have diameters  $\leq 12$  arcsec. As a result, the disk and spiral arms are poorly visible. Any attempt for a morphological classification would thus be largely approximative, and could only be limited to the presence of the main features (disk, bulge, spiral arms, signs of interaction), and restricted to the closest objects (to  $z \leq 0.2$ ; at larger distances, the diameter of the objects becomes too small  $< 9$  arcsec – for any usable classification). Even from high-resolution images, the morphological classification is dependent on the filter used for the imaging, and different filters show different stellar components with varying morphologies [27]. The Spectral Energy Distributions (SED hereafter) are a useful alternative approach for characterising the galaxy populations. The SEDs measure quantitatively the relative contributions of the underlying stellar components and constrain the gas content and average metallicity. The spectral classification thus provides a physical sequence which can be interpreted in terms of evolution of the stellar components, and allows to trace back the episodes of stellar formation. For deriving a robust classification

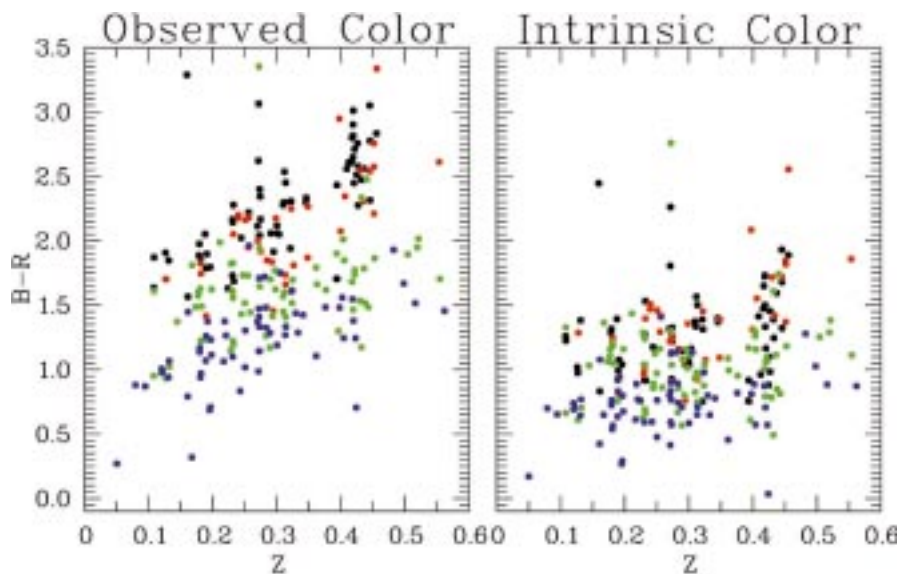


Figure 6: Observed and intrinsic  $B - R$  colours for 330 ESS galaxies as a function of redshift and spectral type ( $E/S0$  in black;  $Sa$  in red;  $Sb$  in green;  $Sc/Im$  in blue). The differences result from application of the  $K$ -corrections derived per spectral type, redshift interval, and filter band, using the spectrophotometric model PEGASE [34].

for the ESS, we have used the Principal Component Analysis (PCA hereafter) [28]. This technique is un-supervised in the sense that it does not rely on the use of a set of galaxy templates. It provides an objective study of the systematic and non-systematic trends of the sample, and has the advantage of being poorly sensitive to the noise level in each spectrum. Moreover, the resulting spectral classification is strongly correlated with the Hubble morphological type [29, 30, 23].

Application of the PCA to the ESS allows to re-write each spectrum as a linear combination of a reduced number of parameters and vectors (3 in this case), and which accounts for 98% of the total flux in each spectrum. The spectral type of the galaxies can be written in terms of 2 independent parameters  $\delta$ ,  $\theta$  which respectively measure the position of the spectra along the sequence of spectral types, and the deviation from the sequence originating from either peculiar continua and/or strong emission line. The two parameters are in addition correlated (late-types tend to have stronger emission lines). Figure 4 shows the  $\delta$ - $\theta$  sequence for 277 galaxies of the ESS sample. Figure 5 shows the first 3 principal components obtained from these data sets (PC1, PC2, and PC3). The first 2 principal components account for the red and blue stellar populations in the observed galaxies, and their relative contributions to each galaxy spectrum define its position along the PCA sequence (measured by  $\delta$ ); the 3rd component determines the emission line contribution (measured by  $\theta$ ). It was already known that the colours of galaxies can be described by a linear combination of stellar colours (namely types AV and M0III [31]). The interest of the PCA is to provide a more detailed demonstration of this effect over a large sample of galaxy spectra.

The continuous PCA spectral sequence obtained for the ESS can be binned to provide the corresponding fractions of the different Hubble morphological types (the correspondence is made by using spectra of galaxies with known morphology [21]). In this manner, we find that the ESS contains 17% of E, 9% of S0, 15% of Sa, 32% of Sb, 24% of Sc, and 3% of Sm/Im (see Fig. 4). The type fractions show no significant variations with redshift over the redshift range  $0.1 < z < 0.5$ , and are in good agreement with those found from other surveys to smaller or comparable depth (see [23, 32]). We find systematic variations in the main spectral features (equivalent width of the [OII], [OIII] and  $H_\beta$  emission lines; height of the 4000 Å break; slope of the continuum) with PCA spectral type, which illustrates the efficiency of the PCA technique for performing a physically meaningful spectral classification.

The PCA spectral classification has

many advantages over other classification methods. It first provides a *continuous* classification in a 2-parameter space, which allows quantitative analyses of the sample properties as a function of spectral type. In particular, it will allow an unprecedented measurement of the morphology-density relation [33] at large distance. The PCA also provides a convenient filtering technique: the reconstructed spectra (with 3 components) are inherently “noise-free” because the principal components are derived from a large sample of spectra. For the ESS, the reconstructed spectra have a signal-to-noise in the range 35–80 (to be compared with the range of 4–40 for the S/N of observed spectra). The ESS spectra are reconstructed from the principal components of Figure 5 as a linear combination  $\alpha_1 \mathbf{PC1} + \alpha_2 \mathbf{PC2} + \alpha_3 \mathbf{PC3}$  (with  $0.92 < \alpha_1 < 1$ ,  $-0.2 < \alpha_2 < 0.3$ ,  $-0.05 < \alpha_3 < 0.15$ ). Figure 2 shows the reconstructed spectra (in red) versus the observed spectra (in black) for 27 ESS galaxies. Reconstruction of noise-free spectra can be especially useful for comparing the ESS spectra with synthetic templates obtained from models based on stellar population synthesis [34].

The spectral classification for the ESS allows to derive accurate cosmological K-corrections for the various photometric bands, which correct for the “blue-shift” of the *observed* filter bands with respect to the *rest-frame* spectra. The crucial step is the extrapolation of the observed spectra in the rest-frame  $B$  band, which at  $z \sim 0.5$  corresponds to a  $U$  filter. For this, we use the multi-spectral model PEGASE developed at IAP by B. Rocca-Volmerange et al. [34] which provides galaxy SEDs from the UV to

the infrared. These represent a good match to the ESS spectra in the optical range 3700–5250 Å. We can then derive analytical relations between galaxy spectral type as measured by  $\delta$ , redshift and K-correction [32]. In turn, the K-corrections provide absolute magnitudes for the galaxies in the rest-frame filter bands. Figure 6 shows the observed  $B - R$  colours for the ESS spectra as a function of redshift and spectral type and the intrinsic colours after application of the K-corrections. These diagrams show that the effect of the K-corrections on the object colours is significant over the redshift range for the ESS, and is strongly correlated with spectral type. Note, however, that the large dispersion in the observed  $B - R$  colours makes any attempt to determine spectral types from colour-redshift diagrams subject to large uncertainties. This approach is often used for determination of the galaxy types.

#### 4.3 Luminosity function

In addition to the physical information which it provides, the galaxy luminosity function is indispensable for any statistical study of an apparent magnitude-limited survey. However, this function is poorly known so far due to the limited samples adequate for its measurement. The existing luminosity functions measured at  $z \leq 0.2$  from surveys with typically  $\sim 10^4$  galaxies give variables results, which are a function of the selection criteria for the samples [32]. The “local” luminosity function ( $z \sim 0.03$ ) [35] is likely to be affected by errors in the magnitude measurements in the Zwicky catalogue. Luminosity functions based on digitised plates can be biased by the non-linearity

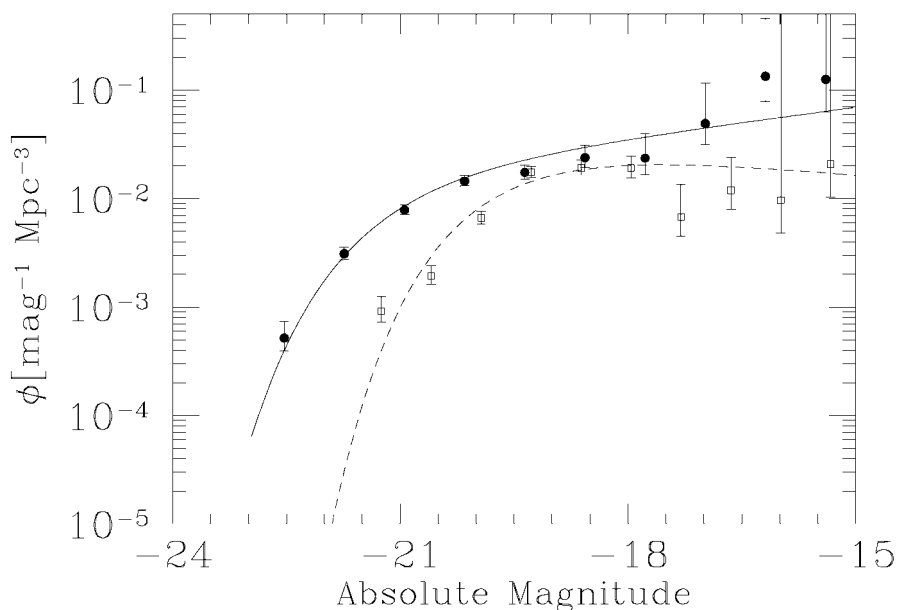


Figure 7: Luminosity functions in  $B$  (open squares) and  $R$  (filled circles) for 327 galaxies of the ESS. The best fit Schechter functions have  $M_B^* = -19.58 \pm 0.17$ ,  $\alpha_B = -0.85 \pm 0.17$ , and  $M_R^* = -21.15 \pm 0.19$ ,  $\alpha_R = -1.23 \pm 0.13$  [32].

of the photographic emulsion at bright magnitudes [36], and by incompleteness at faint magnitudes. The recent Las Campanas Redshift Survey [4] has the advantage of providing the largest CCD galaxy catalogue for measurement of the luminosity function at  $z \sim 0.2$  (see [37] and references therein). However, this spectroscopic sample is affected by selection effects such as variable sampling over the sky, and a systematic under-sampling of low-surface brightness galaxies, which might be responsible for the shallow faint-end slope.

The luminosity functions for different galaxy types show variations in their faint end slopes [37, 35]; in some cases, the variation is closely related to the presence of emission lines in the galaxy spectra [38]. In addition, deep redshift surveys suggest that the slope of the late-type luminosity function evolves significantly at  $z \geq 0.5$  [39, 40, 41]. Although the different deep surveys agree to detect an evolution in the luminosity density by a factor of nearly 2 between  $z \sim 0$  et  $z \geq 0.5$  [41, 42], the differences in the results emphasise the need for a confrontation with new catalogues. In Figure 7, we show the B and R luminosity function for 327 galaxies from the ESS sample calculated using an “inhomogeneity-independent” method (see [32] for details). The 2 luminosity functions are in good agreement with the results for the CNOC1 survey [40] using similar filters and an analogous observational set-up (multi-slit spectroscopy at the Canada-France-Hawaii telescope), and which probes the galaxy distribution to similar depth as the ESS. A more detailed study using the full ESS sample is in course.

## 5. Conclusions and Prospects

The ESS demonstrates the interest of a deep fully-sampled pencil-beam survey for probing through and identifying numerous large-scale structures along the line-of-sight. The survey confirms that the nearby properties of the large-scale clustering extend to  $z \lesssim 0.5$ , namely a cell-like structure of sharp walls alternating with voids of order of  $20\text{--}60 h^{-1}$  Mpc in diameters [25]. Measures of the power-spectrum at scales  $\geq 100 h^{-1}$  Mpc and of the topological properties of the detected structures will provide useful constraints on the nature of the primordial fluctuations which led to the observed large-scale clustering. The ESS also has the potential for uncovering very large structures exceeding the extent of the shallower surveys. Some marginal evidence for the presence of an extended under-density in the redshift range  $0.3\text{--}0.4$  is under close examination.

The ESS photometric survey is the largest CCD multi-colour survey of galaxies, and allows to confirm with tighter

error bars the previous analyses of galaxy number counts and colour distribution at  $B < 24.5$  based on smaller areas and/or fewer bands [17]. The ESS galaxy spectra provide a unique database for adjustment of the models of spectrophotometric evolution of galaxies at “low” redshift [34]. Calibration of these models on the ESS data, via the proportions of the different galaxy types and their luminosity functions will allow to obtain better predictions of galaxy evolution at  $z > 1$ . These predictions could be tested on the full photometric sample, which extends significantly deeper than the spectroscopic sample, using the 2-point angular correlation function [19]. Photometric redshifts techniques [42], which would require the acquisition of  $U$ -band photometry, would provide additional constraints, and are under consideration.

The ESS spectroscopic sample is being complemented by a similar spectroscopic survey being performed in the northern hemisphere using the CFH Telescope. The  $\sim 1700$  galaxies contained in the two samples, and their homogeneous spectral classifications and absolute magnitude determinations provided by the Principal Component Analysis [23] will provide a new measure of the luminosity function as a function of spectral class at the intermediate redshifts  $0.1 \leq z \leq 0.5$ . The difficulty to interpret the galaxy number-counts from the “Hubble Deep Field” [42] emphasises the need for a better determination of the “local” luminosity function per galaxy type. Objective detection of the galaxy groups within the ESS is also in progress and will allow a detailed study of the different galaxy populations and their relationship with the environment, as measured by the local galaxy density and the location within the large-scale structure. In particular, the morphology-density relation [33], and the existence of an analogous to the Butcher-Oemler effect [43] for field galaxies are being investigated.

The optical study of the ESS data is complemented by multi-wavelength follow-up observations: IRAC2 on the ESO-2.2-m telescope is used for obtaining  $K'$  imaging of a sub-sample of the ESS spectroscopic sample; the same region is scheduled for observations with ISO at  $10 \mu\text{m}$  and  $90 \mu\text{m}$  (in collaboration with B. Rocca-Volmerange); the full ESS region has been observed with the VLA at 6 cm and 20 cm (in collaboration with J. Roland and A. Lobanov). The optical- $K'$  colours allow to identify the stellar populations from massive stars to old giants. The  $K'$ -far-infrared colours allow to separate the different populations of grains, and indirectly allow to constrain the star-formation rate. Determination of the luminosity functions per type in the infrared, are crucial for interpreting the infrared galaxy counts. These, in contrast to the optical counts,

show no excess over no-evolution models [44]. Finally, the radio observations will allow to study the correlation between the optical and radio properties of the different galaxy populations in an optically selected sample (the opposite of the usual approach of making optical follow-up observations of a radio-selected sample).

We are considering the extension of the ESS spectroscopic sample one magnitude fainter using FORS1 at the VLT/UT1. This would provide the redshifts for another  $\sim 1000$  galaxies to  $z \lesssim 1$  for which the photometry is already available. This survey would be useful for obtaining a dense sampling of the large-scale structure at redshifts where so far only individual structures are detected, usually in association with quasars or radio galaxies. The evolution of the large-scale clustering at  $z \sim 1$  is expected to depend markedly on the cosmological parameters [45]. Any detection or absence of evolution in the cell-like pattern with redshift would provide useful constraints on the mean matter density in the Universe ( $\Omega$ ). The redshift extension of the ESS would also be useful for preparing the definition of the large area surveys which will be done more efficiently with VIRMOS.

Only one other systematic redshift survey is currently being performed at the depth of the ESS: the CNOC2 programme, with the goal to obtain redshifts for 10,000 galaxies at  $z \lesssim 0.7$ . Answering the question of the scale of homogeneity in the galaxy distribution, and hence of the underlying matter distribution will nevertheless require larger area redshift surveys than the ESS and CNOC2. In particular, the “Sloan Digital Sky Survey” (SDSS) [46] and the “2dF” project [47] to map 1 million and 250,000 galaxies respectively out to distances  $z \sim 0.2$  over large areas of the sky will both make a tremendous improvement in the statistical analysis of the galaxy distribution. The larger distances will be probed by the 2dF extension (6,000 galaxies to  $R \approx 21$ ) [47] and the DEEP survey with the Keck Telescope (15,000 galaxies with  $B \lesssim 24$ ) [48]. Note that the well-known difficulties with the flux calibration of multi-fiber spectroscopy, supplemented by the aperture bias at  $z \lesssim 0.2$  (the fibres only sample the core of the galaxies) will make any spectral classification of the SDSS and shallow 2dF survey subject to a number of biases. A unique survey for determination of the galaxy luminosity function per type will be the 5-m “Liquid-mirror telescope” which will provide SEDs with photometric quality for nearly one million galaxies to  $z \sim 1$  using a multi-narrow-band imaging technique [49]. These data will be essential for constraining the evolution of the galaxy populations and of the large-scale clustering with look-back time. It will also allow to simulate the biases in the SEDs obtained with the

multi-fibre surveys. Although the ESS is not in proportion with these large-area surveys to come in terms of survey volume, budget, and manpower, it provides an anticipated understanding of the properties of the galaxy distribution at large distances.

## Acknowledgements

We are grateful to ESO for the numerous nights of observing time allocated to this programme. We also wish to thank the staff members in La Silla who greatly contributed to the success of our observing runs. This research is partly supported by the "Programme National de Cosmologie" (previously "GdR Cosmologie") from INSU/CNRS.

## References

- [1] Oort, J.H. 1983, *Ann. Rev. of Astron. and Astroph.*, **21**, 373.
- [2] de Lapparent, V., Geller, M.J., Huchra, J.P. 1986, *Astroph. J. Lett.*, **302**, L1.
- [3] Ramella, M., Geller, M.J., & Huchra, J.P., 1992, *Astroph. J.*, **384**, 396.
- [4] Shectman, S.A., Landy, S.D., Oemler, A., Tucker, D.L., Kirshner, R.P., Lin, H., & Schechter, P.L. 1996, *Astroph. J.*, **470**, 172.
- [5] Vettolani, G., Zucca, E., Zamorani, G., Cappi, A., Merighi, R., Mignoli, M., Stirpe, G.M., MacGillivray, H., Collins, C., Balkowski, C., Cayatte, V., Maurogordato, S., Proust, D., Chincarini, G., Guzzo, L., Maccagni, D., Scaramella, R., Blanchard, A., Ramella, M. 1997, *Astron. & Astroph.*, in press.
- [6] Schuecker, P. & Ott, H.-A. 1991, *Astroph. J. Lett.*, **378**, L1 (<http://aquila.uni-muenster.de/mrsp-overview/mrsp-overview.html>).
- [7] Bahcall, N.A., Lubin, L.M., & Dorman, V. 1995, *Astroph. J. Lett.*, **447**, L81.
- [8] Dar, A. 1995, *Astroph. J.*, **449**, 553.
- [9] Blumenthal G.R., Faber, S.M., Primack, J.R., & Rees, M.J. 1984, *Nature*, **311**, 517.
- [10] Brdeen, J.M., Bond, J.R., Kaiser, N., Szalay, A.S. 1986, *Astroph. J.*, **304**, 15.
- [11] Brosch, N. 1989, *Astroph. J.*, **344**, 597.
- [12] Kuhn, B., Hopp, U., Elsaesser, H. 1997, *Astron. & Astroph.*, **318**, 405.
- [13] Bennett, C.L., Banday, A.J., Gorski, K.M., Hinshaw, G., Jackson, P., Keegstra, P., Kogut, A., Wilkinson, D.T., Wright, E.L. 1996, *Astroph. J. Lett.*, **464**, L1.
- [14] Ashman, K.M., Salucci, P., Persic, M. 1993, *M.N.R.A.S.*, **260**, 610.
- [15] Madau, P., Ferguson, H.C., Dickinson, M.E., Giavalisco, M., Steidel, C.C., Fruchter, A. 1996, *M.N.R.A.S.*, **283**, 1388.
- [16] Santiago, B.X., da Costa, L.N. 1990, *Astroph. J.*, **362**, 386.
- [17] Arnouts, S., Lapparent, V., Mathez, G., Mazure, A. & Mellier, Y., Bertin, E. & Kruszewski, A. 1997, *Astron. & Astroph. Suppl.*, **124**, 163.
- [18] Bertin, E. & Arnouts, S. 1996, *Astron. & Astroph. Suppl.*, **117**, 393.
- [19] Arnouts, S., Thèse de Doctoral, Université Paris VII, 1996.
- [20] Metcalfe, N., Shanks, T., Campos, A. & Fong, R. 1996, *Nature*, **383**, 236.
- [21] Kennicutt, R.C. 1992, *Astroph. J. Suppl.*, **79**, 255.
- [22] Bellanger, C., de Lapparent, V., Arnouts, S., Mathez, G., Mazure, A. & Mellier, Y., 1995, *Astron. & Astroph. Suppl.*, **110**, 159.
- [23] Galaz, G. & de Lapparent, V., 1997, *Astron. & Astroph.*, submitted.
- [24] Tresse, L., Rola, C., Hammer, F., Stasinska, G., Le Fèvre, O., Lilly, S.J., Cramp-ton, D. 1996, *M.N.R.A.S.*, **281**, 847.
- [25] Bellanger, C., de Lapparent, V., 1995, *Astroph. J. Lett.*, **455**, L103.
- [26] Koo, D.C., Ellman, N., Kron, R.G., Munn, J.A., Szalay, A.S., Broadhurst, T.J. & Ellis, R.S., 1993, in *Observational Cosmology*, eds. G. Chincarini et al., *ASP Conf. Ser.*, Vol. **51**, 112.
- [27] O'Connell, R.W., Marcum, P. 1996, in *HST and the High Redshift Universe (37th Hertstmonceux Conference)*, eds. N.R. Tanvir, A. Aragon-Salamanca, & J.V. Wall.
- [28] Murtagh, F. & Heck, A. 1987, *Multivariate Data Analysis*, Reidel.
- [29] Connolly, A.J., Szalay, A.S., Bershad, M.A., Kinney, A.L. & Calzetti, D. 1995, *Astron. J.*, **110**, 1071.
- [30] Sodré, L. & Cuevas, H. 1994, *Vistas in Astronomy*, **38**, 287.
- [31] Aaronson, M. 1978, *Astroph. J.*, **221**, L103.
- [32] Galaz, G., Thèse de Doctoral, Université Paris VII, 1997.
- [33] Dressier, A. 1980, *Astroph. J.*, **236**, 351.
- [34] "Base de données PEGASE", 1996, A.A.S. CD-ROM Series, Vol. **7**, ed. Leitherer et al. (<http://www.iap.fr/users/rocca/index.html>)
- [35] Marzke, R.O., Geller, M.J., Huchra, J.P. & Corwin, H.G., Jr 1994, *Astron. J.*, **108**, 437.
- [36] Bertin, E. & Dennefeld, M. 1997, 1997, *Astron. & Astroph.*, **317**, 43.
- [37] Lin, H., Kirshner, R.P., Shectman, S.A., Landy, S.D., Oemler, A., Tucker, D.L. & Schechter, P.L. 1996, *Astroph. J.*, **464**, 60.
- [38] Zucca, E., Zamorani, G., Vettolani, G., Cappi, A., Merighi, R., Mignoli, M., Stirpe, G.M., MacGillivray, H., Collins, C., Balkowski, C., Cayatte, V., Maurogordato, S., Proust, D., Chincarini, G., Guzzo, L., Maccagni, D., Scaramella, R., Blanchard, A., Ramella, M. 1997, *Astron. & Astroph.*, in press.
- [39] Heyl, J., Colless, M., Ellis, R.S. & Broadhurst, T., 1997, *M.N.R.A.S.*, in press, ([astro9610036](http://astro9610036)).
- [40] Lin, H., Yee, H.K.C., Carlberg, R.G., Ellingson, E. 1997, *Astroph. J. Lett.*, **475**, 494.
- [41] Lilly, S.J., Tresse, L., Hammer, F., Crampton, D. & Le Fèvre, O., 1995, *Astroph. J.*, **455**, 108.
- [42] Sawicki, M.J., Lin, H., Yee, H.K.C. 1997, *Astron. J.*, **113**, 1.
- [43] Butcher, H. & Oemler, A. 1978, *Astroph. J.*, **219**, 18.
- [44] Cowie, L.L., Gardner, J.P., Hu, E.M., Songaila, A., Hodapp, K.-W., Wainscoat, R.J. 1994, *Astroph. J.*, **434**, 114.
- [45] White, S.D.M. 1997, in *The Early Universe with the VLT*, ed. J. Bergeron (Springer-Verlag).
- [46] <http://www-sdss.fnal.gov:8000/>
- [47] <http://msowwww.anu.edu.au/colless/2dF/>
- [48] <http://www.ucolick.org/deep/home.html>
- [49] <http://www.astro.ubc.ca/LMT/lmt.html>

V. de Lapparent  
lapparent@iap.fr

# Massive Stars Running Through Space

L. KAPER, F. COMERÓN, J.Th. VAN LOON, A.A. ZIJLSTRA

## 1. Introduction

OB runaways are massive (OB) stars that travel through interstellar space with anomalously high velocities. The space velocity of these stars can be as high as 100 km/s, which is about ten times the average velocity of "normal" OB stars in the Milky Way. Many of them can be traced back to a nearby OB association where they seem to have originated from. But how did these massive stars obtain such a high velocity? Recent observations carried out at the European Southern Observatory have provided

compelling evidence that, at least in one case, the supernova explosion of a massive binary companion is responsible for the large space velocity gained by the remaining OB star. The observational evidence is based on the discovery of a wind bow shock around the high-mass X-ray binary Vela X-1, an X-ray pulsar with a B-supergiant companion. Here we report on new high-resolution coronagraphic observations of the bow shock obtained with ESO's *New Technology Telescope*. Furthermore, we present the first results of hydrodynamical calculations simulating the interaction between

the interstellar medium and the stellar wind of a B supergiant moving with a supersonic velocity.

According to Blaauw (1961), a "bona-fide" runaway star fulfils two criteria: (i) it has an observed high (i.e. > 30 km/s) space velocity and (ii) a "parent" OB association has been identified. It turns out that a significant fraction of the OB stars are runaways; their frequency steeply decreases as a function of spectral type: from about 20% among the O-types to 2.5% among B0-B0.5, and still lower among B1-B5 (Blaauw, 1993). Almost all runaways appear to be single;



Narrow-band  $H\alpha$  (left) and  $[O III]$  (right) images of the wind bow shock around the runaway binary HD77581 (Vela X-1) obtained with the NTT in January 1996. North-west is up and north-east to the left. The distance between the bow shock's apex and the supergiant is 0.9 arcminutes, which corresponds to 0.5 parsec at the distance of 1.8 kpc. To suppress the bright B supergiant's light ( $V = 6.9$  mag) we used a coronagraphic plate. Additionally, a scaled R-band frame was subtracted to further reduce the remaining stellar light. The  $H\alpha$  image clearly shows the 3-dimensional cone structure of the bow shock and the filamentary structure in front. Obviously, the system is moving to the north. Comparison of the  $H\alpha$  and  $[O III]$  images shows that the  $[O III]$  emission originates from a region in front of the (denser) part of the bow shock seen in  $H\alpha$ .

only in a very few cases a runaway is confirmed to be part of a binary or multiple system (Gies & Bolton, 1986). The average distance with respect to the galactic plane is much larger for confirmed runaways than for cluster and association members (Gies, 1987). Although based on small-number statistics, OB-runaways also tend to have high (projected) rotational velocities and relatively high surface helium abundances (Blaauw, 1993).

The majority of massive stars are members of an OB association or a cluster; e.g., for the O stars about 70% belong to a cluster or association (Gies, 1987); given the large fraction of O-runaways, it might well be that all O-type stars were born in associations and that the whole field population consists of runaway stars. The study of runaway stars is, therefore, intimately related to the problem of massive-star formation and evolution.

## 2. How are OB-Runaways Formed?

The two most popular scenarios for the formation of runaway stars are the binary supernova model (Blaauw, 1961) and the cluster ejection mechanism (Poveda et al., 1967). Blaauw suggest-

ed that when an OB star is bound to another OB star in a binary system, the supernova explosion of one of the stars (i.e. the initially most massive one) causes the disruption of the binary system since more than half of the total mass of the system would be lost after the supernova explosion of the primary. As a consequence, the remaining massive star escapes preserving its (relatively high) orbital velocity. The modern version of this scenario includes a phase of mass transfer inverting the original mass ratio, so that the resulting runaway star has a large probability to remain bound to the compact remnant (a neutron star or a black hole) produced by the supernova. The mass transfer from the evolved star to the future runaway star could increase its atmospheric helium abundance. Furthermore, the angular momentum associated with the accreted material would result in a higher rotation rate of the future runaway. The binary supernova model predicts that many OB runaways should have a compact companion. Searches for compact stars around OB runaways have, however, up to now not been successful (e.g. Philp et al., 1996).

An alternative explanation for the existence of OB-runaway stars is the cluster ejection model: the dynamical inter-

action in a compact cluster of stars results in the ejection of one or more of the members. From their extensive radial velocity survey of bright OB-runaway stars, Gies & Bolton (1986) concluded that the cluster ejection model has to be favoured. Apart from the lack of observational evidence for the presence of compact companions around OB runaways, the existence of 2 runaway double-lined spectroscopic binaries cannot be explained with the supernova model. Also the kinematical age of OB-runaway stars (i.e. the time needed to reach its present position with respect to the "parent" OB association) is often close to the age of the OB association itself, which would be in support of the cluster ejection model. In the following we will argue that at least in one case the supernova scenario applies.

## 3. A Wind Bow Shock Around Vela X-1

Kinematic studies of OB stars are hampered by the large distances at which these stars are usually found, making it very difficult to measure proper motions accurately (although this situation has significantly improved after the release of the *Hipparcos* data). But it turns out that many OB stars with high

space velocity create an unmistakable sign in the surrounding space. When an OB star moves supersonically through the interstellar medium (ISM), the interaction of its stellar wind with the ISM gives rise to a bow shock. Van Buren & McCray (1988) inspected the IRAS all-sky survey at the location of several OB-runaway stars and found extended arc-like structures associated with many of them. The infrared emission results from interstellar dust swept up by the bow shock and heated by the radiation field of the OB-runaway star. In a subsequent study (Van Buren et al., 1995), wind bow shocks were detected around one-third of a sample of 188 candidate OB-runaway stars. Thus, the detection of a wind bow shock can be considered as an observational confirmation of the runaway status of an OB star.

Recently, such a wind bow shock was discovered around the high-mass X-ray binary (HMXB) HD 77581 (Vela X-1), indicating a high space velocity of the system (Kaper et al., 1997). HD 77581 is the B-supergiant companion of the X-ray pulsar Vela X-1. The supergiant's strong stellar wind is partly intercepted by the orbiting neutron star resulting in the observed (pulsed) X-ray flux. Obviously, this binary system experienced a supernova explosion which resulted in the formation of Vela X-1. Due to a phase of mass transfer, the supernova remnant (in this case a neutron star) could remain bound to its massive OB-star companion when the system received a large kick velocity. The short ( $\sim 10^4$  years) HMXB phase starts when the OB-star becomes a supergiant. The observed wind bow shock not only indicates the runaway nature of Vela X-1, it also shows the direction of motion of the system. Most likely, Vela X-1 originates from the OB association Vel OB1; then, the kinematical age of the system is 2 to 3 million years, which would be consistent with the expected time interval between the supernova explosion of the primary and the subsequent evolution of the secondary into a supergiant (Van Rensbergen et al., 1996). The new *Hipparcos* measurements confirm this result: the space velocity of the system is about 50 km/s with respect to the OB association (which is less than the 90 km/s quoted in Kaper et al., 1997).

In Figure 1 we present new high-resolution images of the wind bow shock around Vela X-1 obtained with the *New Technology Telescope* at La Silla. We used the narrow-band H $\alpha$  (excluding the [N II] line) and [O III] filters, plus a coronagraphic plate to suppress the large flux produced by the  $V = 6.9$  mag (!) B supergiant. Furthermore, a properly scaled R-band image was used to remove (as far as possible) the remaining parts of the PSF and internal reflections (this does not work very well for the [O III] image due to the colour difference). The filamentary structure of the wind bow shock



These panels show the results of numerical simulations of the bow shock produced by a runaway star with the wind parameters derived for HD 77581 (Vela X-1), moving at 90 km/s in a medium with a density of one hydrogen atom  $\text{cm}^{-3}$ . Shown is the gas density. Different hypotheses about the physical behaviour of the gas are made in each case: in the middle panel, the gas is allowed to cool down by radiation and to transport energy by conduction. In the top panel, it is assumed to be isothermal, at a temperature of 8500 K. In the bottom panel, thermal conduction has been suppressed. Each panel covers an area of  $4.4 \times 2.2$  parsec. The simulations indicate that a filamentary structure of the bow shock is expected.

is present for both filters. In three dimensions the bow shock has a parabolic shape. H $\alpha$  photons produced by the far side of the bow shock appear in this image as a sharp contrast between the front and far side of the bow shock. A comparison of the H $\alpha$  and [O III] images shows that the [O III] emission originates from a region in front of the (denser) part of the bow shock seen in H $\alpha$  (use the "remnants" of the surrounding stars as a reference). To determine the spatial separation between the regions producing H $\alpha$  and [O III] emission, projection effects should be taken into account.

#### 4. Hydrodynamical Simulations

In order to interpret these observations, we performed hydrodynamical simulations of the interaction process between the stellar wind of the runaway system and the interstellar medium. The observed bow shock is only the outermost layer of a more complex structure, whose characteristics are determined by the efficiency of the different physical processes operating in the interstellar gas. Proceeding away from the star, one

finds in the first place the region of freely flowing wind. This region is bounded by a strong shock, where most of the kinetic energy of the wind is transformed into thermal energy. The hot, low-density shocked gas has a rather slow cooling rate and, while flowing downstream, it provides a cushion supporting the bow shock against the ram pressure of the ambient gas. The high temperature of the shocked stellar wind, in contact with the warm, dense gas from the ambient medium accumulated in the bow shock, produces an intense flow of energy from the hot to the warm gas by thermal conduction. The effects of this energy flow are to keep the temperature of the shocked wind at a value of a few million degrees, and to evaporate dense gas from the bow shock into the hot interior. This produces an interface of intermediate density and temperature between the shocked wind and the bow shock.

In Figure 2 a simulation is shown of the bow shock using the parameters for Vela X-1 derived by Kaper et al. (1997), arbitrarily turning off some of the relevant physical processes in the gas in order to estimate their relative impor-

tance. The frame in the middle shows the structure outlined above, with both radiative cooling and thermal conduction at work in the hot gas. The top frame shows the same results, but now assuming that the shocked wind is able to instantaneously cool down to a temperature of 8,500 K, the same as the ambient gas. The shape of the bow shock is in this case much more irregular; this is due to the chaotic motions induced by Kelvin-Helmholtz instabilities when the gases coming from the ambient medium and from the stellar wind, having very different velocities along the bow shock, get in contact. Finally, the bottom frame is the same as the middle one, but now without allowing energy transport by thermal conduction. Also in

this case, the bow shock becomes unstable, with ripples and filaments appearing all along its inner surface. The sharper jump in density from the shocked wind to the bow shock is also apparent in this case. These simulations are described in detail by Comerón & Kaper (1997, in preparation).

In conclusion, we see that the observation of a wind bow shock around Vela X-1 provides support for Blaauw's scenario for the production of runaway stars. The wind bow shock itself provides an interesting laboratory to study the hydrodynamical processes involved in the collision of stellar wind particles moving at 1% of the speed of light with the interstellar medium that "approaches" the star with a supersonic velocity.

## References

- Blaauw, A. 1961, *Bull. Astr. Inst. Neth.* **15**, 265.  
 Blaauw, A. 1993, in *ASP Conf. Series*, Volume **35**, p. 207.  
 Gies, D.R. 1987, *ApJ Supp. Ser.* **64**, 545.  
 Gies, D.R., Bolton, C.T. 1986, *ApJ Supp. Ser.* **61**, 419.  
 Kaper, L., et al. 1997, *ApJ* **475**, L37.  
 Philp, C.J., et al. 1996, *AJ* **111**, 1220.  
 Poveda, A., et al. 1967, *Bol. Obs. Ton. y Tac.* **4**, 860.  
 Van Buren, D., McCray, R. 1988, *ApJ* **329**, L93.  
 Van Buren, D., et al. 1995, *AJ* **110**, 2914.  
 Van Rensbergen, W., et al. 1996, *A&A* **305**, 825.

L. Kaper  
 lkaper@eso.org

# Oph 2320.8–1721, a Young Brown Dwarf in the $\rho$ Ophiuchi Cluster: Views from the Ground and from Space

F. COMERÓN, ESO

P. CLAES, ESA, Villafranca del Castillo, Spain

G. RIEKE, Steward Observatory, Tucson, Arizona, USA

A variety of observational techniques have provided over the last few years the first reliable identifications of brown dwarfs and extrasolar planets, detected either by direct observations or by the gravitational effects on the stars they orbit. The list of the best brown-dwarf candidates known so far includes members of multiple systems, cluster members, and free-floating objects, as well as moderately young and more evolved objects. Likewise, the list of probable extrasolar planets, although still short, already includes objects covering a fairly large range of masses, distances to the central star, and eccentricities, thus suggesting the existence of several different scenarios for their formation and orbital evolution. The combination of new observational data and theoretical developments is leading to a vigorous activity in this field (Rebolo, 1997).

The observation of brown dwarfs in their earliest evolutionary stages is an important ingredient in our understanding of the formation and the characteristics of substellar objects. These objects sample a particular region of the temperature-surface gravity diagram, already abandoned by the more evolved objects discovered so far. They are still bright and hot, emitting most of their luminosity in the near-infrared. Their presence in clusters allows the study of coeval samples with well-constrained ages, and the determination of the mass func-

tion down to substellar masses. One of the best-studied very young, nearby clusters is the one near  $\rho$  Ophiuchi, usually referred to as "the  $\rho$  Ophiuchi cluster". Its proximity to the Sun (160 pc) and its age (a few million years) places its brown dwarfs well within the reach of arrays operating in the near-infrared, where the abundant dust in which the cluster members are still embedded is much more transparent than at visible wavelengths. The dust also helps by providing a natural screen against background sources unrelated to the cluster, whose density per unit area is already reduced by the relatively large distance of the cluster to the galactic equator.

In practice, the identification of a brown dwarf in an embedded cluster is complicated by several factors. Such an identification has to be done based on the luminosity, which allows an estimate of the mass by means of theoretical models (Burrows et al., 1993, D'Antona & Mazzitelli, 1994) provided that the age of the object is known. Unfortunately, the luminosity is difficult to assess, as the foreground dust absorbs most of the energy emitted at short wavelengths, including the near-infrared where the intrinsic spectral energy distribution of the object peaks. Also, a part of the luminosity of the object can be reprocessed by a circumstellar disk or envelope, which is a common feature in very young objects. On the other hand, the rapid decrease of

the luminosity of a very low mass object with time requires a precise knowledge of the age for a reliable mass estimate. However, this is not so demanding in the case of brown dwarfs, due to the temporary stability in the luminosity output by deuterium burning in the core, which can last for a time comparable to the duration of the embedded stage. These problems were considered by Comerón et al. (1993, 1996), who were able to derive mass functions down to  $\sim 0.04 M_{\odot}$  for both  $\rho$  Ophiuchi and NGC 2024 using mostly J, H and K band photometry. Nevertheless, the masses of individual objects in each of those aggregates was rather poorly constrained, due to the difficulty of reconstructing the intrinsic spectral energy distribution from the available JHK photometry alone.

The possible substellar character of one of the most promising brown-dwarf candidates identified in  $\rho$  Ophiuchi, Oph 2320.8–1721, was already pointed out by Rieke & Rieke (1990), who tentatively assigned to it a mass of  $0.06 M_{\odot}$ . This estimate was further reduced by Comerón et al. (1993), based on the need of assuming a moderate circumstellar infrared excess to fit the available photometry. A major step in supporting the brown-dwarf nature of Oph 2320.8–1721 came from its spectrum in the  $2 \mu\text{m}$  region presented by Williams et al. (1995), whose features clearly confirmed the low photospheric temperature

(below 3000 K) inferred from the fits to the broad-band photometry. Those authors set an upper limit of  $0.05 M_{\odot}$  on the mass of this object.

Oph 2320.8–1721 was included in a list of targets prepared by us for observations with the Infrared Space Observatory (ISO). The purpose of these observations was to extend the photometry of the best brown-dwarf candidates in  $\rho$  Ophiuchi into longer wavelengths, and to probe the region where their luminosities would be dominated by circumstellar emission in case that moderate amounts of circumstellar material were present. The observations were carried out in March 1996 with ISOCAM, the imaging camera on board of ISO, in wavelengths ranging from 3.6 to  $6 \mu\text{m}$ . We could also perform observations of Oph 2320.8–1721 with the NTT in the R and I bands in April 1997, and new observations in the JHK bands with IRAC2 at the ESO-MPI 2.2-m telescope, also in April 1997. The latter were intended to check for a suspected variability of the object suggested by Williams et al. (1995), which was not confirmed.

These observations sample the spectrum of Oph 2320.8–1721 from 0.7 to  $6 \mu\text{m}$ . This extended coverage enables us to disentangle in a reliable way the reddening of the spectral energy distributions of the embedded objects caused by foreground dust from that caused by the circumstellar material. As a consequence, we can now obtain a much more solid estimate of the luminosity of this object, and therefore also of its mass. Selected images taken with the telescopes mentioned above in different bands are presented in Figure 1, where Oph 2320.8–1721 appears near the centre of the frames. The magnitude of the object ranges from 24.41 in R to 10.1 at  $6 \mu\text{m}$  (ISOCAM filter LW4). In addition, the object was detected from the ground at  $10.6 \mu\text{m}$  (Rieke & Rieke, 1990), with an approximate magnitude of 8.7.

To derive the intrinsic spectral energy distribution of Oph 2320.8–1721, we have used new theoretical pre-main-sequence evolutionary tracks (Burrows et al., 1997, in preparation), which yield essentially the same best fitting parameters as the models of Burrows et al., 1993 for this particular object. The foreground extinction is assumed to follow the wavelength dependence described by Rieke & Lebofsky (1985); although important deviations from a universal law are known to exist in star-forming regions such as  $\rho$  Ophiuchi, they are unlikely to be important in the far-red and infrared wavelengths used here (Mathis, 1990). To model the circumstellar excess, we have used a power law form characterised by a single parameter,  $n$ , as defined by Adams et al. (1987). This approximation is found to reproduce to a good degree of accuracy the models of disks around low-mass stars and circumstellar envelopes around protostars

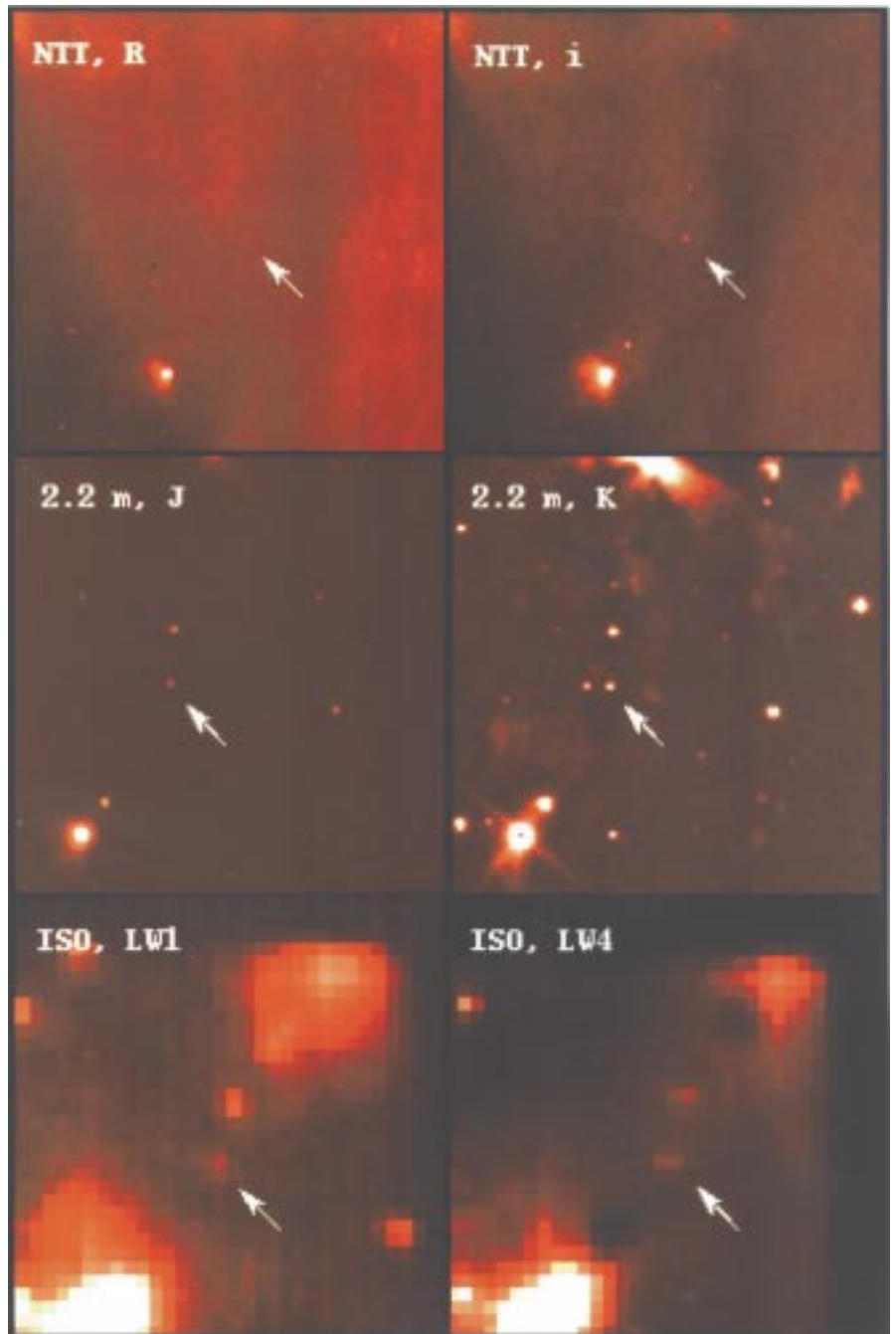


Figure 1: A mosaic of images of Oph 2320.8–1721 (pointed with an arrow) from 0.7 to  $6 \mu\text{m}$ . North is at the top and east to the left in the NTT and 2.2-m images; the ISO images are slightly rotated clockwise.

(Adams et al., 1987, Lada & Adams, 1992, Calvet et al., 1997). Finally, the photospheric fluxes at each band have been corrected for spectral features, mostly flux redistribution by wide molecular absorption bands, using approximate corrections to blackbody fluxes derived from the models of Allard & Hauschildt (1995).

Our best fit to the overall spectrum of Oph 2320.8–1721 is shown in Figure 2, and is represented by the solid line corresponding to a stellar photosphere plus a circumstellar disk reddened by foreground extinction. The dotted line represents the contribution to the luminosity from the stellar photosphere alone, reddened by the same amount of fore-

ground dust. Most of the difference between the two curves arises from light originally emitted by the central object at visible wavelengths which has been absorbed by the circumstellar disk, and then re-emitted in the mid-infrared. The rather poor fit of the measurements at R and I is probably due to the combined effect of the broad passband of those filters, the steep continuum spectral energy distribution of the object, and the complexity of the absorption features in that region. The best fit shown in Figure 2 is obtained for a luminosity of  $0.011 L_{\odot}$ , corresponding to a mass of  $0.04 M_{\odot}$ . This mass estimate does not change if the assumed age of the object is changed between 1.5 and 9 million

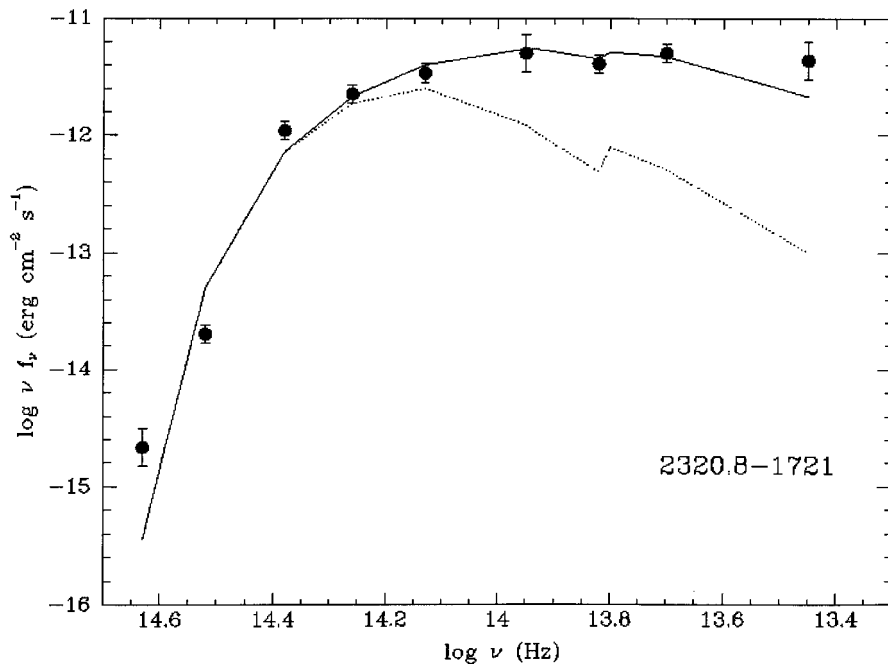


Figure 2: Best fit to the available photometry of Oph 2320.8–1721. The data points correspond from left to right to the following filters: R, I, J, H, K, L', ISOCAM LW1, ISOCAM LW4, and N. The solid line includes the contributions from the photosphere and the circumstellar excess, with the dotted line being the photospheric contribution alone. Both curves include a foreground reddening of  $A_V = 10$  mag.

years, and keeps below the stellar limit provided that the object is younger than 15 million years, which is more than the expected lifetime of an embedded cluster and several times the estimated age of the  $\rho$  Ophiuchi cluster. The circumstellar excess, characterised by a spectral index  $n = -1.6$  (where  $n = -3$  would correspond to a central source without circumstellar material and  $n > 0$  to a protostar totally embedded in its envelope) further supports the youth of Oph 2320.8–1721. The required foreground extinction to produce a good fit is  $A_V = 10$  mag, much less than the average extinction,  $A_V \sim 50$ , deduced from CO maps of the area, suggesting that Oph 2320.8–1721 is placed near the front edge of the cloud. The effective temperature of the object,  $T = 2650$  K, is

consistent with the spectral features discussed by Williams et al. (1995). On the other hand, due to the deuterium burning phase which Oph 2320.8–1721 is presumably undergoing, its age is practically unconstrained by our fits.

The long baseline in wavelength available with the new measurements, plus the insensitivity of the fit to the assumed age, make the above estimates much more robust than the ones presented in previous stages of this work. A significantly larger mass exceeding the stellar limit, implying a greater luminosity, would require a substantial increase in the amount of foreground extinction, which would be incompatible with the detection of the object in R. Moreover, this would decrease the required amount of circumstellar excess, making it inconsistent

with the rather flat shape of the  $\log(\nu f_\nu)$  curve at longer wavelengths. New, high signal-to-noise spectra of Oph 2320.8–1721 in the H and K regions obtainable in the near future with SOFI at the NTT would help to further constrain the surface temperature and gravity of this object, thus giving independent estimates of its temperature and luminosity. In the meantime, however, we can say that the identification of Oph 2320.8–1721 as a young brown dwarf is already supported by a very considerable amount of observational material.

**Acknowledgements:** We wish to thank Jason Spyromilio for making a part of his service observing time at the NTT available to us, as well as to the ESO staff providing support to the observations at the NTT and the 2.2-m telescope. Based on observations with ISO, an ESA project with instruments funded by ESA Member States (especially the PI countries: France, Germany, the Netherlands and the United Kingdom) with the participation of ISAS and NASA.

## References

- Adams, F.C., Lada, C.J., Shu, F.H., 1987, *ApJ*, **312**, 788.  
 Allard, F., Hauschildt, P.H., 1995, *ApJ*, **445**, 433.  
 Burrows, A., Hubbard, W.B., Saumon, D., Lunine, J.I., 1993, *ApJ*, **406**, 158.  
 Calvet, N., Hartmann, L., Strom, S.E., 1997, *ApJ*, **481**, 912.  
 Comerón, F., Rieke, G.H., Burrows, A., Rieke, M.J. 1993, *ApJ*, **416**, 185.  
 Comerón, F., Rieke, G.H., Rieke, M.J., 1996, *ApJ*, **473**, 294.  
 D'Antona, F., Mazzitelli, I., 1994, *ApJS*, **90**, 467.  
 Lada, C.J. Adams, F.C., 1992 *ApJ*, **393**, 278.  
 Mathis, J.S., 1990, *ARA&A*, **28**, 37.  
 Rebolo, R. (ed.), 1997, "Brown dwarfs and extrasolar planets", ASP Conf. Series, in press.  
 Rieke, G.H., Lebofsky, M.J., 1985, *ApJ*, **228**, 618.  
 Rieke, G.H., Rieke, M.J., 1990, *ApJ*, **362**, L21.  
 Williams, D.M., Comerón, F., Rieke, G.H., 1995, *ApJ*, **454**, 144.

F. Comerón  
 fcomeron@eso.org

# PMS Binaries in Southern Molecular Clouds Observed with ADONIS + COMIC

J.-L. MONIN and H. GEOFFRAY

Laboratoire d'Astrophysique – Observatoire de Grenoble, France

## 1. Introduction

The process of low-mass star formation is now well known for producing a large fraction of binary and multiple systems. This result is confirmed by many surveys (e.g. Reipurth & Zinnecker, 1993; Ghez et al., 1993; Leinert et al., 1993), showing that most, if not all, the

T Tauri stars (TTS) have companions. Therefore, the study of Pre-Main-Sequence (PMS) binary systems appears as a crucial key in understanding the process of star formation. However, due to the increasing number of multiple systems at small projected separations, the basic data do not exist for most of the individual members of these sys-

tems because of the limited angular resolution of the available instruments (cameras, spectrographs, and polarimeters), or the limited signal-to-noise ratio of the observations. For instance, some observations of PMS binaries have already been performed in Speckle at  $2.2 \mu\text{m}$  (Ghez et al., 1993), but this was mainly for a study of the binary-star fre-

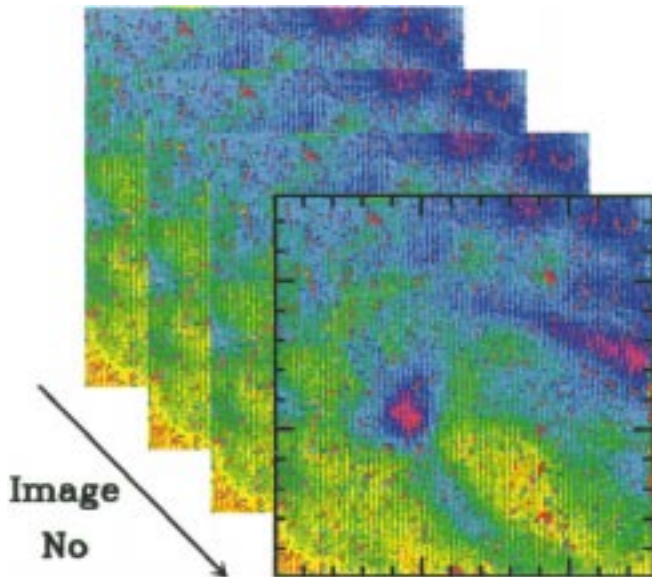


Figure 1: Example of successive ( $128 \times 128$ ) image planes recorded in the L band alternatively on the source (ON chopping mirror position) and on the nearby sky (OFF chopping mirror position). The image pattern is dominated by the sky + telescope + instrument thermal background emission, with a large amplitude of several thousands ADU over the image; no source is visible in the images at this point of the data reduction process. North is to the right, east down. Field of view is 4.6 arcsec.

quency and above all, the speckle observations do not provide such a high dynamical range as adaptive optics does.

The bulk of the emission from TTS peaks in the near-infrared. The 1–5  $\mu\text{m}$  range is therefore particularly well suited for studying the Spectral Energy Distribution of such objects and estimate their luminosity and temperature. Indeed, the recent availability of a 3–5  $\mu\text{m}$  window provided by COMIC allows to measure IR excesses at a high angular resolution, thus giving access to circumstellar accretion disks. Moreover, the separation distribution of PMS binaries peaks at  $\approx 50$  AU, corresponding to an angular separation of  $\approx 0.3''$  at the nearest star-forming region observable from ESO La Silla.

The availability of the instrument ADONIS + (SHARP / COMIC), which allows to obtain images with a resolution down to  $\approx 0.2$  arcsec or less in the range 1 to 5  $\mu\text{m}$  (J, H, K, L and M bands), with a field of view of the order of 10 arcsec, therefore provides a unique opportunity to study the binarity among PMS TTS. In practice, binaries with linear projected distance from 1500 AU down to 30 AU at the  $\rho$  Oph cloud distance, can be resolved and imaged with a high signal-to-noise ratio. At such a distance, images can be obtained of binaries with companion stars separated by less than the canonical predicted size of an accretion disk ( $\approx 100$  AU).

We have started a series of observations of PMS binary systems in order to study the precise photometry of the binary components from 1 to 5  $\mu\text{m}$  in these – often recently discovered – binary systems. From these measurements we will characterise the stellar Spectral Energy Distribution (SED) of the primary and its companion, adjust a blackbody model to estimate their luminosities and temperature, hence

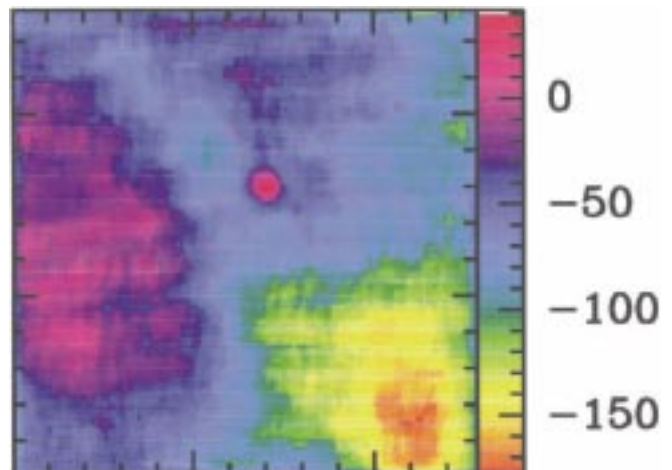
masses and ages through the use of an HR diagram. At the same time, we will study the distribution of the circumstellar and circumbinary environment of our PMS targets, in order to study how the eventual left-over material is distributed after contraction.

In this paper, we report on preliminary results of an observing run that took place in May 1996 and was the first scientific observing run with COMIC. We give some details of the observing procedure with COMIC at 3 and 5  $\mu\text{m}$ , which appears non trivial because of the high level of thermal emissivity of the close instrumental environment in these wavebands. We compute an on-the-spot estimation of the limiting magnitude that one can hopefully attain at L and M. We present some images and SEDs that have been obtained. The complete results of this work will be presented in a forthcoming paper.

## 2. Observations

We have used ADONIS + COMIC on 3 nights in 1996, May 1 and 2 and May

Figure 2: Residual close instrumental background emission pattern after ON-OFF subtraction. The sky background contribution has been subtracted and the source is now visible, approximately in the middle of the image. The amplitude of the residual background pattern is only a few tens of ADU (scale at the right of the image). Same orientation and scale as Figure 1.



5. The weather was excellent during the overall run and the experiment ran smoothly during its first scientific run, thanks to the help of the ADONIS team. From the adaptive optics point of view, TTS represent a tough challenge for the correction system since they are often dimmer than  $V = 12$  and most interesting objects are often around  $V = 14$ . We have benefited from a new quadrant of the ADONIS EBCCD and we have been able to close the loop on the primary (i.e. brighter) component of all our sources, even one with a magnitude as high as  $V = 14.9$  in the literature (V 536 Aql, Herbig and Bell, 1988). Every source was observed using the primary as a reference star. This solution appeared to work correctly for most of our objects since there was high enough a magnitude difference  $\Delta m$  between the primary and its companion. We had some correction problems only once, on a source with a  $\Delta m$  too close to zero. In such a case, the use of a numerical filter allows to reject the signal from the close companion and to restore a good correction. We also observed PSF reference stars every other observation, i.e. within 5 or 10 minutes on the average. These PSF measurements will be used as deconvolution calibrators to study the presence of dim circumstellar environment around our objects. We also observed photometric calibration stars every hour or so, so that we were able to determine the absolute photometry of both components in all the observed systems. We used approximately the same integration times in the JHK bands (during SHARP observations) and LM bands (COMIC observations). The large integration capacity of the COMIC detector allowed integration times as high as 10 seconds in L and 6 seconds in M. In fact, we always adjusted the integration time to get approximately half of the saturation level in the detector. In this configuration, the read-out noise is limited by the sky background statistical noise and the detector can be considered as perfect. The long integration times are not essential

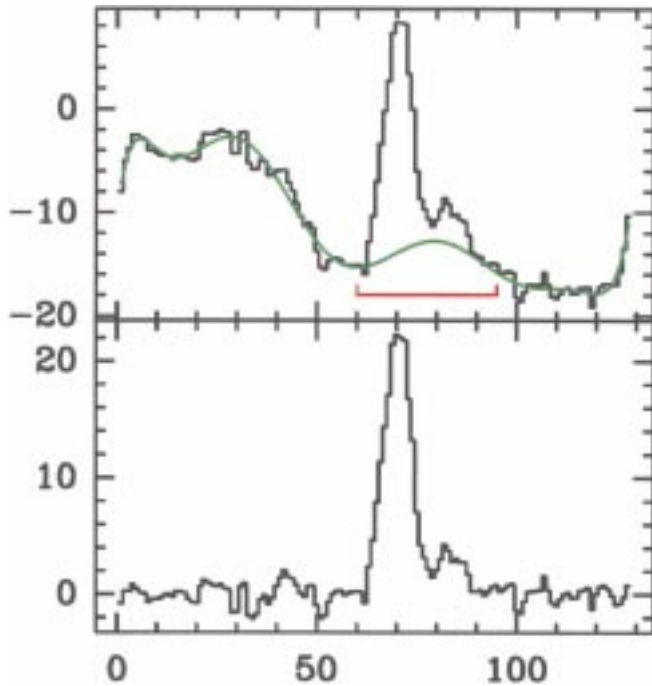


Figure 3: Line-by-line residual background fitting and subtraction. Upper panel: the source can be seen superimposed on the background. This background signal is fitted as a polynomial function (green line) outside the source position (red window). The lower panel shows the source and its companion after background subtraction. The residual rms noise is of the order of 1 ADU.

from the signal-to-noise point of view but are very convenient to increase the acquisition efficiency (integration time compared to read-out time).

### 3. Some Hints for High Background COMIC Data Reduction

The ADONIS bench allows us to use a tilt mirror to measure the sky emission on a nearby position. Three choices are possible.

(1) no chopping: then one has to move the telescope to measure the sky emission. This is slow and we didn't use it.

(2) simple chopping: the mirror moves every few images to allow the camera to measure the sky emission. This allows us to measure the sky emission if there is no sky emission gradient. The main inconvenient of this method is that the close environment thermal emission pattern changes between the ON and OFF position of the mirror. As a consequence, the sky emission is correctly suppressed in the ON-OFF operation but a new (lower) background pattern appears. This effect is well known in thermal infrared imaging and requires a beam-switching technique (nodding) to be cancelled. However, the ADONIS bench has been mainly designed for visible and "optical" near infrared (1–2.5  $\mu\text{m}$ ) observations, and beam-switching is not currently available. To cancel this effect, a solution consists of storing images of an empty part of the sky and record the close environment thermal emission pattern, in order to subtract it later from the observations. Unfortunately, we didn't measure such a pattern during our observations and we only used the simple chopping mode on all our sources. This obliged us to estimate *a posteriori* the "baseline" background in every image after pre-processing with the ECLIPSE package.

(3) double chopping: the mirror moves successively to ON, OFF1, OFF2 positions in order to measure the sky background emission on two symmetrical positions around the star. This allows us to remove any sky emission gradients, but doubles the close environment emission problem and we do not recommend to use it. Clearly, the double chopping cannot replace the beam-switching. Note that for extended sources where the close background baseline emission cannot easily be disentangled from the source emission, the use of the simple chopping appears mandatory, and it is also required to measure the thermal emission pattern of the close warm environment by performing a long enough integration (with simple chopping) on an empty part of the sky. Contrary to the sky

background emission that varies on short times, the close instrumental environment emission is relatively stable (as is its temperature) and does not need to be measured very often.

Data reduction has been performed using the ECLIPSE package developed by N. Devillard at ESO (Devillard, 1997), and some other classical data reduction packages (GRAPHIC and CLASS, two softwares developed in the Grenoble Observatory, and also IRAF).

We have removed the residual background pattern in our images by fitting a polynomial baseline on every line of the image. We found that this was more efficient than trying to fit a 2-D surface on the overall image. In any case, this implies that one defines some part of the image or line where the fit procedure must ignore the signal. We illustrate these various operations in Figures 1 to 3.

### 4. On Sky Performances

We have used our data to estimate the image quality and the limiting magnitude one can attain in the L and the M bands. Figure 4 shows the image of a binary (V 536 Aql, Monin et al., 1997), together with its associated PSF reference star, obtained with COMIC in the L band. The images have been flat-fielded and corrected for bad pixels, but no deconvolution was applied. The image correction was incomplete, but two diffraction rings can be seen on the object and on the PSF, and the correction errors are the same on both images. Photometric measurements are already possible, and deconvolution will provide a clean image of the binary. The L magnitude of the primary and the secondary are 7.1 and 8.2 respectively, and the separation of the binary is 0.5". These observations have been obtained with

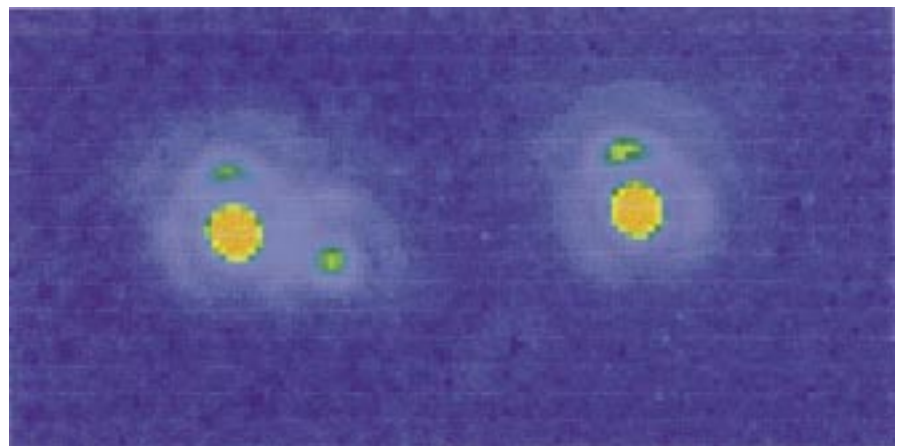


Figure 4: V536 Aql (left,  $L_A = 7.1$ ,  $L_B = 8.2$ ) image in the L band together with the PSF reference star (right). Two diffraction rings are visible both on the main component of the binary on the right part of the image and on the PSF. One diffraction ring is visible around the dim secondary of V536 Aql (the projected separation is 0.5" at P.A. 17°). North is to the right, east is down, and each image field of view is 2.2". Note that the correction errors have not been "CLEANed" and are the same on the object and on the reference star. As an example, the small bright feature in the first diffraction ring on top of each source (main component and psf, to the West) is an artifact.

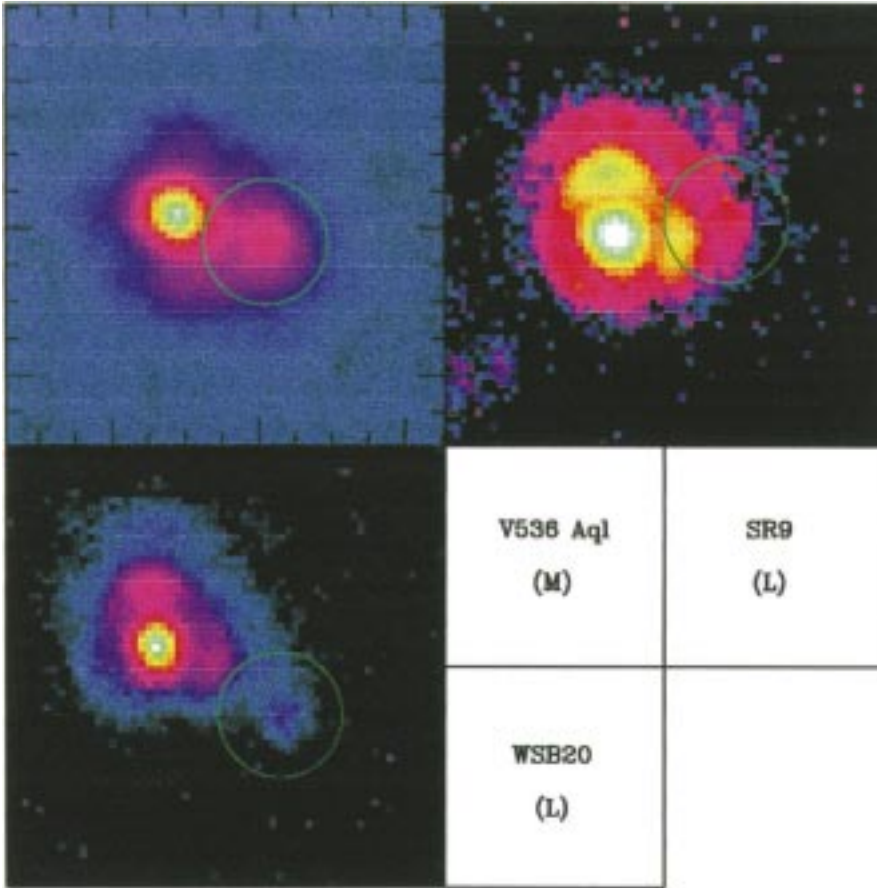


Figure 5: Sample images of close PMS binaries (V536 Aql, sep.  $0.5''$ , SR9, sep.  $0.6''$ , WSB20, sep.  $0.7''$ ). The orientation (north to the right and east down) and the image scale (field of view of  $2.2''$ ) are the same as in Figure 4. The respective name of the sources together with the corresponding IR photometric band are indicated in the figure. In every image, the circle traces the first diffraction ring around the secondary component.

an integration time per frame of 8–10 second and the total integration time is of the order of 30 s. We have estimated the limiting magnitude in the L band by comparing the background noise in the image with the amplitude of the signal on a photometric reference star.

On HR 4523 ( $L = M = 3.3$ ), we obtain  $L_{\text{lim}}(1 \text{ s}, 1 \sigma) = 11$ . Marco et al. (1997) have computed the theoretical limiting performances of the COMIC camera from laboratory measurements at (900 s,  $5 \sigma$ ). If we scale their results to (1 s,  $1 \sigma$ ), we find  $L_{\text{lim}} = 11.9$ . These two estimates have been obtained with completely different methods and appear very consistent. In the M band on the same reference star, we obtain a limiting magnitude of the order of  $M_{\text{lim}} = 8$ . This is a bit smaller than the theoretical estimates of Marco et al. (1997) and can be explained by

(1) the fact that we have observed in M with the objective optimised for JHK which gives a resolution of  $0.036''/\text{pixel}$ , similar to that of SHARP1, but which oversamples the image in M (Lacombe et al., 1997).

(2) The influence of the close background thermal emission is strong and can hardly be taken into account in a priori performance estimations.

## 5. First Binary Images and SEDs

The detailed data reduction is in progress; some preliminary results have been published by Monin et al. (1997) and the complete results, together with a deeper analysis of our data will be pub-

lished in a forthcoming paper. We present here some of the images after global reduction process, including the fit of the background baseline, but without any deconvolution applied (see Figure 5). Our background fitting procedure is equivalent to the spectral baseline fitting and removal in radio line observations, and we did use the dedicated CLASS package, developed at Grenoble Observatory and IRAM, for this purpose.

Note that we have not yet co-added all the available frames so that the signal-to-noise ratio can be upgraded in some images, especially the ones where the secondary is about ten times fainter than the primary.

We have also obtained detailed SEDs for the first time in the  $1\text{--}5 \mu\text{m}$  range for both components on close binary systems. We show one example of such results in Figure 6.

Most of our objects have never been observed separately in the visible range. Still, in some cases, when the luminosity difference is large enough between both components, we attributed the visible magnitude value to the brighter one (i.e. the primary). Then we fitted a blackbody curve and a common visual absorption to the SEDs of both components, assuming interstellar characteristics for the dependence of the absorption on wavelength (this was the case for the SR9 system shown in Figure 6). Another possibility is to fit a blackbody to the J, H and K SED points of the fainter component, and to subtract the corresponding (fitted) V, R and I flux contribution from the primary (brighter) component, before fitting this latter SED from R to H (this was the case for the WSB20 system, where both components have identical flux to within a factor of two in the range F to K).

In the case shown in Figure 6 (SR9), the components of the binary can be ap-

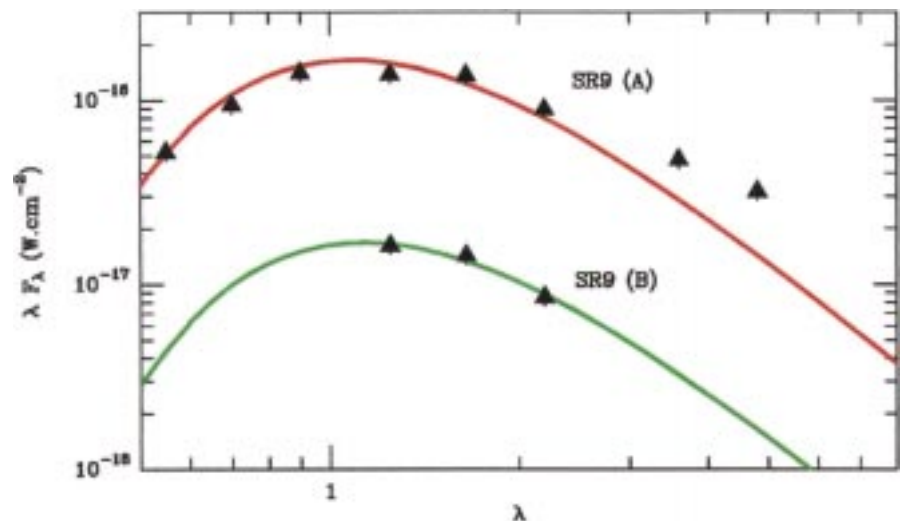


Figure 6: Spectral Energy Distribution of the components of the binary system SR9 (full triangles) together with their corresponding fitted blackbody curves (see text for details).

proximately described by the respective parameters:  $L_A = 2.5 L_\odot$ ,  $T_A = 3900$  K,  $A_V = 0.9$  (same value for both components),  $L_B = 0.25 L_\odot$ ,  $T_B = 3800$  K. There appears to be an infrared excess over a blackbody photosphere on the primary component of SR9, indicating the presence of a probable accretion disk. This example illustrates the advantage of a high angular resolution 3–5  $\mu\text{m}$  imaging detector.

## 6. Conclusion

We have used ADONIS + SHARP / COMIC to determine the SED of close PMS binaries in the full 1–5  $\mu\text{m}$  range. This new instrument available at the 3.6-m telescope at ESO is very well suited for such scientific programmes. We have used this result to determine the physical characteristics of both components of these close binaries. To take full advantage of the 3–5  $\mu\text{m}$  window on ADONIS + COMIC would require beam-switching

observations, but this is not possible with the current ADONIS setting. We therefore recommend to calibrate the close background emission by measuring it regularly (less than every hour or so) on a sky position empty of sources close to the object position. This appears particularly important if one wishes to observe extended sources like galaxies. The SED fitting procedure provides an approximate value for the visual absorption and the effective temperature. The access of the COMIC instrument to the 3–5  $\mu\text{m}$  window will allow us to detect the presence of accretion disks around close binary components and study the relation of these disks with separation. A more precise determination of the spectral type of our binary targets will await the availability of the *GraF* adaptive optics infrared spectrometer currently under tests at ESO.

**Acknowledgements.** The adaptive optics observations would not have

been possible without the constant help and support of the ESO ADONIS team, and we are happy to thank here the ESO ADONIS team for its great help and enthusiasm during the run. Hervé Geoffroy acknowledges one year of ESO studentship during which this study has been performed.

## References

- Devillard, N., 1997, *The Messenger*, **87**, 19.  
 Ghez et al. 1993, *AJ*, **106**, 200.  
 Herbig, G.H., and Bell, K.R., 1988, *Third Catalog of Emission-Line Stars of the Orion Population*, Lick Observatory Bulletin series.  
 Lacombe et al., 1997, submitted.  
 Leinert et al. 1993, *A&A*, **278**, 12.  
 Marco et al., 1997, submitted.  
 Monin et al., 1997, in *Poster Proceedings of IAU Symp. No. 182*, eds. Malbet & Castets, (1997), p. 230.  
 Reipurth & Zinnecker, 1993. *A&A*. **278**, 81.

E-mail address:

Jean-Louis.Monin.@obs.ujf-grenoble.fr

# An ESO 3.6-m/Adaptive Optics Search for Young Brown Dwarfs and Giant Planets

W. BRANDNER<sup>1</sup>, J.M. ALCALÁ<sup>2</sup>, S. FRINK<sup>3</sup>, and M. KUNKEL<sup>4</sup>

<sup>1</sup>University of Illinois at Urbana-Champaign, USA

<sup>2</sup>Osservatorio Astronomico di Capodimonte, Napoli, Italy

<sup>3</sup>Astronomisches Rechen-Institut Heidelberg, Germany

<sup>4</sup>Max-Planck-Institut für Astronomie, Heidelberg, Germany

## 1. Extrasolar Planets and the Brown Dwarf Gliese 229 B

Only two years ago, the century-old paradigm that other planetary systems would be similar to our own solar system started to change. The discovery of extrasolar giant planets and brown dwarfs by monitoring radial velocities of nearby stars revealed that giant planets are not necessarily 5 to 30 AU away from their sun but may orbit at much smaller ( $\ll 1$  AU) separations (Mayor & Queloz, 1995, Marcy & Butler, 1996).

While radial velocity surveys are most successful for discovering close companions, direct imaging allows one to probe systems with larger separations for which radial velocity methods are not sensitive. Indeed, Gl 229B, the first brown dwarf to be identified unambiguously, has a separation of 45 AU from the central star. It was discovered with an adaptive optics coronagraph at the Palomar 1.5-m telescope (Nakajima et al., 1995, Oppenheimer et al., 1995). Direct imaging of resolved objects also allows one to study their spectral features in detail.

As inferred by Allard & Hauschildt (1995) from computations of model at-

mospheres, the energy distribution of late-type dwarfs (and thus of young brown dwarfs and giant planets) is very peculiar. The molecular opacities that globally define the continuum cause the spectral energy distribution to peak around 1.1  $\mu\text{m}$  for solar metallicities, almost independently of the effective temperature.

In Figure 1 we show on top a low-resolution spectrum of Gl 229 B (Oppenheimer et al., 1995). Below, adaptive optics images obtained with ADONIS/SHARP and the circular variable filter ( $\lambda/\Delta\lambda \approx 60$ ) at three distinct wavelength bands on and off molecular absorption bands are shown. The image scale was 0.035"/pixel. Four two-minute exposures were coadded for each frame. No image deconvolution has been applied.

## 2. The Luminosity Evolution of Young Brown Dwarfs and Giant Planets

Younger brown dwarfs will have a higher luminosity, their bolometric luminosity L<sub>BD</sub> evolves with time t as  $L_{BD} \propto t^{-1.2}$  (Black, 1980, Burrows et al., 1995<sup>1</sup>) Pre-main-sequence stars exhibit a tem-

poral luminosity evolution similar to brown dwarfs. However, their luminosity  $L_{PMS}$  decreases much slower than that of brown dwarfs (e.g.  $L_{PMS} \propto t^{-0.7}$  for a pre-main-sequence star with a mass of 0.5  $M_\odot$  and an age between  $10^5$  and  $10^8$  yr, D'Antona & Mazzitelli, 1994).

Figure 2 illustrates the evolution of the luminosity ratio of a 0.02  $M_\odot$  brown dwarf and a 0.50  $M_\odot$  star. Whereas at an age of  $10^6$  yr to  $10^7$  yr the luminosity ratio is in the range of  $\approx 0.1$  to 0.03, it will be two orders of magnitude smaller at an age of  $10^9$  yr. It will become increasingly harder to detect a brown dwarf next to an "older" pre-main-sequence star or even a main-sequence star than next to a young pre-main-sequence star – always assuming that the star and the brown dwarf are coeval. Studies of the individual components of pre-main-sequence binaries revealed that most of them are indeed coeval (Hartigan et al., 1994, Brandner & Zinnecker, 1997).

Because of the smaller brightness difference, it should be much easier to de-

<sup>1</sup>Note that these calculations did not consider the fact that brown dwarfs with masses  $\geq 13 M_{\text{Jupiter}}$  will start Deuterium burning and might be considerably brighter over a short period of time.

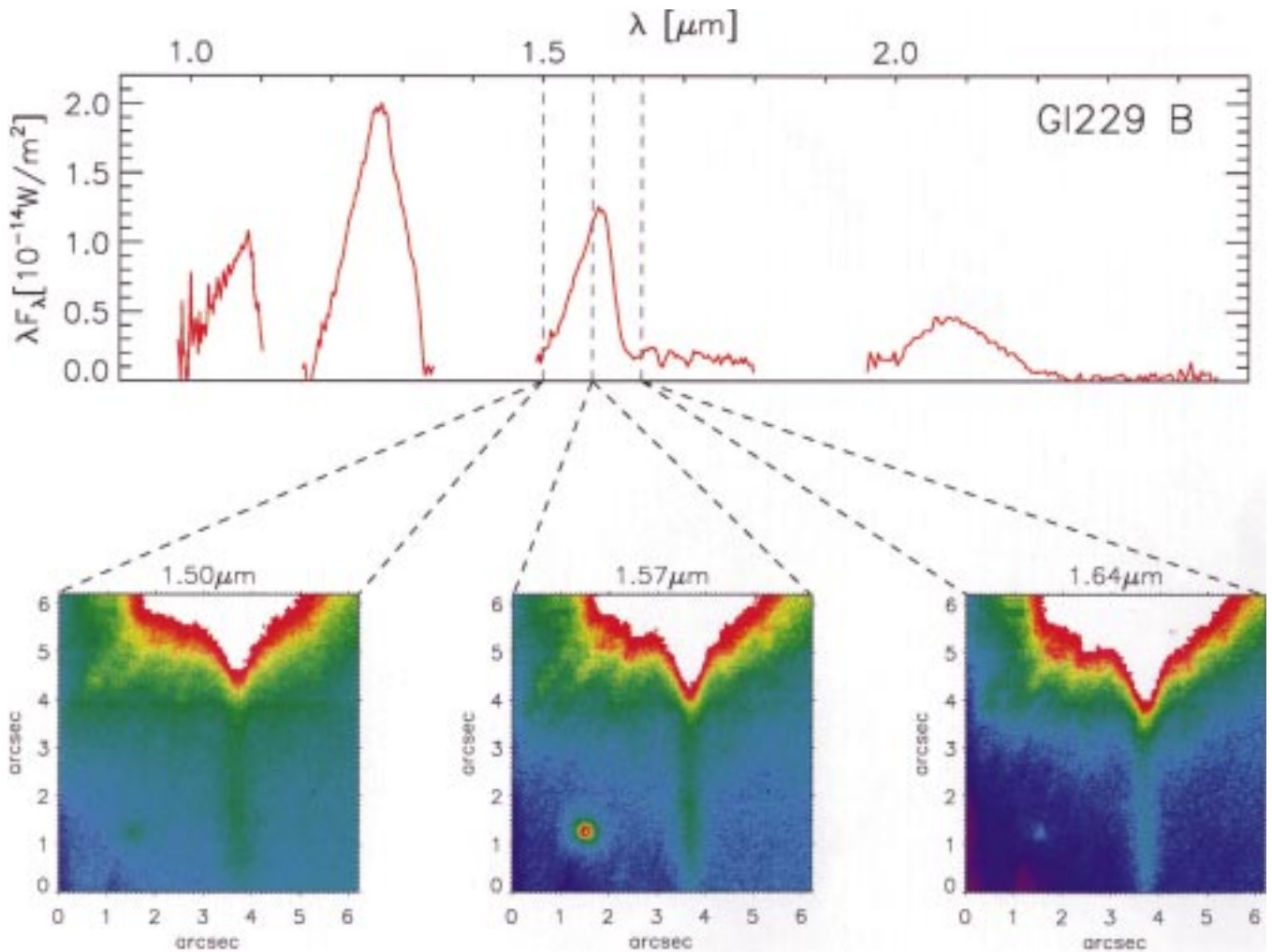


Figure 1: Top: Low-resolution spectrum of Gl 229 B (Oppenheimer et al., 1995). Bottom: Gl 229 B observed with adaptive optics (ADONIS) at the ESO 3.6-m telescope on March 24, 1997 in wavelength bands centred on molecular absorption bands and in the continuum. At the wavelength of a strong  $\text{CH}_4$  absorption band ( $1.64 \mu\text{m}$ ), Gl 229 B is about 2 mag fainter than in the nearby “continuum” ( $1.57 \mu\text{m}$ ). North is up and east is to the left.

tect and resolve young brown dwarfs and young giant planets as companions to T Tauri stars than their more evolved (older) counterparts. As explained above, observations in the near-infrared between  $1.0 \mu\text{m}$  and  $2.5 \mu\text{m}$  are suited best!

### 3. The Sample

Contrary to classical T Tauri stars, weak-line T Tauri stars no longer possess massive circumstellar disks (e.g. Beckwith et al., 1990). In weak-line T Tauri stars, the circumstellar matter was either accreted onto the central star or redistributed to form planetesimals or – via disk fragmentation – to form directly giant planets or brown dwarfs.

Based on photometric and spectroscopic studies of ROSAT sources (Alcalá et al., 1995, Kunkel et al., in preparation) we have selected an initial sample of 200 weak-line T Tauri stars in the Chamaeleon T association (cf. Fig. 3) and the Scorpius-Centaurus OB association. Proper-motion studies (e.g. Frink et al., 1997) as well as radial-velocity measurements (e.g. Covino et al., 1997) helped to select member stars of

the associations. In the course of follow-up observations visual and spectroscopic binary stars were identified

(Brandner et al., 1996, Covino et al., 1997, Köhler et al., in prep.) and excluded from our final list as the complex

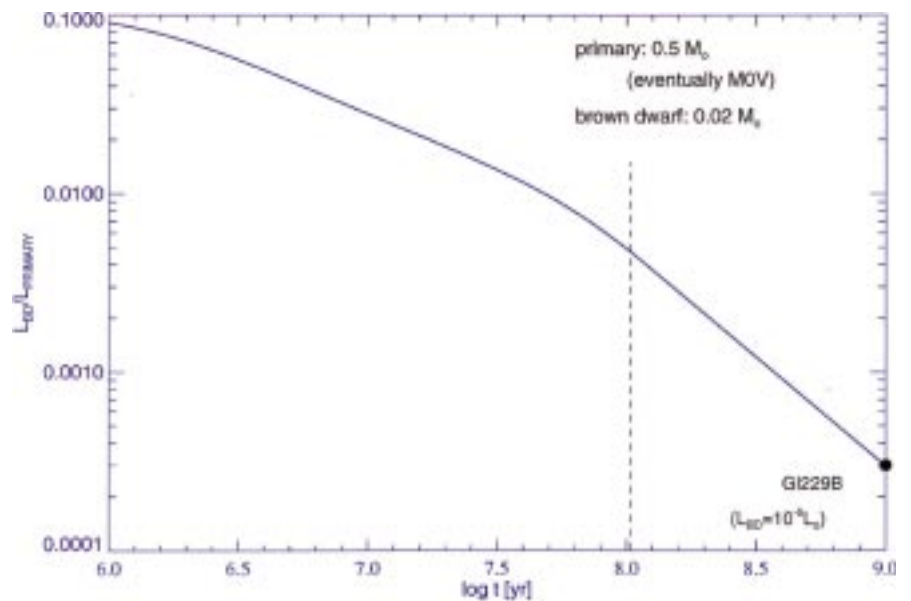


Figure 2: Temporal evolution of the luminosity ratio of a  $0.02 M_{\odot}$  brown dwarf and a  $0.50 M_{\odot}$  star (“primary”), which after  $\approx 10^8$  yr (dashed line) eventually settles on the main sequence as an M0-type star. The current location of Gl 229 B is indicated by a black dot.

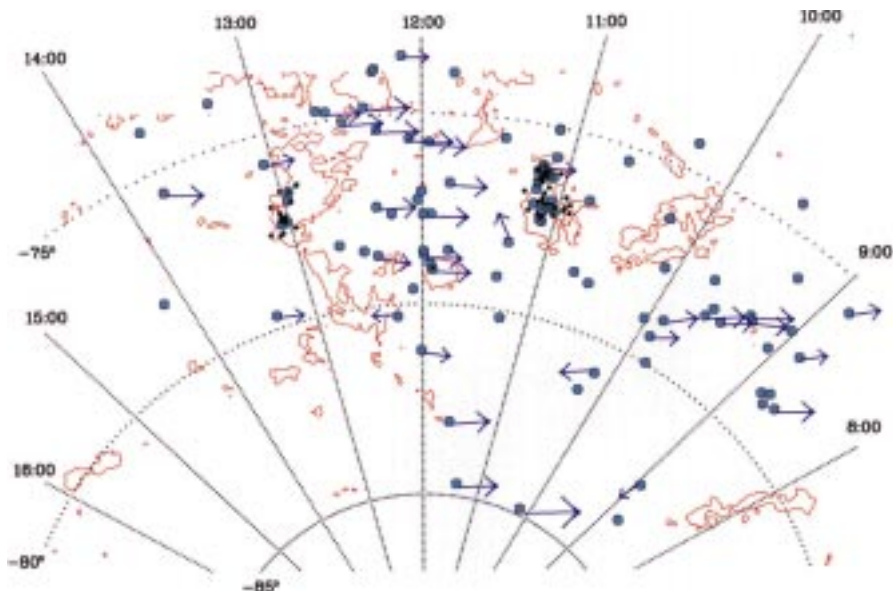


Figure 3: Spatial distribution of classical (black dots) and weak-line (turquoise dots) T Tauri stars in the Chamaeleon T association. Proper motions are indicated by blue arrows. IRAS 100  $\mu\text{m}$  contours indicate the location of the dark clouds.

dynamics and gravitational interactions in binary systems might aggravate or even completely inhibit the formation of planets (depending on physical separation of the binary components and their mass-ratio). We ended up with a final sample of about 70 presumably single weak-line T Tauri stars.

#### 4. Observations with Adaptive Optics and HST

The big questions are:

- What are the time scales for disk dissipation?

- When does planet formation take place?
- How common are young planetary systems?
- What type of environment encourages the formation of planetary systems? (T or OB associations?)

In Period 58 we started a systematic search for substellar companions to single weak-line T Tauri stars using ADONIS/SHARP at the ESO 3.6-m telescope. In total, about 50 G- and K-type weak-line T Tauri stars will be observed. In addition, from July 1997 on, 24 M-type weak-line T Tauri stars will

be surveyed for faint brown dwarf or giant planet companions with HST/NICMOS.

First results of our survey are shown in Figure 4. Follow-up observations are necessary in order to verify that the T Tauri star and its presumed companion form a common proper-motion pair. Adaptive-optics images in and out of molecular bands (cf. Figure 1, see also Rosenthal et al., 1996) will then provide a first estimate of the effective temperature of the companion

Depending on the brightness difference between the primary and the low-mass companion, our survey will be sensitive to separations down to 0.20", i.e. 30 AU (comparable to the semi-major axis of the orbit of Neptune) at a distance of 150 pc.

The new generation of 8-m- to 10-m-class telescopes in combination with adaptive optics will enable us to extend this survey to substellar companions situated even closer to their central star. From 1998 on, the Keck II telescope will be equipped with adaptive optics (diffraction limited at 2  $\mu\text{m}$ ) and thus be able to resolve separations as small as 15 AU at a distance of 150 pc. Adaptive optics at the first VLT telescope should become on-line in 2000. Diffraction limited imaging at 1  $\mu\text{m}$  would give a spatial resolution for faint companions of about 8 AU at 150 pc.

Also in 2000, the first segment of the VLTI as well as the Keck interferometer (equipped with adaptive optics) should become operational. Both interferometers will ultimately provide a resolution of 3 mas at 2  $\mu\text{m}$  (less than 1 AU at 150 pc). Thus, also the inner region of young

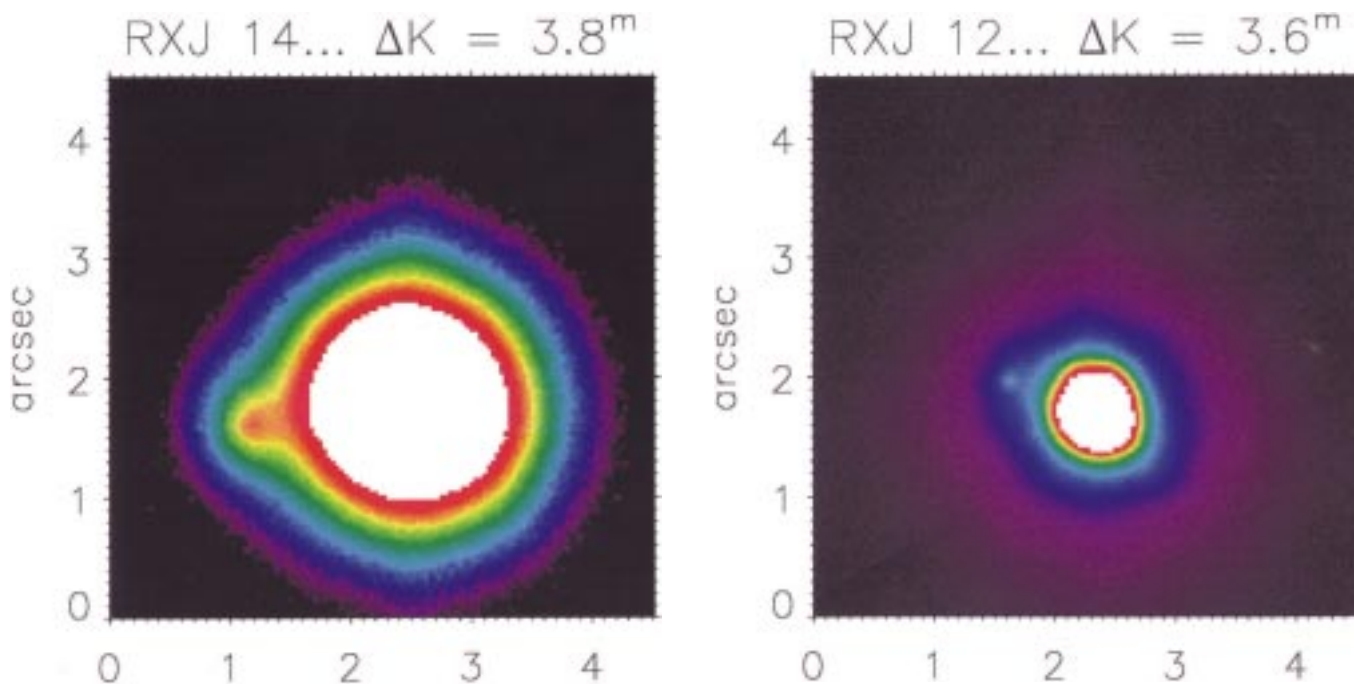


Figure 4: Candidates for substellar companions of two weak-line T Tauri stars in Chamaeleon (ADONIS/ESO 3.6-m, March 1997). Follow-up observations are necessary to discern physical companions from chance projections and to probe the physical properties of the companions. North is up and east is to the left.

planetary systems will finally become resolvable.

**Acknowledgements:** We would like to thank Drs. Eva K. Grebel and Hans Zinnecker for helpful discussions and comments.

### References

Alcalá J.M., Krautter J., Schmitt J.H.M.M. et al. 1995, *A&AS* **114**, 109.  
Allard F., Hauschildt P.H. 1995, *ApJ* **445**, 433.

Beckwith S.V.W., Sargent A.I., Chini R.S., Guesten R. 1990, *AJ* **99**, 924.  
Black D.C. 1980, *ICARUS* **43**, 293.  
Brandner W., Alcalá J.M., Kunkel M., Moneti A., Zinnecker H. 1996, *A&A* **307**, 121.  
Brandner W., Zinnecker H. 1997, *A&A* **321**, 220.  
Burrows A., Hubbard W.B., Lunine J.L. et al. 1995, *Nature* **375**, 299.  
Covino E., Alcalá J.M., Allain S., et al. 1997, *A&A*, in press.  
D'Antona F., Mazzitelli I. 1994, *ApJS*, **90**, 467.  
Frink S., Röser S., Neuhäuser R., Sterzik M.F. 1997, *A&A*, **325**, 613.

Hartigan P., Strom K.M., Strom S.E. 1994, *ApJ* **427**, 961.  
Mayor M., Queloz D. 1995, *Nature*, **378**, 355.  
Marcy G.W., Butler R.P. 1996, *ApJ* **464**, L147.  
Nakajima T., Oppenheimer B.R., Kulkarni S.R. et al. 1995, *Nature* **378**, 463.  
Oppenheimer B.R., Kulkarni S.R., Matthews K., Nakajima T. 1995, *Science* **270**, 1478.  
Rosenthal E.D., Gyrwell M.A., Ho P.T.P. 1996, *Nature* **384**, 243.

W. Brandner  
brandner@astro.uiuc.edu

## The ESO Exhibition at the IAU General Assembly in Kyoto, Japan

Like at previous IAU General Assemblies, ESO maintained an information stand with up-to-date information about the organisation and the current status

of the VLT project. A scale model of the VLT was on display and the stand also featured daily screenings of ESO videos. Located in the Event Hall next to

the e-mail terminals, the 35-square-metre ESO stand quickly evolved into "a meeting place at the meeting", serving as a venue for many informal discussions as well as a contact point for ESO staff and a steady stream of visitors wishing to learn more about ESO's activities.

Other exhibitors included the Gemini Project, the National Astronomical Observatory of Japan (including SUBARU), ROSAT, NRAO, ASP and NASDA (the Space Agency of Japan) as well as commercial exhibitors such as Carl Zeiss, Toshiba, Kluwer Academic Publishers, Cambridge University Press, etc.

C. MADSEN

*Figure 1: With the Emperor and the Empress in attendance, IAU President Prof. L. Woltjer opens the General Assembly.*

*Figure 2: ESO's stand was located between the National Observatory of Japan and NASDA, in the huge "Event Hall".*

*Figure 3: The ESO information stand – "a meeting place at the meeting".*



Figure 1



Figure 2



Figure 3

# Enhanced Resolution with Two-Channel Deconvolution Codes

L.B. LUCY, ST-ECF

## 1. Deconvolution Codes

In the last issue of *The Messenger*, Magain et al. (1997) presented impressive results obtained with a new deconvolution code. In this code, the novel idea of deconvolving with a narrower PSF (Snyder, 1990; Lucy, 1990) is combined with an astrometric capability to construct a more powerful two-channel code than that developed at the ST-ECF some years ago (Lucy, 1993, Hook & Lucy, 1993). In the ST-ECF code, the artefact of ringing around stars superposed on diffuse emission was eliminated by adding a second channel comprising only point sources, with the first channel then restricted to modelling the distributed emission. The great merit of this innovation was that the code is no longer faced with the impossible task of reconstructing  $\delta$ -functions: the investigator designates certain objects (stars, AGN) as  $\delta$ -functions and the code then proceeds to fit the data using its exact knowledge of their profiles in the image plane. Test calculations show that the amplitudes of these  $\delta$ -functions yield high-precision, unbiased magnitudes, even for crowded fields (Hook & Lucy, 1993; Magain et al., 1997).

In an *ST-ECF Newsletter* article (Hook et al., 1994), we applied our code to an image of 3C 48 and found that the nuclear regions hosting the AGN were indeed restored free from the ringing strongly evident in a Richardson-Lucy restoration. In their Figure 1, using a simulated image, Magain et al. similarly exhibit their two-channel code's superiority relative to an R-L restoration.

Note that the successful elimination of ringing derives fundamentally from giving the code, via the 2nd channel, prior information that the image contains point sources. A single-channel code that deconvolves with a narrower PSF and with an appropriately finer pixelation than the observed image – i.e., with “correct” sampling – is still prone to this artefact, though with reduced amplitude and angular scale (Lucy, 1990).

## 2. Resolution

Astronomers define the resolution of a telescope as the separation  $A_1$  of an equal component double star that is just discernible as double. With the same definition, one finds that single-channel deconvolution codes can indeed enhance resolution. However, there is a

formidable S/N barrier against achieving high resolution with such codes (Lucy, 1992). Thus, if an astronomer concludes from a restored image that a factor 2 improvement in resolution is required by the science, then he must return to the telescope and acquire an image with a factor  $2^8 = 256$  increase in signal.

For given S/N, there is a separation  $A_2$  above which deconvolution can resolve a double star, and another separation  $A_3 < A_2$  below which the image does not differ significantly from that of a single star. For intermediate separations, the slightly elongated image can be *decomposed* into two stars with a 2-channel code by suitably initiating the 2nd channel with two  $\delta$ -functions. But one is then making the *hypothesis* or introducing *prior information* that the object is double. In contrast, when a double star is resolved at the telescope or with single-channel deconvolution, no hypothesis or prior information is required.

Having decomposed an elongated stellar image into two  $\delta$ -functions, we can construct a “restored” image by convolving with a PSF of our choice. For example, we could choose the Airy function with 1st zero at 0.014” and claim the imaging capability of a perfect 10-m space telescope – and the diffraction rings would be proof! In reality, of course, the space telescope, by revealing additional stars or extended emission, might well disprove the hypothesis underpinning the decomposition.

## 3. Compact Star Clusters

The degenerate case of a compact cluster is a close double star. For this case, numerical experiments at the ST-ECF indicate that, if the only limitation is photon statistics, decomposition into components is achievable with precision and without bias, even for sub-pixel separations.

Accordingly, the decomposition of ground-based images of compact clusters with a 2-channel code is potentially a powerful technique, even without an HST image as a guide as earlier envisaged (Lucy, 1993). Nevertheless, such decompositions are not unique, since any star can be replaced by two fainter ones with negligible separation. In this circumstance, we of course seek the simplest solution consistent with the data. However, if the decomposition is made interactively and sequentially and results in several tens of stars, one may

suspect that independent workers will not find the same “simplest” solution. Clearly, procedures need to be formalised and preferably automated.

## 4. HST Proposals

When evaluating proposals for HST time, the TAC Review Panels are instructed to ask themselves whether the project can be done from the ground and to reject proposals when the answer is yes. As they stand, the strong claims by Magain et al. will therefore impact negatively on future proposals to use HST to resolve star fields in nearby galaxies. Accordingly, astronomers interested in such studies need to test whether what is possible in principle on the basis of photon statistics is in fact achievable in practice. There must be many fields that could be decomposed into stars with the Liège code and then compared to “ground truth” in the form of an image from the HST archive. Such tests should be carried out and evaluated by independent users.

The above concern does not arise for HST proposals to resolve structure in nebulae and galaxies. For such objects, we lack a physical model – the equivalent of the  $\delta$ -functions for stars – and so ground-based images cannot be decomposed in the same way. We are therefore then left with the modest resolution enhancement achievable with a single-channel code, and this is not seriously competitive with post-COSTAR HST images.

## References

- Lucy, L.B. 1990, in *The Restoration of HST Images and Spectra*, eds. R.L. White & R.J. Allen, p. 80.
- Lucy, L.B. 1992, *Astron. J.* **104**, 1260.
- Lucy, L.B. 1993, in *The Restoration of HST Images and Spectra – II*, eds. R.J. Hanisch & R.L. White, p. 79.
- Hook, R.N., & Lucy, L.B. 1993, in *The Restoration of HST Images and Spectra – II*, eds. R.J. Hanisch & R.L. White, p. 86.
- Hook, R.N., Lucy, L.B., Stockton, A., & Ridgway, S. 1994, *ST-ECF Newsletter*, No. **21**, p. 16.
- Magain, P., Courbin, F., & Sohy, S. 1997, *The Messenger*, No. **88**, p. 28.
- Snyder, D.L., 1990, in *The Restoration of HST Images and Spectra*, eds. R.L. White & R.J. Allen, p.56.

L. Lucy  
llucy@eso.org

# ANNOUNCEMENTS

## VACANCY NOTICE

### Staff Astronomers on La Silla

Two staff astronomer positions at the La Silla Observatory are available starting in 1997 to integrate the teams responsible for the operation of the New Technology Telescope (NTT) and the medium-size telescopes (MPI 2.2-m, ESO 1.5-m, Danish 1.5-m, and Dutch 0.9-m). The telescope teams are multidisciplinary teams of 10–15 persons including astronomers, technicians, engineers, and night assistants. They are fully responsible for operations and are supported in the specialised technical areas by technicians and engineers from the so-called support teams (Optics, Detectors, IR, Mechanics, Electronics, and Software). There are 4 telescope teams in total. The scientific staff of each team consists of 2 staff astronomers and 2–4 post-doctoral fellows. Staff astronomers and fellows share the responsibilities of instrument support, acting as instrument scientists in charge of direct support of visiting astronomers at the telescope, documentation, upgrades, calibration plans and on-line data reduction facilities.

La Silla staff astronomers are based at the ESO centre in Santiago, and are required to spend at least 105 nights per year at La Silla. In addition to providing full services to support scientific research (library, computers, seminars, etc.), the ESO centre in Vitacura maintains a graduate student programme which provides funds for students of European universities to spend up to 2 years in Chile working towards their Ph.D. theses, in collaboration with astronomers from the ESO staff.

One of the staff astronomers acts, on a rotating basis, as Team Leader and as such assumes the task of providing supervision and motivation to all members of the team. Team Leaders are responsible for administering the Team's budget and monitoring the performance of the team members. Team Leaders report to the Observatory Director and are members of the Observatory Management Team. They receive managerial and administrative support from the Observatory Management for budgeting and personnel issues.

A Ph.D. in astronomy or equivalent degree and several years of post-doctoral experience in the areas of high dispersion optical spectroscopy, infrared imaging and/or spectroscopy, faint object photometry/spectroscopy, or adaptive optics is required. Staff astronomers must be able to provide sound scientific judgements on the many technical issues facing a modern observatory, and ESO therefore requires, and strongly supports and encourages staff astronomers to carry out dynamic and independent research programmes, using La Silla telescopes as well as facilities at other observatories. Active publication in leading journals is considered essential. Staff astronomers use up to 50 % of their time on research and are supported with excellent facilities and generous travel grants to attend conferences, work with collaborators and visit other observatories. Proven capability of working (or leading) in multidisciplinary teams will be an advantage.

Staff Astronomer contracts are for an initial period of 3 years, which may be extended up to another three years, with the possibility of an indefinite contract offer after the fifth contractual year.

Applications and four letters of recommendation should be submitted to ESO Personnel Services, Garching, by November 28, 1997.

## ESO Astrophysics Symposia Proceedings

The proceedings of the following ESO Astrophysics Symposia are available from Springer-Verlag:

### Newly published:

- "Science with the VLT Interferometer" (Ed. F. Paresce)

### Also available:

- "The Early Universe with the VLT" (Ed. J. Bergeron)
- "Science with Large Millimetre Arrays" (Ed. P.A. Shaver)
- "The Role of Dust in the Formation of Stars" (Ed. H.U. Käufl and R. Siebenmorgen)
- "Spiral Galaxies in the Near-IR" (Ed. D. Minniti and H.-W. Rix)
- "Quasar Absorption Lines" (G. Meylan)
- "The Bottom of the Main Sequence – and Beyond" (Ed. C. Tinney)
- "Science with the VLT" (Eds. J.R. Walsh and I.J. Danziger)
- "The Light Element Abundances" (Ed. P. Crane)

ESO has negotiated an attractive price for these proceedings. They may be ordered directly from book stores or through Springer:

FAX: (49 30) 8201 301  
e-mail: orders@springer.de  
Post: Springer-Verlag, P.O. Box 311340, D-10543 Berlin

### To appear end of 1997/beginning of 1998:

- "Quasar Hosts – Low to High Redshift" (Eds. D. Clements and I. Perez-Fournon)
- "Origin, Evolution, and Astronomical Uses of Galaxy Scaling Relations" (Ed. L. Da Costa)

## PERSONNEL MOVEMENTS

### International Staff (1 July – 31 October)

#### ARRIVALS

##### EUROPE

ANGELONI, Elisabetta (I), Software Engineer (Archive Syst.)  
CARBOGNANI, Franco (I), Software Engineer  
SCHÖLLER, Markus (D), Paid Associate  
PULONE, Luigi (I), UpA DGDF  
BOAROTTO, Carlo (I), Software Engineer (Observ. Handling)  
DUPUY, Christophe (F), Opto-Mech. Technician  
MARIOTTI, Jean-Marie (F), Head of VLT Group  
PASQUALI, Anna (I), Astronomer ST-ECF  
FERRARI, Marc (F), Fellow  
SLIJKHUIS, Remco (NL), Student  
BRESOLIN, Fabio (I), Fellow  
GLINDEMANN, Andreas (D), Paid Associate VLT  
IBATA, Rodrigo (GB), Fellow  
WOUTD, Patrick (NL), Fellow  
CONTRADO, Gertrud (D), Student  
DELPLANCKE, Françoise (B), UpA (TMS) EC  
PITTICHOVÁ, Jana (SK), Student

##### CHILE

BÖHNHARDT, Hermann (D), Astronomer  
GONZALEZ, Jena-François (F), Fellow NTT Team  
LEISY, Pierre (F), Fellow  
JOGUET, Benoit (F), Student  
HAINAUT, Olivier (F), Fellow

#### DEPARTURES

##### EUROPE

BALLEMANS, Irma (NL), Adm. Asst. (Archives)  
CÔTÉ, Stéphanie (CDN), Fellow  
ZELLER, Kurt (CH), Head of Personnel

MENDEZ-BUSSARD (RCH), Fellow  
MÜLLER, Karen (ZA), Student  
ANDERSEN, Torben (DK), Senior Systems Analyst  
EISENHUTH, Dorothea (D), Secretary to the DG  
EMSELLEM, Eric (F), Fellow  
YAN, Lin (RC), Fellow

#### CHILE

MARTIN, Pierre (CDN), Fellow  
ATTERSJÖ, Hans (S), Electronics Engineer  
METANOMSKI, Agnès (F), Student  
PRIETO, Eric (F), Optical Engineer  
STORM, Jesper (DK), Astronomer  
PANTIN, Eric (F), Fellow

## Local Staff (1 July – 31 October)

#### ARRIVALS

CAMUZET, Blanca (RCH), Data Handling Operator  
AGUAYO, Ana Maria (RCH), Application Programmer  
IBSEN, Jorge (RCH), Application Programmer  
RIVEROS, Ivonne (RCH), Purchasing Assistant

#### DEPARTURES

LEVIN, Cristian (RCH), Informatics Engineer  
GONZALEZ, Germán (RCH), Administrative Assistant Paranal  
Logistics  
MELLA, Sergio (RCH), Electrician  
ROJAS, Waldo (RCH), Driver  
PEREZ, José (RCH), Photograph Unit Technician

## Uzbek Astronomy Looking Ahead Towards the Future

A co-operation agreement between ESO, Nice University, Moscow Sternberg Institute and Ulugh Beg Astronomical Institute of the Uzbek Academy of Science will be funded by INTAS (International association for the promotion of co-operation with scientists from the New Independent States of the former Soviet Union (NIS)). The accepted proposal aims at the 'Characterisation of Maidanak Observatory among the Major International Ground Based Astronomical Facilities of the Future' and covers the period 1998–1999 during which a number of site monitoring campaigns are planned and local instrumentation will be developed. Launched in 1983 in answer to the financial difficulties faced by many NIS scientists and in order to allow them to pursue their work, INTAS initiative is jointly financed by the EU and its Member States, Norway, Switzerland and Israel. Together with the 332 newly selected projects of the INTAS Call 1996 for 19 million ECU, more than 1,500 research projects covering natural and exact sciences as well as social sciences have already received INTAS support (source European Commission RTD Info Issue 16 and <http://www.cordis.lu/intas/pr170697.hUm>).

Contacts between ESO and Uzbek astronomy were initiated in March 1996 in the frame of the ESPAS (ESO Search for Potential Astronomical Sites) Working Group. A probe survey started in August 1996 confirmed the excellent seeing quality of Maidanak Observatory (38°41' North, 65°55' East, 2600 m altitude) and prompted the joint funding request. Thanks to the INTAS grant, five young Uzbek scientists will receive financial support during the next two years.

M. SARAZIN

## List of Scientific Preprints

#### (March–September 1997)

1213. L. Pasquini and P. Molaro: Lithium Observations in 47 Tuc. *A&A*.
1214. F. Comeron, J. Torra, F. Figueras: Understanding some Moving Groups in Terms of a Global Spiral Shock. *A&A*.
1215. C. Loup et al.: Obscured AGB Stars in the Magellanic Clouds. I. IRAS Candidates. *A&A*.
1216. A. Pizzella et al.: The Distribution of Ionized Gas in Early-Type Galaxies. III. M/L Determinations Based on Triaxial Models. *A&A*.
1217. M. Scodreggio, R. Giovanelli, M.P. Haynes: An Economical Technique for the Estimate of Galaxy Distances: The Photometric Fundamental Plane. *AJ*.
1218. T. Böhm, G.A. Hirth: Forbidden Lines in Herbig Ae/Be Stars. The [O I] (1F) 6300.31 Å and 6363.79 Å Lines. II. Longslit Observations of Selected Objects. *A&A*.
1219. J.-R. Roy, J.R. Walsh: The Abundance Gradient of NGC 1365: Evidence for a Recently Formed Bar in an Archetype Barred Spiral Galaxy. *M.N.R.A.S.*  
J.R. Walsh, J.-R. Roy: The O/H Distribution in the Transition Magellanic Galaxy NGC 1313. *M.N.R.A.S.*
1220. P. Ballester, M.R. Rosa: Modeling Echelle Spectrographs. *A&A*.
1221. C. Carignan, S. Côté, K.C. Freeman, P.J. Quinn: NGC 5084: A Massive Disk Galaxy Accreting Its Satellites? *AJ*.
1222. L. Pasquini, S. Randich, R. Pallavicini: Lithium in M67: Evidence for Spread in a Solar Age Cluster. *A&A*.
1223. W.P. Gieren, P. Fouqué, M. Gómez: Very Accurate Distances and Radii of Open Cluster Cepheids from a Near-Infrared Surface Brightness Technique. *ApJ*.
1224. D. Minniti, A.A. Zijlstra: Stellar Populations of the Dwarf Irregular Galaxy WLM.
1225. M. Turatto et al.: The Spectroscopic Diversity of Type II Supernovae.
1226. E. Cappellaro, M. Turatto: The Rate of Supernovae.
1227. J.T. van Loon et al.: Obscured Asymptotic Giant Branch Stars in the Magellanic Clouds. III. New IRAS Counterparts. *A&A*.
1228. Bo Reipurth et al.: Thackeray's Globules in IC 2944. *A&A*.
1229. H.-G. Reimann et al.: Mid Infrared Spectral Observations of UX Orionis. *A&A*.
1230. Bo Reipurth et al.: Hubble Space Telescope Images of the HH 111 Jet.
1231. S. Benetti et al.: Supernova 1994AJ: A Probe for Pre-Supernova Evolution and Mass Loss from the Progenitor. *M.N.R.A.S.*
1232. P. Martin, D. Friedl: Star Formation in Bar Environments. I. Morphology, Star Formation Rates and General Properties. *A&A*.
1233. P. François, J. Danziger, R. Buonanno, M.N. Perrin: Metallicity of the Young Halo Globular Cluster Ruprecht 106. *A&A*.
1234. L. Kaper et al.: Coordinated Ultraviolet and H $\alpha$  Spectroscopy of Bright O-Type Stars. *A&A*.
1235. N. Ageorges, A. Eckart, J.-L. Monin, F. Ménard: New Multiple Young Stellar Objects Discovered by Near-Infrared Speckle Imaging. *A&A*.
1236. F. Comeron: Dynamical Evolution of Wind-Driven HII Regions in Strong Density Gradients. *A&A*.
1237. P.-A. Duc, E. Brinks, J.E. Wink, I.F. Mirabel: Gas Segregation in the Interacting System Arp 105. *A&A*.
1238. Bo Reipurth, S. Heathcote: 50 Years of Herbig-Haro Research. From Discovery to HST. To appear in IAU Symposium No. 182 "Herbig-Haro Flows and the Birth of Low Mass Stars", Eds. Bo Reipurth and Claude Bertout, Kluwer, 1997, p.3.
1239. M. Mayor et al.: Radial Velocities of Southern Stars Obtained with the Photoelectric Scanner CORAVEL. VIII. Observations of 471 Giant Stars in  $\omega$  Centauri.
1240. D. Merritt, G. Meylan, M. Mayor: The Stellar Dynamics of  $\omega$  Centauri. *AJ*.
1241. L. Binette et al.: Photoionization of Very High Excitation Gas in the Circinus Galaxy and Other Active Galactic Nuclei. *A&A*.
1242. J.R. Walsh, G. Dudziak, D. Minniti, A.A. Zijlstra: Chemical Abundances of Planetary Nebulae in the Sagittarius Dwarf Elliptical Galaxy.
1243. E. Cappellaro et al.: SN Ia Light Curves and Radioactive Decay. *A&A*.
1244. M.-H. Ulrich, L. Maraschi, C.M. Urry: Variability of Active Galactic Nuclei. *Ann. Rev. of Astron. and Astroph.*, Vol. 35.
1245. K. Gesicki, A.A. Zijlstra, A. Acker, R. Szczerba: Velocity Fields of Planetary Nebulae. *A&A*.
1246. J.T. van Loon et al.: Obscured Asymptotic Giant Branch Stars in the Magellanic Clouds IV. Carbon Stars and OH/IR Stars. *A&A*.
1247. P. Molaro, P. Bonifacio, L. Pasquini: Lithium in Very Metal Poor Thick Disk Stars. *M.N.R.A.S.*
1248. M. Della Valle, R. Gilmozzi, A. Bianchini, H. Esenoglu: Study of Nova Shells II: FH Ser 1970 and QU Vul 1984, Nebular Expansion, Parallax and Luminosity. *AA*.
1249. A.A. Zijlstra, A. Wallander, L. Kaper, J.A. Rodriguez: Remote Observing at the ESO NTT & CAT Telescopes. *PASP*.

ESO, the European Southern Observatory, was created in 1962 to . . . establish and operate an astronomical observatory in the southern hemisphere, equipped with powerful instruments, with the aim of furthering and organising collaboration in astronomy . . . It is supported by eight countries: Belgium, Denmark, France, Germany, Italy, the Netherlands, Sweden and Switzerland. It operates the La Silla observatory in the Atacama desert, 600 km north of Santiago de Chile, at 2,400 m altitude, where fourteen optical telescopes with diameters up to 3.6 m and a 15-m submillimetre radio telescope (SEST) are now in operation. The 3.5-m New Technology Telescope (NTT) became operational in 1990, and a giant telescope (VLT = Very Large Telescope), consisting of four 8-m telescopes (equivalent aperture = 16 m) is under construction. It is being erected on Paranal, a 2,600 m high mountain in northern Chile, approximately 130 km south of Antofagasta. Eight hundred scientists make proposals each year for the use of the telescopes at La Silla. The ESO Headquarters are located in Garching, near Munich, Germany. It is the scientific, technical and administrative centre of ESO where technical development programmes are carried out to provide the La Silla observatory with the most advanced instruments. There are also extensive facilities which enable the scientists to analyse their data. In Europe ESO employs about 200 international Staff members, Fellows and Associates; at La Silla about 50 and, in addition, 150 local Staff members.

The ESO MESSENGER is published four times a year: normally in March, June, September and December. ESO also publishes Conference Proceedings, Preprints, Technical Notes and other material connected to its activities. Press Releases inform the media about particular events. For further information, contact the ESO Information Service at the following address:

EUROPEAN  
SOUTHERN OBSERVATORY  
Karl-Schwarzschild-Str. 2  
D-85748 Garching bei München  
Germany  
Tel. (089) 320 06-0  
Telex 5-28282-0 eo d  
Telefax (089) 3202362  
ips@eso.org (internet)  
ESO::IPS (decnet)

The ESO Messenger:  
Editor: Marie-Hélène Demoulin  
Technical editor: Kurt Kjær

Printed by  
Druckbetriebe Lettner KG  
Georgenstr. 84  
D-80799 München  
Germany

ISSN 0722-6691

## ESO Conference Proceedings Still Available

A number of ESO conference and workshop proceedings are still available. To permit you to complete the series or simply to inform you about any volume that you may have missed, we reproduce here a list of some of the more recent ones.

No.	Title	Price
45	ESO/EIPC Workshop "Structure, Dynamics and Chemical Evolution of Elliptical Galaxies", 1993	DM 90.—
46	Second ESO/CTIO Workshop on Mass Loss on the AGB and Beyond, 1993	DM 70.—
47	5th ESO/ST-ECF Data Analysis Workshop, 1993	DM 30.—
48	ICO-16 Satellite Conference on "Active and Adaptive Optics", 1994	DM 90.—
49	ESO/OHP Workshop on "Dwarf Galaxies", 1994	DM 90.—
50	ESO/OAT Workshop "Handling and Archiving Data from Ground-based Telescopes", 1994	DM 35.—
51	Third CTIO/ESO Workshop on "The Local Group: Comparative and Global Properties", 1995	DM 50.—
52	European SL-9/Jupiter Workshop, 1995	DM 80.—
53	ESO/ST-ECF Workshop on "Calibrating and understanding HST and ESO instruments", 1995	DM 60.—
54	OSA/ESO Topical Meeting on "Adaptive Optics", 1996	DM 80.—

## Contents

### TELESCOPES AND INSTRUMENTATION

A. Kaufer, B. Wolf, J. Andersen, L. Pasquini: FEROS, the Fiber-fed Extended Range Optical Spectrograph for the ESO 1.52-m Telescope .....	1
M. Sarazin: ESO Internal Workshop on Forecasting Astronomical Observing Conditions — 29–30 May 1997. Predicting Observing Conditions at ESO Observatories — Reality and Perspectives .....	5
Sunset on Paranal .....	10
G. Mathys: News from the NTT .....	11
C. Madsen: ESO at the Leipzig Fair .....	13

### REPORTS FROM OBSERVERS

P.-A. Duc, I.F. Mirabel: Tidal Dwarf Galaxies .....	14
M.C. Festou, M. Gunnarsson, A. Winnberg, H. Rickman, G. Tancredi: The Activity of Comet 29P/Schwassmann-Wachmann 1 Monitored Through the CO J(2–1) Emission Line at 230 GHz .....	18
V. de Lapparent, G. Galaz, S. Arnouts, S. Bardelli, M. Ramella: The ESO-Sculptor Faint Galaxy Survey: Large-Scale Structure and Galaxy Populations at $0.1 \lesssim z \lesssim 0.5$ .....	21
L. Kaper, F. Comerón, J. Th. van Loon, A.A. Zijlstra: Massive Stars Running Through Space .....	28
F. Comerón, P. Claes, G. Rieke: Oph 2320.8–1721, a Young Brown Dwarf in the $\rho$ Ophiuchi Cluster: Views from the Ground and from Space .....	31
J.-L. Monin, H. Geoffroy: PMS Binaries in Southern Molecular Clouds Observed with ADONIS + COMIC .....	33
W. Brandner, J.M. Alcalá, S. Frink, M. Kunkel: An ESO 3.6-m/Adaptive Optics Search for Young Brown Dwarfs and Giant Planets .....	37
C. Madsen: The ESO Exhibition at the IAU General Assembly in Kyoto, Japan .....	40

### OTHER ASTRONOMICAL NEWS

L.B. Lucy: Enhanced Resolution with Two-Channel Deconvolution Codes .....	41
---	----

### ANNOUNCEMENTS

ESO Astrophysics Symposia Proceedings .....	42
Personnel Movements .....	42
List of Scientific Preprints .....	42
M. Sarazin: Uzbek Astronomy Looking Ahead Towards the Future .....	43
ESO Publications Still Available .....	43